Ore Geology Reviews 71 (2015) 373–404

Contents lists available at ScienceDirect

Ore Geology Reviews

journal homepage: www.elsevier.com/locate/oregeorev

Magmatic sequences in the Halasu Cu Belt, NW China: Trigger for the Paleozoic porphyry Cu mineralization in the Chinese Altay–East Junggar

Chao Wu [a,c], Huayong Chen [a,*], Pete Hollings [b], Deru Xu [a], Pei Liang [a,c], Jinsheng Han [a], Bing Xiao [a,c], Keda Cai [d], Zhenjiang Liu [e], Yukun Qi [e]

[a] Key Laboratory of Mineralogy and Metallogeny, Guangzhou Institute of Geochemistry, Chinese Academy of Sciences, Guangzhou 510640, China
[b] Department of Geology, Lakehead University, 955 Oliver Road, Thunder Bay, Ontario P7B 5E1, Canada
[c] Graduate University of Chinese Academy of Sciences, Beijing 100049, China
[d] Xinjiang Research Center for Mineral Resources, Xinjiang Institute of Ecology and Geography, Chinese Academy of Sciences, Urumqi, Xinjiang 830011, China
[e] No. 4 Geological Party of the Xinjiang Bureau of Geology and Mineral Exploration and Development, Altay, Xinjiang 836500, China

ARTICLE INFO

Article history:
Received 12 April 2015
Received in revised form 23 June 2015
Accepted 24 June 2015
Available online 26 June 2015

Keywords:
U–Pb geochronology
Zircon trace elements
Sr–Nd–Pb–Hf isotopes
Oxidized magma
Flat subduction
Halasu porphyry copper belt

ABSTRACT

The Halasu porphyry copper belt situated in the East Junggar is one of the major porphyry copper belts in Xinjiang Uygur Autonomous Region, northwest China. Copper and molybdenum mineralization occurs as disseminated sulfides or veinlets mainly in granodiorite porphyry and diorite porphyry, with the intense development of zoned alteration from potassic, through sericitic to an outer zone of propylitic alteration.

New LA–ICP-MS zircon U–Pb dating reveals that magmatism in the belt can be divided into three periods during the Middle Devonian and Early Carboniferous, namely the pre-mineralization stage of 390 Ma, syn-mineralization stage of 382–372 Ma, and post-mineralization stage of 350–320 Ma. The syn-mineralization intrusions are calc-alkaline, whereas pre- and post-mineralization intrusions are shoshonitic and high-K calc-alkaline. The syn-mineralization intrusions are enriched in highly incompatible trace elements but depleted in Nb, Ta, Hf and Ti relative to the pre- and post-mineralization intrusions.

Zircon trace elements analyses demonstrate a negative correlation between Ti-in-zircon temperatures and oxygen fugacity. Ore-bearing syn-mineralization granitoids are characterized by higher water content, oxygen fugacity and low temperatures with higher mineralization potential than pre- and post-mineralization ones. These characteristics, together with the geochemical signature of the intrusions, suggest that the ore-bearing porphyries are derived from relative high fH_2O magma reservoir. The remarkably homogeneous Hf isotopic compositions (εHf(t) = 8 to 13) from syn-mineralization intrusions span over 10 m.y., suggesting the existence of a long-lived reservoir beneath Halasu belt during the Middle Devonian. All the intrusions have low initial $^{87}Sr/^{86}Sr$ values (0.703935 to 0.707172), high εNd(t) values (4.7 to 5.5) and young crustal model ages (650 to 750 Ma). Combined with the mantle-derived Pb isotope characteristics, the Sr–Nd–Hf data suggest that the parental magma was probably derived from flat subduction triggered partial melting of juvenile crust generated during subduction–accretionary process with no significant input of old crust, whereas pre-mineralization and post-mineralization intrusions are supposed to emplaced in immature island arc setting and post-orogenic setting, respectively.

1. Introduction

The Central Asian Orogenic Belt (CAOB), located between the Siberian and Russian cratons to the north, and the Tarim and North China cratons to the south (Fig. 1a), is among one of the world's largest accretionary orogens (Carroll et al., 1990; Sengör et al., 1993; Mossakovsky et al., 1994; Jahn et al., 2000; Khain et al., 2003; Xiao et al., 2009a). The CAOB contains a variety of mineral systems including some giant porphyry Cu deposits and as such is one of the largest porphyry deposits belts in the world (Yakubchuk, 2002, 2004; Yakubchuk et. al., 2005; Mao et al., 2014; Seltmann et al., 2014). It is acknowledged that the Altay–East Junggar orogenic collage

* Corresponding author.
E-mail address: huayongchen@gig.ac.cn (H. Chen).

http://dx.doi.org/10.1016/j.oregeorev.2015.06.017

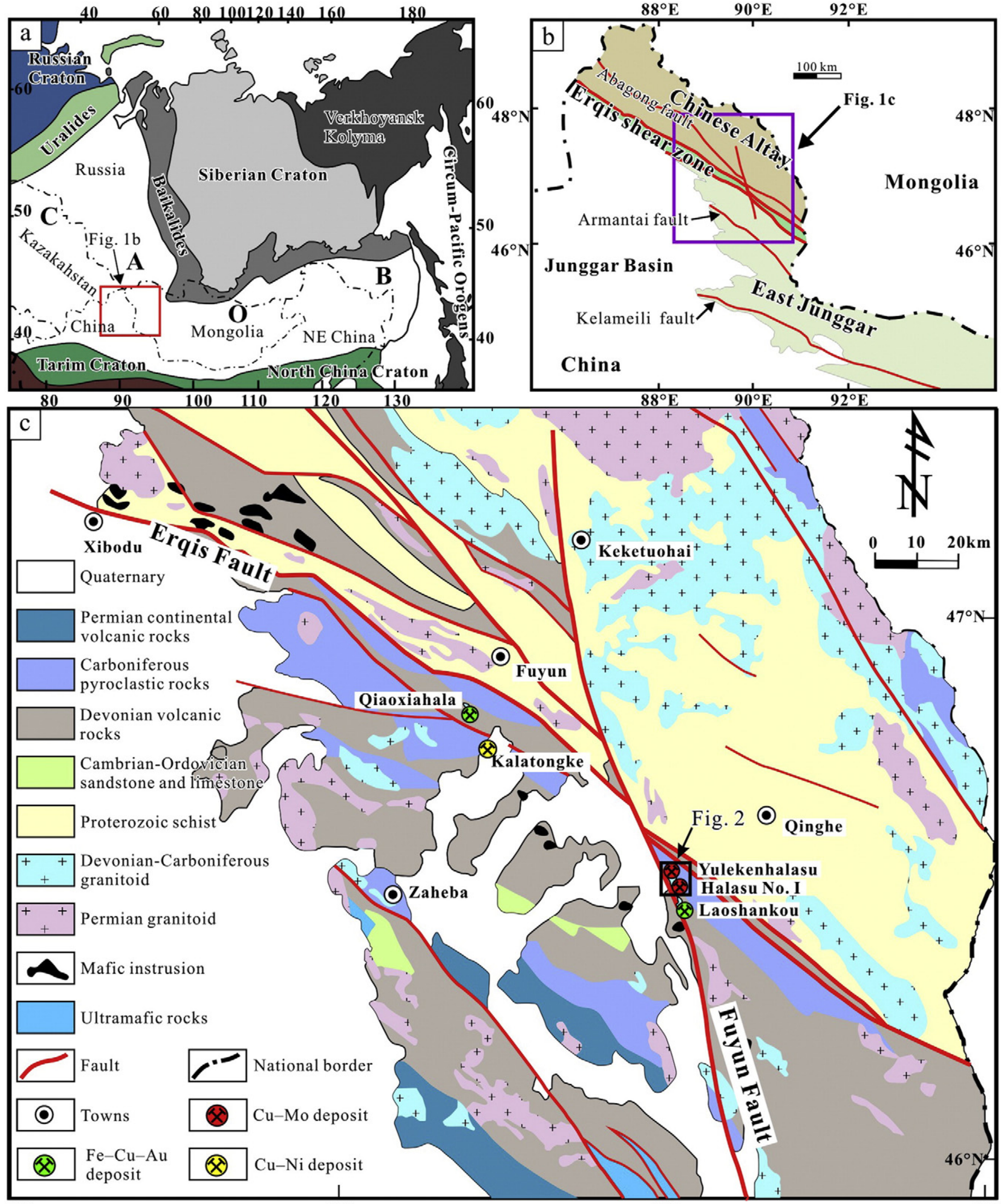

Fig. 1. (a) Relationship of study area with the central Asian orogenic belt (modified from Jahn et al., 2000); (b) relationship of study area with the Chinese Altay–East Junggar orogenic collage (modified from Wan et al., 2014); (c) regional geologic map of the southeastern Altay orogenic belt and northeastern Junggar block, northern Xinjiang (modified from Zhang et al., 2009a).

(CAEJ) in northeastern Xinjiang (Fig. 1b), linking the Kazakhstan and Tuva–Mongol oroclines, is considered as a key area for understanding the complicated orogenic processes of the CAOB (Coleman, 1989; Sengör et al., 1993; Xiao et al., 2004).

Despite ongoing exploration efforts, porphyry deposits in the CAEJ are smaller than those of Kazakhstan to the west and Mongolia to the east in terms of both grade and tonnage (Heinhorst et al., 2000; Perelló et al., 2001; Yakubchuk et al., 2005;

Dong and Li, 2006; Zhao et al., 2009a; Wan et al., 2014). In the CAEJ, the Halasu porphyry copper belt (or Kalaxiange'er porphyry copper belt), including the Yulekenhalasu, Halasu I, II and III orebodies from north to south, was the first porphyry copper district recognized since exploration commenced in the 1960s (Liu et al., 1991; Yan et al., 2006; Yang et al., 2012b). The mineralization in Halasu belt is closely associated with the Late Devonian porphyries (Xiang et al., 2009; Zhao et al., 2009b; Yang et al., 2012c); however, many coeval intrusions in Halasu are geochemically similar to the ore-bearing ones but lack copper mineralization. Moreover, the geochemical and petrological relationships between syn-mineralization ore-bearing intrusions, barren intrusions and porphyry Cu mineralization remain unclear.

Previous researches in the Halasu porphyry copper belt were focused on individual deposits, especially the nature of the ore-forming fluids (Yang et al., 2010b, 2012a; Geng et al., 2013), geochronology and geochemistry of the ore-bearing intrusions (Xue et al., 2010; Yang et al., 2012c) with pre- and post-mineralization magmatism receiving little attention. These earlier studies have proposed that porphyry mineralization during the Late Devonian was probably formed in an island arc setting and overprinted by the Late Carboniferous intensive deformation in an intra-plate setting. However, the evolution of the pre-, syn- and post-mineralization magmatism in various tectonic settings and the genetic relationships with porphyry mineralization are still poorly understood.

In order to solve the above problems, this study focused on the comparison of ore-bearing and barren intrusions in the Halasu belt to place them in the Devonian and Carboniferous tectonic framework of the CAEJ. Additionally, based on the zircon trace element analyses, magma oxygen fugacity and temperatures were calculated and combined to trace the evolution of magma. These parameters have rarely been applied in the East Junggar, so this paper will not only provide constrains on the accretionary process of the CAEJ and the CAOB, but also help to estimate the potential for exploration for porphyry deposits in this region.

2. Regional geology

The CAEJ orogenic collage, which is bounded by Mongolia to the east and Kazakhstan to the west, lies in northeastern Xinjiang and can be subdivided into three juxtaposed tectonic units, namely the Chinese Altay, the Erqis shear zone and the East Junggar from north to south, respectively (Fig. 1b). The Halasu porphyry copper belt is located in the northern margin of the East Junggar, which lies several kilometers away from the southern margin of the Erqis shear zone (Fig. 1c). Three metallogenic belts have been distinguished in the CAEJ (Wan et al., 2011), a volcanogenic massive sulfide (VMS) Cu–Pb–Zn belt in the Chinese Altay, a shear zone-related Au (or orogenic gold) belt in the Erqis shear zone and a porphyry Cu–Au–Mo belt in the East Junggar. The porphyry deposits developed in three pulses in the East Junggar, at ca. 405 Ma, ca. 375 Ma and ca. 330 Ma. Apart from porphyry systems, the East Junggar also contains skarn (or IOCG) deposits, orogenic gold deposits and magmatic Cu–Ni sulfide deposits (Han et al., 2004; Wan and Zhang, 2006; Li et al., 2014; Fig. 1c).

The Chinese Altay in the northern CAEJ comprises the Middle Ordovician to Late Carboniferous rocks ranging from neritic clastic sedimentary rocks, limestone, turbiditic sand-shale to island-arc pyroclastic rocks, whereas the Erqis shear zone predominantly contains high-grade gneisses and schists, Late Paleozoic ophiolitic fragments and mafic-intermediate lavas (Fig. 1c). Intrusions outcropping in the Chinese Altay and Erqis shear zone are mainly Late Paleozoic granites, including the Ordovician to Carboniferous and the Permian granites. The East Junggar domain is characterized by the Devonian mafic-intermediate volcanic rocks, marine sedimentary rocks, the Early to Middle Carboniferous intermediate volcanic and sedimentary rocks and minor Silurian sedimentary rocks, as well as the Early Permian continental volcanic facies. Moreover, according to previous regional studies, the lack of Late Carboniferous rocks in the East Junggar region, together with the Early Permian continental volcanic facies rather than marine facies, may indicate a tectonic transition in this area during the Late Carboniferous (Xiao et al., 1992; Dong et al., 2009). In addition to the Devonian to Early Carboniferous calc-alkaline granites and adakites, the East Junggar also hosts minor Late Carboniferous and Permian A-type granite dykes. The calc-alkaline granites are considered to form in an intra-oceanic island arc in the Junggar Ocean with the A-type granites possibly representing the post-orogenic environment (Xiao et al., 2009b; Wang et al., 2010; Fig. 1c).

In CAEJ, the Erqis shear zone separating the Chinese Altai to the north from the East Junggar to the south and the Abagong Fault dividing the Chinese Altai into northern and southern Altai Mountains, are the domain boundaries. Major fault systems in the East Junggar are mainly NW-trending thrusts, including the Armantai and Kelameili faults, and NNW-trending strike–slip faults, such as the Fuyun Fault (Windley et al., 2002; Wan et al., 2011; Fig. 1b). The Erqis Fault is thought to be the boundary separating Kazakhstan orocline from Tuva–Mongol orocline, thus playing a key role in the evolution of the CAOB. According to different accretionary orogenic models, various interpretations have been proposed to explain the nature of Erqis Fault. It has been interpreted as a dextral strike–slip fault that has undergone more than 1000 km of displacement (Sengör et al., 1993); a suture zone between the Chinese Altay arc and Junggar arc (Coleman, 1989; Badarch et al., 2002) or a crustal-scale thrust that remained active until the Permian (Laurent-Charvet et al., 2002). The 180-km-long Fuyun Fault, an active oblique slip fault which has caused five high-magnitude paleo-earthquakes in the last 10000 years, truncates the Erqis Fault with 7 to 8 km dextral displacement (Ge et al., 1986; Windley et al., 2002; Fig. 1c).

3. Local geology

The Halasu porphyry copper belt is situated in the northern margin of the East Junggar domain and consists of five ore deposits, from north to south these are the Yulekenhalasu, Dunke'erman, Halasu I, II and III ore deposits (Fig. 2). The Halasu I ore deposit contains 0.17 Mt of copper with an average grade of 0.34% and the Yulekenhalasu contains more than 0.04 Mt of copper with an average grade of 1.04% (Liu et al., 2010; Yang et al., 2012a). Three principal fault systems are recognized in the belt (Figs. 1c, 2), of which the N- and NNW-trending fault systems have similar strike directions to the ore bodies and are closely associated with the regional Fuyun Fault that dips sharply to the southwest. The mineralized porphyries are extensively deformed by the three fault systems, especially the WNW- and NNW-trending fault systems, though intrusions are mainly controlled by the N- and NNW-trending fault systems. The outcropping marine volcanic or volcaniclastic rocks in the Halasu porphyry copper belt are dominated by the Middle Devonian Beitashan Formation and the Lower Carboniferous Jiangbasitao Formation, both of which are considered to have been deposited in a volcanic arc setting (Zhang et al., 2009b). The Beitashan Formation, predominantly comprised of mafic to intermediate lavas and corresponding tuffs, breccias and sandstones, crops out in the whole belt, whereas the overlying Jiangbasitao Formation crops out exclusively in the Yulekenhalasu district, and is separated by an unconformity from the underlying Beitashan Formation and consists chiefly of carbonaceous slate, conglomerate, tuffaceous sandstone and intermediate tuff intercalated with minor andesite.

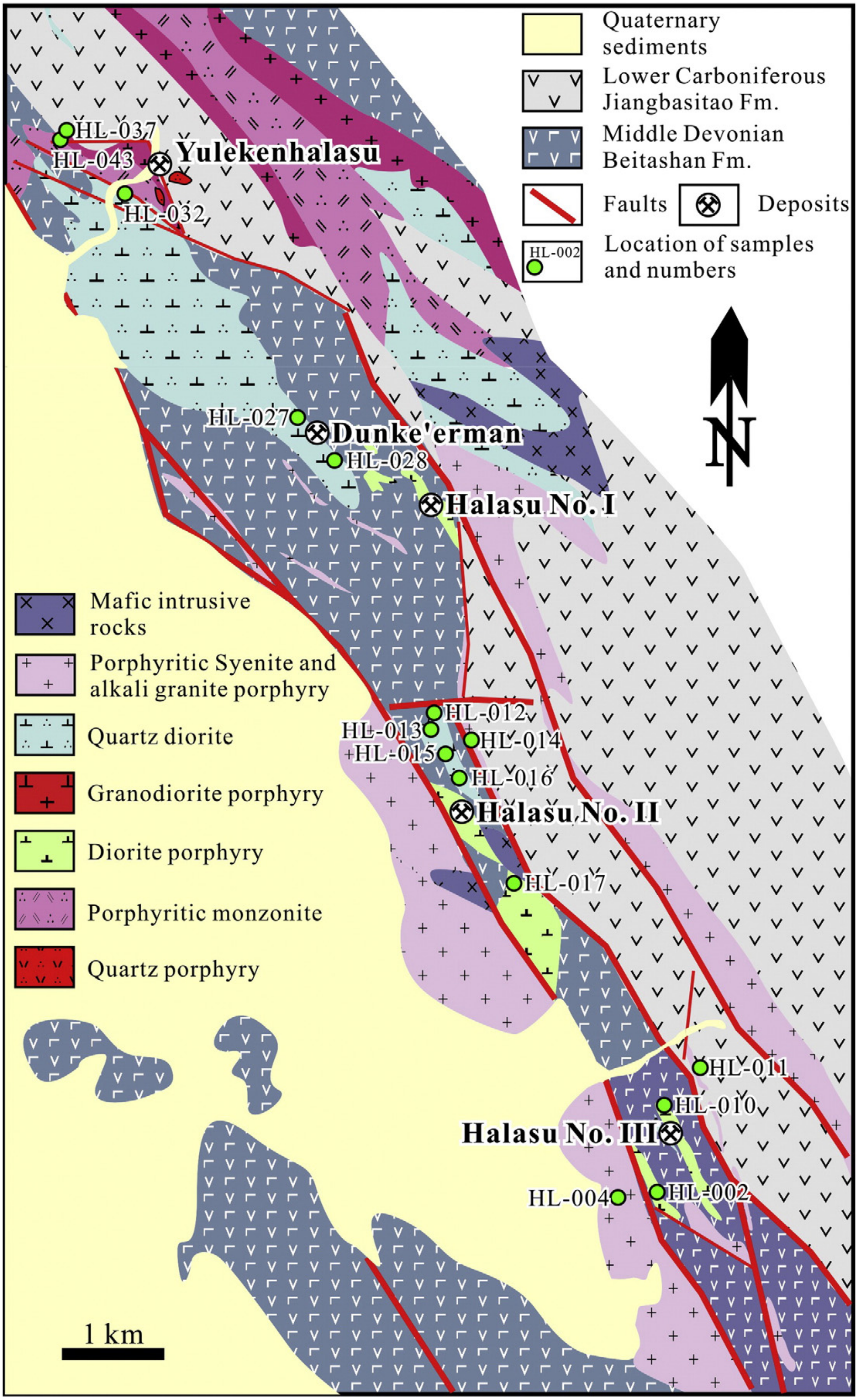

Fig. 2. Simplified geological map of the Halasu belt.
Modified from the No. 4 Geological Party of the Xinjiang Bureau of Geology and Mineral Exploration and Development, 2009.

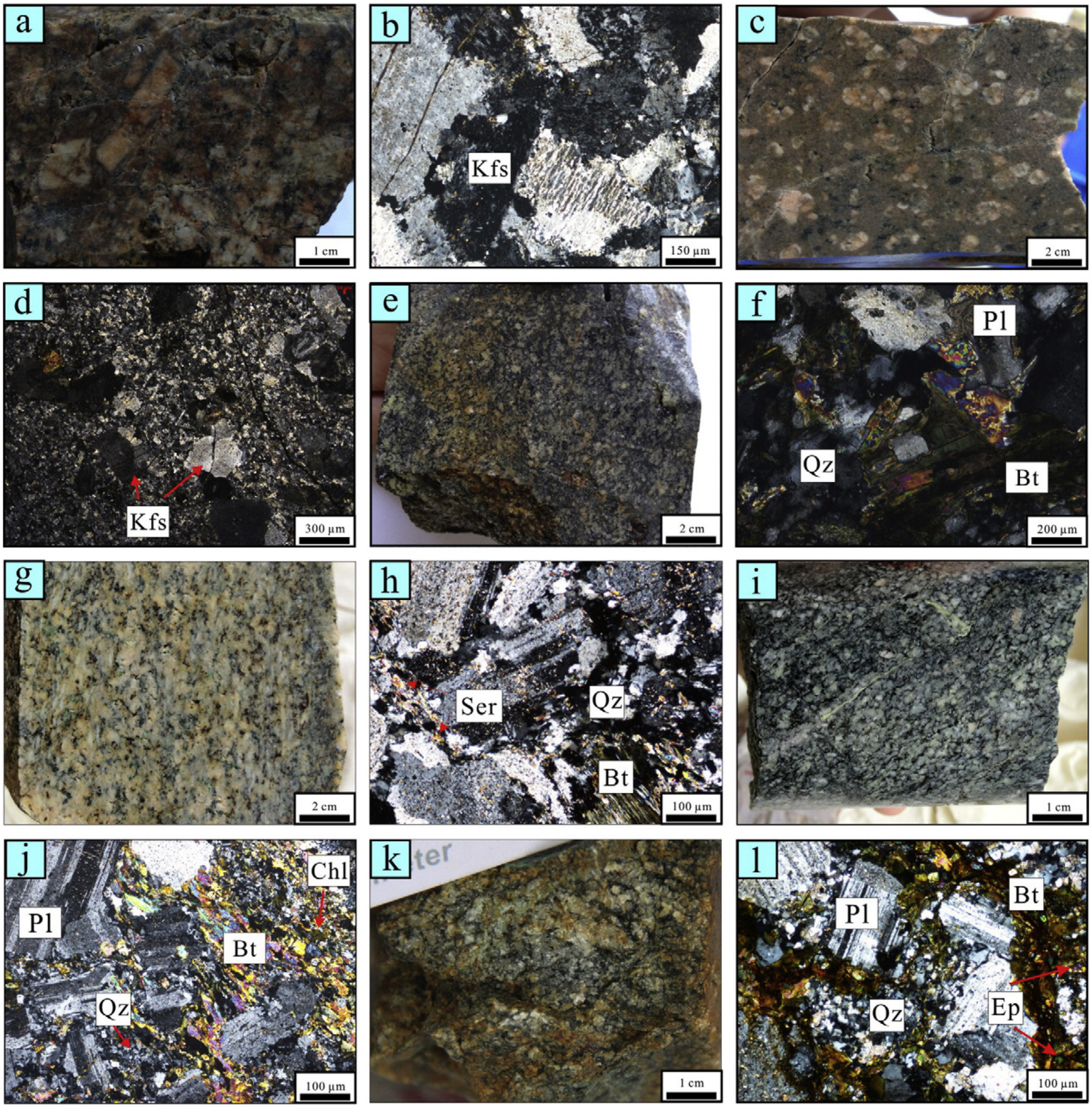

Fig. 3. Representative photographs and photomicrographs of the granitoids in the Halasu porphyry copper belt. (a–b) Porphyritic syenite. (c–d) Alkali granite porphyry. (e–f) Quartz diorite. (g–h) Granodiorite. (i–j) Granodiorite porphyry. (k–l) Diorite porphyry. Abbreviations in figures are based on Whitney and Evans (2010).

3.1. Intrusive rocks

Intrusive rocks in the Halasu porphyry copper belt generally range from the Middle Devonian to Late Carboniferous in age with a peak in the Late Devonian that corresponds with the main mineralization stage (Xiang et al., 2009; Xue et al., 2010; Yang et al., 2012c). Based on the spatial relationship observed in surface mapping, drill core logging and the temporal association between intrusions and mineralization, the intrusive rocks in Halasu belt can be subdivided into two groups: the alkali-rich group and the calc-alkali group.

Two alkali-rich intrusive rock units are found within the belt, a porphyritic syenite (Fig. 3a, b), also referred to as porphyritic monzonite by Yang et al. (2014), and an alkali granite porphyry (Fig. 3c, d). The former crops out as irregular NNW trending stocks in the Yulekenhalasu and Halasu III districts whereas the latter crops out as dykes (Fig. 2). The porphyritic syenite contains coarse-grained K-feldspar as the main phenocrysts with a matrix of fine-grained quartz. The alkali granite porphyry, which intruded into the Middle Devonian Beitashan Formation, comprises phenocrysts of coarse-grained K-feldspar with minor biotite and a groundmass of fine-grained K-feldspar, quartz and biotite.

The quartz diorite (Fig. 3e, f), granodiorite (Fig. 3g, h), granodiorite porphyry (Fig. 3i, j) and diorite porphyry (Fig. 3k, l) are the dominant syn-mineralization calc-alkali intrusions in the Halasu belt (Fig. 2). The quartz diorite, which crops out as a large stock in the north and as NW-trending dikes in the south of the belt, locally intruded the Beitashan Formation and is composed of plagioclase, quartz and biotite, with minor alkali feldspar, titanite, apatite, magnetite and zircon. Granodiorite, which intruded the Beitashan

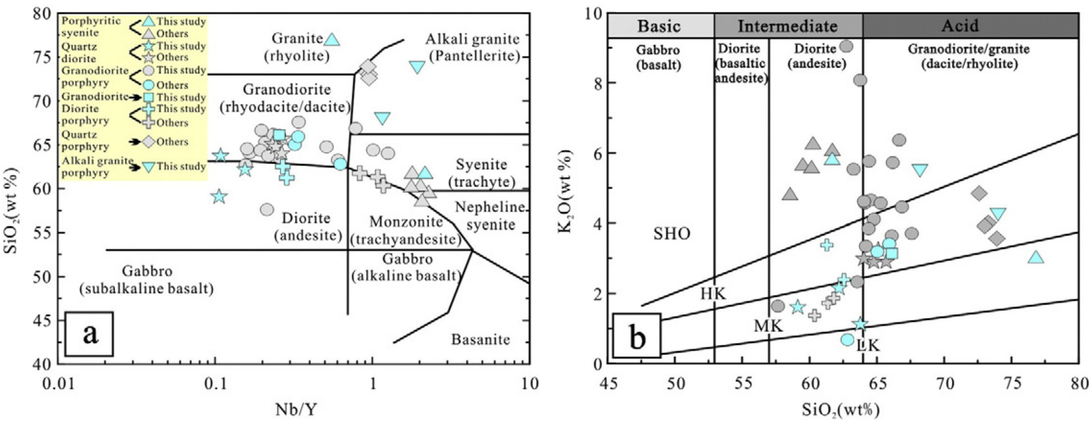

Fig. 4. (a) Nb/Y vs. SiO_2 diagram, modified from Winchester and Floyd (1977). (b) SiO_2 vs. K_2O discrimination diagrams constructed using whole-rock geochemistry from the intrusions in Halasu porphyry copper belt, modified from Peccerillo and Taylor (1976). LK, MK, HK, and SHO are low-K tholeiite series, medium-K calc-alkaline series, high-K calc-alkaline series and shoshonitic series, respectively. Data are from Feng and Zhang (2009), Wan and Zhang (2006), Yang et al. (2014), and Yang et al. (2005), supplemented with data from this study. Note that the significant dispersion of granodiorite porphyry observed in panel b due to potassic alteration is removed in the immobile element Nb/Y panel a and the high SiO_2 content of one porphyritic syenite sample is resulted from silicification.

Formation and crops out as irregular small stocks in the Halasu II ore district, is composed of plagioclase, quartz and perthite, with minor apatite.

Granodiorite porphyry and diorite porphyry, which comprise the main ore-bearing intrusions, intruded into the Middle Devonian Beitashan Formation and share similar petrographic characteristics, whereas the granodiorite porphyry has a weak to moderately porphyritic texture. They comprise plagioclase, quartz, K-feldspar, minor biotite and amphibole. The granodiorite porphyry in the Halasu I ore district generally strikes 325°, dips southwest and extends for about 1 km with the width ranging from 50 to 150 m.

Diorite porphyry occurring as irregular stocks and dykes which are 50 to 500 m wide and 2.7 km long also hosts mineralization. They generally strike 110–120°, dip 30–60° northeast and are separated from the Lower Carboniferous Jiangbasitao Formation by faults in the Yulekenhalasu ore district. The diorite porphyry comprises plagioclase phenocrysts plus minor biotite, with a groundmass of fine-grained plagioclase and microgranular quartz.

Quartz porphyry, as mentioned by Yang et al. (2014) but not identified in this study, is exposed only in the Yulekenhalasu ore district as dykes emplaced in the Lower Carboniferous Jiangbasitao Formation, which makes it obviously different from the earlier intrusions. It has a porphyritic texture with quartz and minor plagioclase as phenocrysts, and a groundmass of quartz, plagioclase and biotite.

3.2. Mineralization and alteration

The mineralization in the Halasu porphyry Cu belt is mainly associated with the Late Devonian intrusive rocks and is characterized by disseminated, quartz vein or veinlet types in porphyries and adjacent strata. Among the syn-mineralization calc-alkali intrusions, granodiorite porphyry and diorite porphyry are the main ore-bearing intrusions in Halasu belt, whereas the quartz diorite is generally barren. Moreover, the granodiorite can also be barren or host insignificant primary mineralization and occasionally underwent sericite alteration and supergene process.

Based on the distribution of mineralization, two mineralized zones have been recognized in the Yulekenhalasu ore district, of which the dominant zone occurring in diorite porphyry discontinuously extends for approximately 800 m in length with a width ranging from 20 to 120 m. Dunke'erman ore district lies 2.5 km to the southeast of Yulekenhalasu ore district and covers a mineralized area approximately 2000 m × 400 m. In contrast, orebodies in the Halasu I, which occur as lenses, irregular vein shape in both porphyry and the surrounding Middle Devonian Beitashan Formation, generally strike 310° and extend for about 1000 m in length with the width of 20 m to 150 m. There is similar mineralization present in the Halasu II and III ore deposits, of which the former defines an area of mineralized rocks approximately 2100 m × 250 m but the latter covers an area about 800 m × 500 m (Fig. 2).

The ore minerals in the Halasu porphyry copper belt are primarily chalcopyrite, pyrite and molybdenite with less bornite, magnetite, galena, sphalerite and pyrrhotite. Gangue minerals are mainly quartz, feldspar, biotite, gypsum, sericite, chlorite, epidote and calcite. Ores occur in various textures including disseminated, veinlets, stockworks, metasomatic relict, and cataclastic textures. Oxidized ore, mainly distributed in the supergene zone of Halasu II and III ore deposits, contains abundant supergene minerals including hematite, chrysocolla, bornite and limonite with minor azurite.

Mineralized porphyries in the Halasu I and Yulekenhalasu districts have undergone intense hydrothermal alteration including potassic, sericitic, propylitic and silicic alteration, of which the potassic and sericitic zones are intimately associated with Cu mineralization (Yang et al., 2005; Xiang et al., 2009, 2012; Geng et al., 2013). The potassic alteration is characterized by quartz, K-feldspar, and biotite overprinting original minerals, whereas the sericitic alteration is characterized by fined-grained quartz and sericite. The propylitic alteration comprises mainly epidote, chlorite and calcite generally in the outer zone of the alteration. In addition, primary minerals or previous assemblages have generally been overprinted, for example, original plagioclase may be destroyed by sericite and secondary biotite in the potassic zone may be overprinted by chlorite.

4. Sampling and analytical methods

Since most of the intrusive rocks in the Halasu porphyry copper belt have undergone various degrees of alteration, the least altered rocks were sampled for the zircon U–Pb dating, trace elements and Hf isotope analyses, whole-rock geochemical and Sr–Nd–Pb isotopic analyses. Samples, including the alkali-rich group (porphyritic

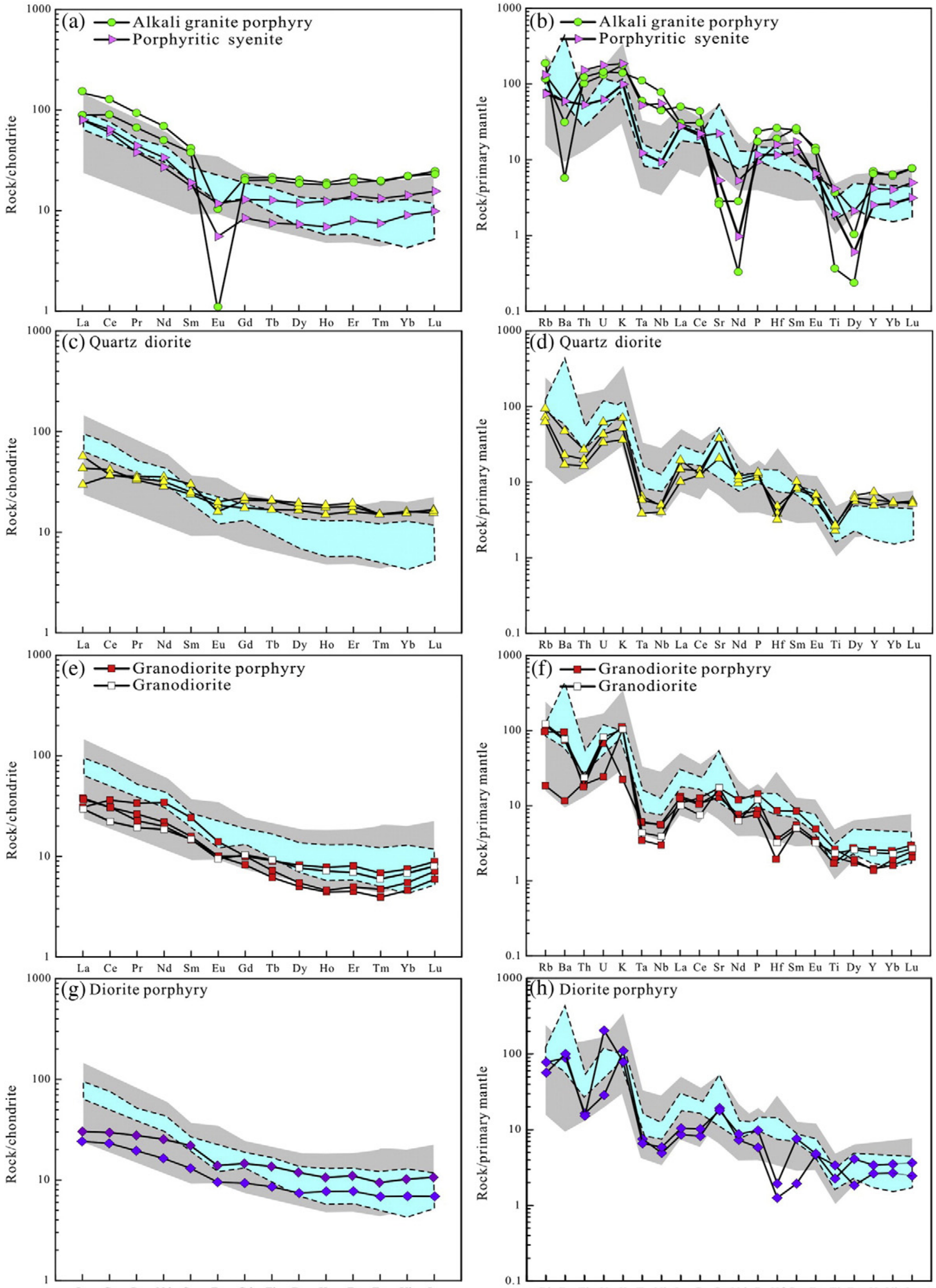

Fig. 5. Chondrite-normalized REE patterns and primitive mantle-normalized spider diagrams for the intrusions in Halasu belt. The normalizing values of chondrite and primitive mantle are from Sun and McDonough (1989). The gray area represents the range of compositions of ore-bearing porphyry in Halasu belt (Feng and Zhang, 2009; Wan and Zhang, 2006; Yang et al., 2005) and the blue area represents the range of compositions of ore-bearing porphyry in Oyu Tolgoi district (Wainwright et al., 2011).

syenite and alkali granite porphyry) and the syn-mineralization calc-alkali group (quartz diorite, granodiorite, granodiorite porphyry and diorite porphyry), were mainly collected from surface exposures of the stocks and dikes in the belt, while some of the granodiorite porphyry and diorite porphyry samples were also sampled from drill cores in the Yulekenhalasu ore district (Fig. 3i, j). However, because

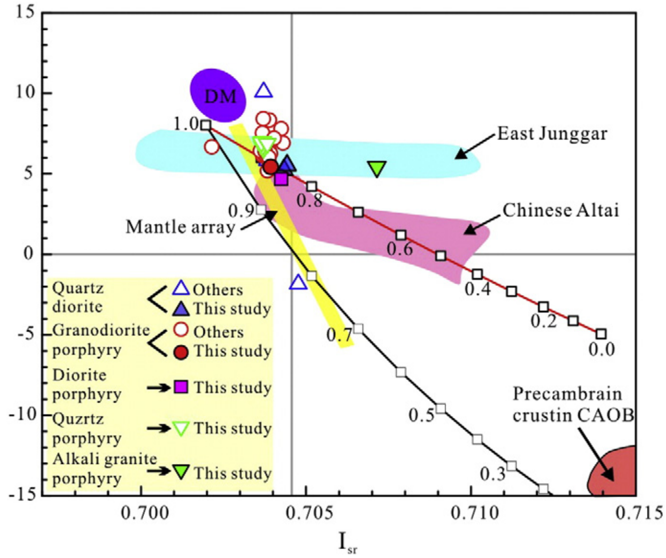

Fig. 6. $(^{87}Sr/^{86}Sr)_i$ vs. εNd(t) diagram of the intrusions from Halasu belt. The data of East Junggar are from Chen and Jahn (2004), Han et al. (1997), and Tang et al. (2007), data of Chinese Altai are from Wang et al. (2009). The mixing model of two end-members: the data for depleted mantle-derived basaltic component ($^{87}Sr/^{86}Sr$ = 0.702, Sr = 200 ppm, ε_{Nd} = +8, Nd = 15 ppm) are from Jahn et al. (2000) and Zimmer et al. (1995), the crustal components are characterized by $^{87}Sr/^{86}Sr$ = 0.703 and Sr = 200 ppm but different Nd components (ε_{Nd} = −17, Nd = 36 ppm and ε_{Nd} = −5, Nd = 25 ppm) according to Hu et al. (2000) and Kovalenko et al. (2004).

of the limited distribution of quartz porphyry in Halasu belt, we were unable to sample this unit. Specific analytical methods are summarized below.

4.1. Whole-rock major and trace element analyses

The major and trace elements of the bulk rock samples were determined at the Mineral Division of ALS Chemex (Guangzhou) Co. Ltd. Whole rock samples were first powdered to less than 200 mesh, then fluxed with $Li_2B_4O_7$ and $LiBO_2$ to make homogeneous glass disks at 1050–1100 °C. The major elements were analyzed by X-ray fluorescence spectrometry on fused glass beads using a PANalytical Axios. The analytical precision for major elements was better than 1%.

For trace element analyses, about 50 mg of powder for each sample was added to lithium metaborate flux, mixed well and fused in a furnace at 1000 °C. The resulting melt was then cooled and dissolved in 100 ml of 4% HNO_3 solution. The REE and trace element concentrations of the sample solutions were determined by inductively coupled plasma mass spectrometry (PerkinElmer Elan 9000) with the analytical precision better than 5% for most trace elements. The results of whole-rock major and trace elements analyses are listed in Appendix Table A1.

4.2. Whole-rock Sr–Nd–Pb isotopic analyses

Whole-rock Sr–Nd–Pb isotopic analyses were carried out at the State Key Laboratory of Isotope Geochemistry, Guangzhou institute of Geochemistry, Chinese Academy of Sciences. The isotope measurements were performed on a Neptune Plus multi-collector mass spectrometer equipped with nine Faraday cup collectors and eight ion counters. Details of Sr–Nd–Pb isotopic analytical methods are similar to Chernyshev et al. (2007) and Yang et al. (2009). Normalizing factors used to correct the mass fractionation of Sr and Nd during the measurements are $^{86}Sr/^{88}Sr = 0.1194$ and $^{146}Nd/^{144}Nd = 0.7219$. Analyses of standards NIST SRM 987, the Shin Etsu JNdi-1 over the measurement period provided $^{87}Sr/^{86}Sr = 0.710290 \pm 0.000014$ (2σ) and $^{143}Nd/^{144}Nd = 0.512094 \pm 0.000008$ (2σ), respectively. Samples for Pb analyses were doped with Tl and mass discrimination was corrected relative to a certified $^{205}Tl/^{203}Tl$ ratio. Analyses of standard NIST SRM 981, over the measurement period provided average values of $^{206}Pb/^{204}Pb = 16.931 \pm 0.0006$ (2σ), $^{207}Pb/^{204}Pb = 15.485 \pm 0.0006$ (2σ), and $^{208}Pb/^{204}Pb = 36.676 \pm 0.0018$ (2σ). The results of whole-rock Sr–Nd–Pb isotopic analyses are listed in Appendix Table A2.

4.3. Zircon U–Pb dating and trace elements

Zircon sample pretreatment was undertaken at the Chengxin Geology Service Co. Ltd, Langfang, Hebei Province, China, and further screening and imaging were performed at the State Key Laboratory of Isotope Geochemistry, Guangzhou Institute of Geochemistry, Chinese Academy of Sciences. Zircon grains were separated from ~2 kg samples, using standard methods with both magnetic and density separation procedures, followed by hand picking under a binocular

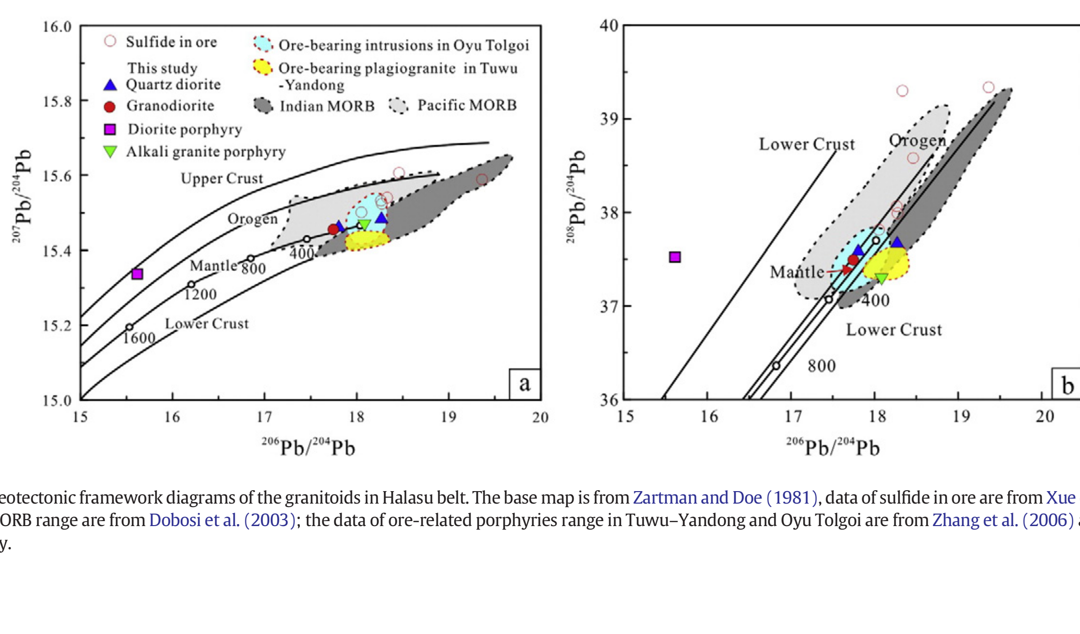

Fig. 7. Pb isotopic geotectonic framework diagrams of the granitoids in Halasu belt. The base map is from Zartman and Doe (1981), data of sulfide in ore are from Xue et al. (2010); the data representing the MORB range are from Dobosi et al. (2003); the data of ore-related porphyries range in Tuwu–Yandong and Oyu Tolgoi are from Zhang et al. (2006) and Wainwright et al. (2011), respectively.

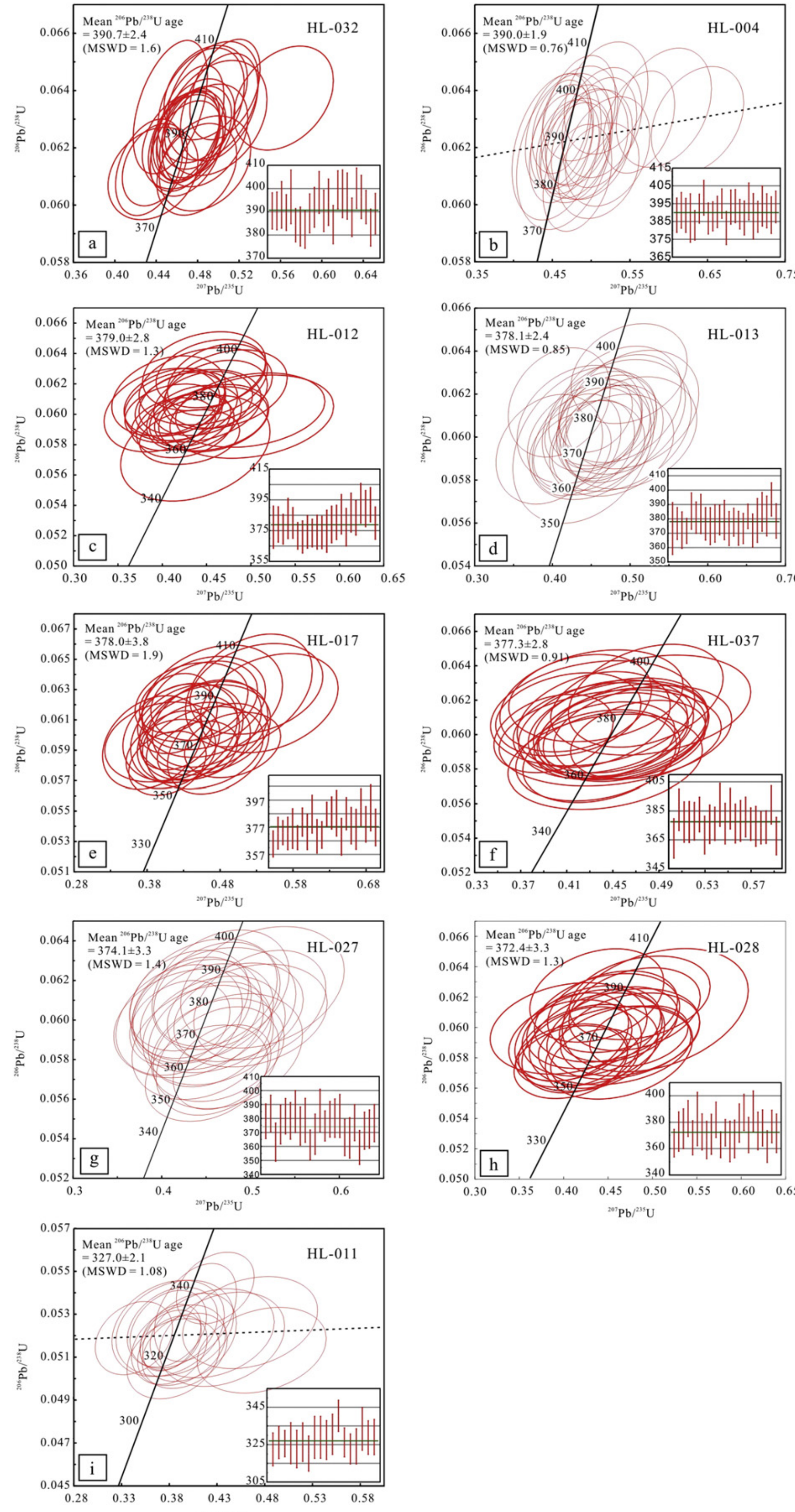

Fig. 8. Concordia plots and age data bar charts from zircon LA–ICP-MS U–Pb data of the intrusions at Halasu porphyry copper belt.

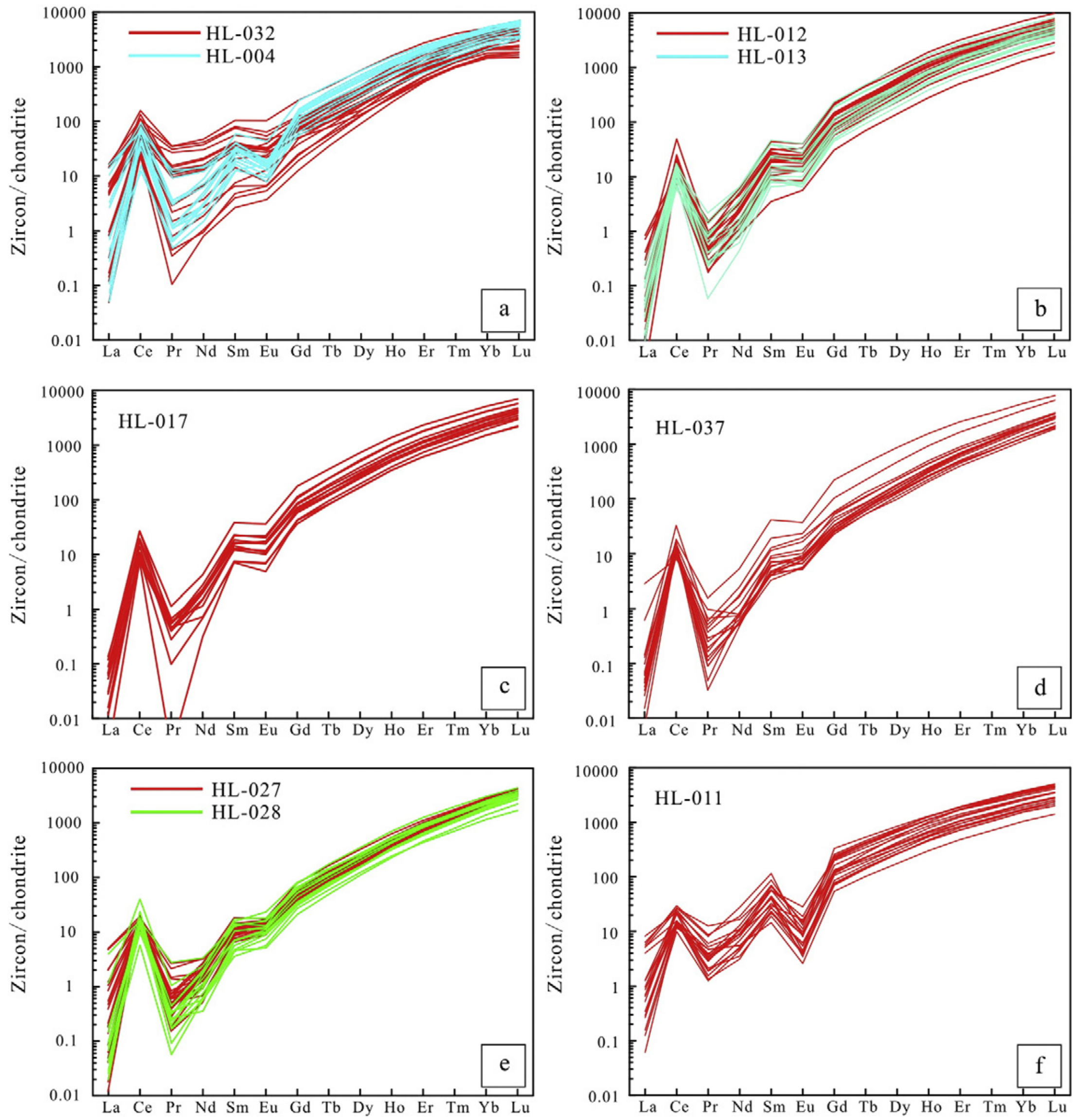

Fig. 9. Chondrite normalized REE patterns of zircon grains from the Halasu porphyry copper belt. The normalizing values are from Sun and McDonough (1989).

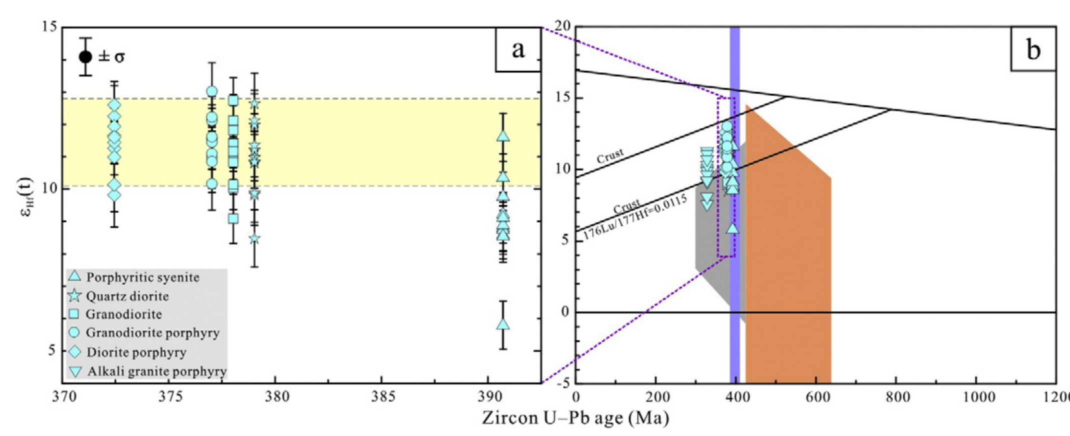

Fig. 10. Relationship between εHf(t) values and U–Pb ages for zircon grains from the intrusions in the Halasu belt. The brown field represents εHf(t) data before 420 Ma and the gray field represents εHf(t) data after 420 Ma in the Chinese Altai, while the light blue stands for the transition of εHf(t) values around 400 Ma in the East Junggar (Sun et al., 2009; Cai et al., 2011; Xu et al., 2013).

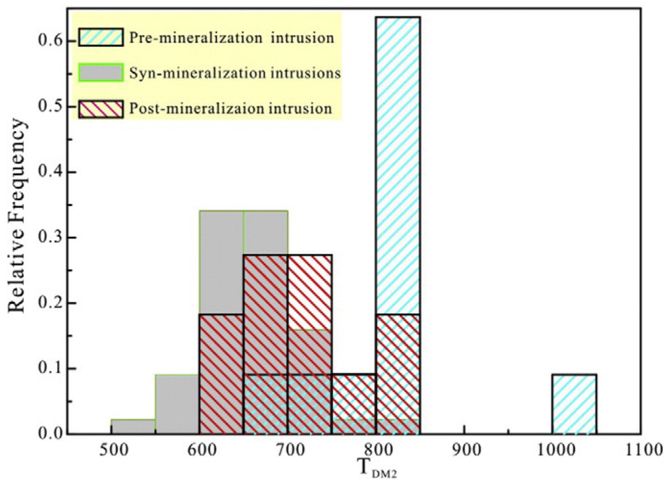

Fig. 11. Hf isotope crustal model age (T_{DM2}) histogram for zircon grains from the intrusions in Halasu belt.

microscope. Zircon grains, generally more than 200 for each sample, were mounted in epoxy and polished down to near half section to expose internal structures. Cathodoluminescence (CL) images were taken for all grains. U–Pb dating and trace element analyses were conducted synchronously using LA–ICP-MS. Sample mounts were placed in a special sample cell designed by Laurin Technic Pty. Ltd, flushed with Ar and He. Laser ablation was accomplished using a pulsed Resonetic 193 nm ArF excimer laser, operated at a constant energy of 80 mJ, with a repetition rate of 8 Hz and a spot diameter of 31 μm. The ablated aerosol was carried to an Agilent 7500a ICP-MS by He gas (Tu et al., 2011). NIST SRM 610 glass (Pearce et al., 1997; Gao et al., 2002) and Temora zircon standards (Black et al., 2003) were used as external standards. The calculation of zircon isotope ratios and zircon trace elements was performed using ICPMSDataCal 7.0 (Liu et al., 2008). Zircon Ce anomalies were calculated using the method based on lattice strain model (Ballard et al., 2002) and the zircon age was calculated using Isoplot (Ludwig, 2003). LA–ICP-MS U–Pb zircon data are presented in Appendix Table A3.

4.4. Zircon Lu–Hf isotopes

In situ zircon Lu–Hf isotopic measurements were undertaken using the Nu plasma high resolution MC–ICP-MS, equipped with a Geolas 193 nm ArF Excimer laser on selected dated zircon grains at Guangzhou Institute of Geochemistry, Chinese Academy of Sciences. A laser repetition rate of 10 Hz at 100 mJ was used and spot sizes were 32 μm. Raw count rates for ^{172}Yb, ^{173}Yb, ^{175}Lu, ^{176}(Hf + Yb + Lu), ^{177}Hf, ^{178}Hf, ^{179}Hf, ^{180}Hf and ^{182}W were collected and isobaric interference corrections for ^{176}Lu and ^{176}Yb on ^{176}Hf were precisely determined. ^{176}Lu was calibrated using the ^{175}Lu value and the correction was made to ^{176}Hf. The zircon standards adopted to evaluate the accuracy of the laser-ablation results during experimentation were Penglai zircon whose ^{176}Hf/^{177}Hf was 0.282888 ± 0.000024 (2SD). Full details of analytical methods are provided in Wu et al. (2007). The $(^{176}Hf/^{177}Hf)_i$ and εHf(t) values were calculated by using the chondrite values recommended by Bouvier et al. (2008). The two-stage model ages, assuming that the parental magma was produced from an average continental crust derived from depleted mantle, were calculated by using values recommended by Griffin et al. (2002). The results of zircon Lu–Hf isotopic analyses are listed in Appendix Table A4.

5. Results

5.1. Whole-rock major and trace elements

Porphyritic syenite and alkali granite porphyry samples display a similar range of K_2O contents, K_2O/Na_2O and A/CNK ratios. For trace elements, they are characterized by different total REE content and Eu anomalies with the alkali granite porphyry exhibiting marked negative Eu anomalies, although they display similar highly incompatible trace elements enrichment and flat HREE patterns (Fig. 5a, b).

Quartz diorite samples are characterized by intermediate SiO_2 (57.1–61.7 wt.%), low to intermediate K_2O contents (1.1–2.1 wt.%) (Fig. 4) and A/CNK ratios of 0.7–1. They also show calc-alkaline characteristics with K_2O/Na_2O ratios ranging from 0.2 to 0.5. The samples are enriched in highly incompatible trace elements including the light rare earth elements (LREE), and large-ion lithophile elements (LILE: Rb, K, Sr), but are depleted in Nb, Ta, Hf and Ti relative to neighboring REE on the trace element spidergrams (Fig. 5c, d).

Granodiorite porphyry samples are characterized by a relatively narrow range of SiO_2 (60.7–64.3 wt.%), but a wide range of K_2O (0.7–3.3 wt.%), which is probably caused by variable alteration. This alteration effect is supported by the wider range for K_2O contents than Nb/Y ratios in Fig. 4. The samples are LREE enriched with relative low HREE and no Eu anomalies. The high Sr contents (average 300 ppm) together with the relatively low Y abundances (average 6 ppm), result in moderate Sr/Y ratios (26–58). They

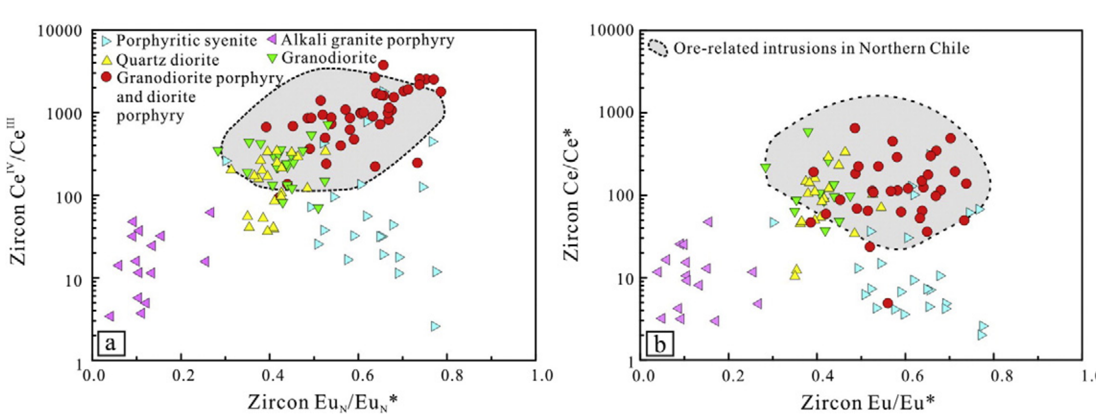

Fig. 12. Zircon Ce^{IV}/Ce^{III} vs. Eu_N/Eu_N* (a) and Ce_N/Ce_N* vs. Eu_N/Eu_N* (b) diagrams constructed using individual zircons from intrusions in Halasu belt. The data range of ore-related intrusions in Northern Chile is from Ballard et al. (2002) and Muñoz et al. (2012).

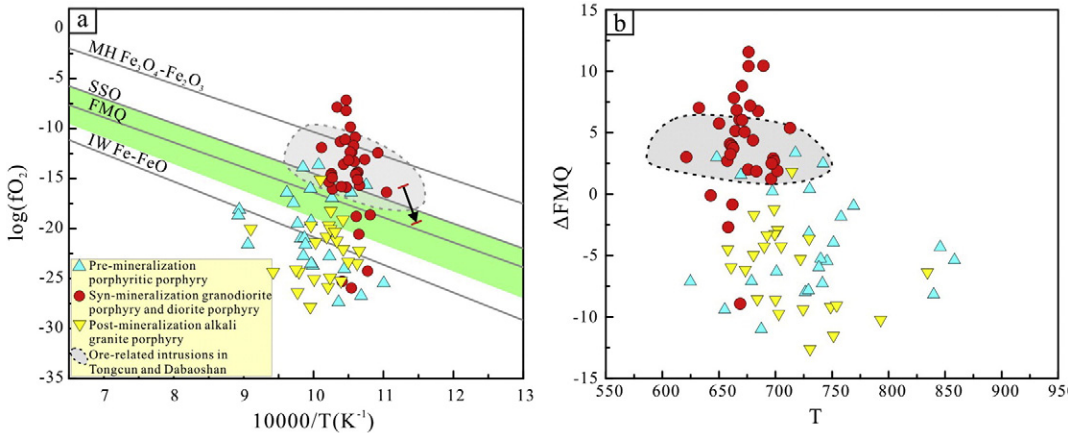

Fig. 13. Magma oxidation states in Halasu belt indicated by logfO_2 (a) and ΔFMQ (b). The base map is from Mungall (2002) and Trail et al. (2012) and the data of Tongcun porphyry molybdenum deposit are from Qiu et al. (2013). Note that the cooling of magma will change the oxidation state and cross SO_3–H_2S boundary.

display notable depletions in high field strength elements (HFSE) such as Nb and Ta, but various enrichment of LILE. However, granodiorite displays slightly high SiO_2 (64.6%) but similar K_2O (3.1%) content and trace elements pattern with the granodiorite porphyry (Fig. 5e, f).

Diorite porphyry samples display narrow SiO_2 content range (60.1–61.4 wt.%), intermediate to high K_2O contents (2.4–3.3 wt.%) (Fig. 4). They show light LREE enrichment with the $(La/Yb)_N$ ranging from 3 to 3.5, and insignificant europium anomalies ($Eu/Eu^* =$ 0.8–0.9). Moreover, the samples also exhibit enrichment in LILE (Rb, Ba, Sr), but markedly depleted in HFSE, especially Nb, Ta and Hf (Fig. 5g, h).

5.2. Whole-rock Sr–Nd–Pb isotopes

The Sr–Nd–Pb isotope compositions of the Halasu porphyry copper belt are illustrated in Figs. 6 and 7. The Sm, Nd, Rb, and Sr concentrations and zircon U–Pb ages were used to calculate the initial isotope compositions at the time of magma crystallization to constrain the petrogenesis of the intrusions. All samples are characterized by relatively low initial $^{87}Sr/^{86}Sr$ ratios ranging from 0.703935 to 0.707172 and high εNd(t) values varying from 4.7 to 5.6. The granodiorite sample has similar Sr–Nd isotope compositions to the younger ore-bearing diorite porphyry and lies close to the depleted mantle range along the mantle array (Fig. 6). The sample from the alkali granite porphyry has similar εNd(t) values but distinct initial $^{87}Sr/^{86}Sr$ ratio of 0.707172 to the ore-related diorite porphyry (Fig. 6). The initial $^{206}Pb/^{204}Pb$, $^{207}Pb/^{204}Pb$, and $^{208}Pb/^{204}Pb$ ratios of the samples are 15.617–18.269, 15.337–15.483 and 37.309–37.667, respectively. The Pb isotope compositions are generally uniform and plot close to the mantle line in the plumbotectonic diagram (Zartman and Doe, 1981; Fig. 7) except sample HL-028, whose $^{206}Pb/^{204}Pb$ value of 15.617 is much less than other samples. The Pb isotope values of samples from the Halasu porphyry copper belt plot within the field of India and Pacific MORB, similar to the porphyries in Oyu Tolgoi porphyry Cu deposit and Tuwu–Yandong Cu deposits, and have mantle-derived Pb characteristic. Compared with the uniform Pb isotope ratios of whole-rock, the Pb isotope compositions of sulfide in ore analyzed by Xue et al. (2010) show significant variability and plot discretely (Fig. 7).

5.3. Zircon U–Pb ages

The results of LA–ICP-MS U–Pb zircon analyses for intrusive rocks (porphyritic syenite, alkali granite porphyry, quartz diorite, granodiorite, granodiorite porphyry, and diorite porphyry) in the Halasu belt are illustrated on concordia diagrams (Fig. 8). Errors on individual analyses are cited at the 1σ level, and the weighted mean $^{206}Pb/^{238}U$ ages are quoted at the 95% confidence level. Concentrations of U and Th range from 43 to 3293 and from 17 to 6503 ppm, respectively, with Th/U values ranging from 0.2 to 5.2, most of which are great than 0.4 and support a magmatic origin (often > 0.4) (Wu and Zheng, 2004).

Zircon grains from porphyritic syenite (samples HL-004 and HL-032) are generally prismatic, colorless or light brown, transparent and euhedral. The majority of grains from the two samples are 40–120 μm in length and 20–40 μm in width with aspect ratios between 1 and 3. The Th/U ratios of sample HL-004 and sample HL-032 vary from 0.4 to 1.2 and from 0.2 to 0.6, respectively. Twenty-three spot analyses from HL-032 yielded concordant results with a weighted mean $^{206}Pb/^{238}U$ age of 390.7 ± 2.4 Ma (MSWD = 1.6; Fig. 8a), similar to the sample HL-004 weighted mean 390.0 ± 1.9 Ma with MSWD = 0.76 defined by twenty-three spots (Fig. 8b). The ages for samples HL-004 and HL-032 are interpreted as the crystallization age of the porphyritic syenite in Halasu III and Yulekenhalasu ore districts, respectively.

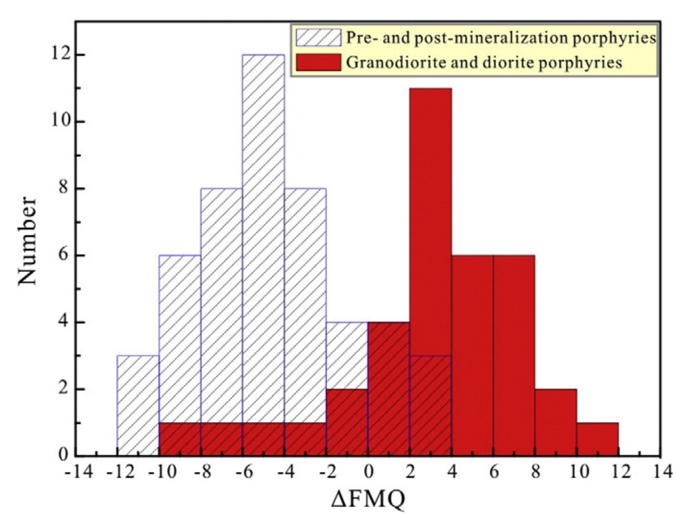

Fig. 14. Histograms of ΔFMQ values for intrusions in Halasu belt.

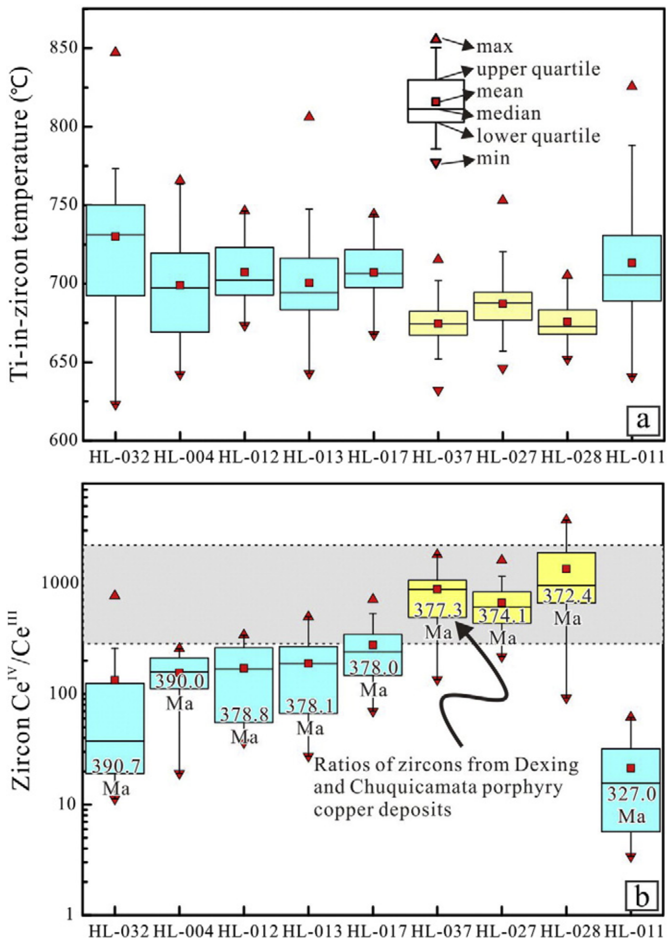

Fig. 15. Boxplots of the Ti-in-zircon temperatures (a) and zircon Ce^{IV}/Ce^{III} ratios (b) for intrusions in Halasu belt. Note that temperatures decrease with time while Ce^{IV}/Ce^{III} values demonstrate reverse trend in syn-mineralization intrusions. Data ranges of Dexing and Chuquicamata porphyry copper deposits are from Ballard et al. (2002) and Li et al. (2012).

Zircon grains from quartz diorite (samples HL-012 and HL-013) are colorless, transparent and generally euhedral, with lengths ranging from 80 to 150 μm and length/width ratios from 1 to 6. The Th/U ratios of the sample HL-012 and sample HL-013 vary from 0.4 to 0.7 and from 0.3 to 1.3, respectively. Twenty-two spot analyses from HL-012 define a weighted mean $^{206}Pb/^{238}U$ age of 379.0 ± 2.8 Ma with MSWD = 1.3 (Fig. 8c), whereas sample HL-013 of 378.1 ± 2.4 Ma (MSWD = 0.85; Fig. 8d) from twenty-three grains. The ages are interpreted to represent the crystallization age of the quartz diorite in Halasu II ore district.

Zircon grains from the granodiorite (HL-017) and granodiorite porphyry (HL-037) are generally prismatic, colorless or light brown, transparent and euhedral. Most grains range in length from 60 to 160 μm. The Th/U ratios of sample HL-017 and ore-bearing sample HL-037 vary from 0.34 to 1.06 and from 0.40 to 0.86, respectively, support their magmatic origin. Twenty-two grains from sample HL-017 defined a weighted mean $^{206}Pb/^{238}U$ age of 378.0 ± 3.8 Ma (MSWD = 1.9; Fig. 8e), while twenty-one grains from sample HL-037 yielded a weighted mean $^{206}Pb/^{238}U$ age of 377.3 ± 2.8 Ma (MSWD = 0.91; Fig. 8f). The ages from samples HL-017 and HL-037 are interpreted to record the emplacement age of granodiorite in Halasu II district and granodiorite porphyry in Yulekenhalasu ore district.

Zircon grains from the diorite porphyry (samples HL-027 and HL-028) are colorless, transparent, and generally euhedral, with lengths ranging from 50 to 140 μm and length/width ratios from 1.5 to 3. The Th/U ratios of the samples vary from 0.4 to 1.7. Twenty-three spot analyses from HL-027 define a weighted mean $^{206}Pb/^{238}U$ age of 374.1 ± 3.3 Ma (MSWD = 1.4) (Fig. 8g), slightly earlier than the sample HL-028 of 372.4 ± 3.3 Ma defined by twenty-three spots (MSWD = 0.85; Fig. 8h) and represents the crystallization age of the diorite porphyry in Dunke'erman ore deposit.

Zircon grains from alkali granite porphyry (sample HL-011) are euhedral and elongate with lengths ranging from 60 to 200 μm and length/width ratios from 1.5:1 to 4:1. The Th/U ratios of the zircon grains range from 0.26 to 0.66, herein suggesting a magmatic origin. Nineteen spots on sample HL-011 yielded a weighted mean $^{206}Pb/^{238}U$ age of 327.0 ± 2.1 Ma with MSWD = 1.1 (Fig. 8i), which is considered to record the crystallization age of alkali granite porphyry in Halasu III ore district.

5.4. Zircon geochemistry

Trace element data for zircon grains from nine samples are plotted in Fig. 9 with the full data set presented in Appendix Table A5. Most of the zircon grains are depleted in LREE and enriched in HREE on chondrite

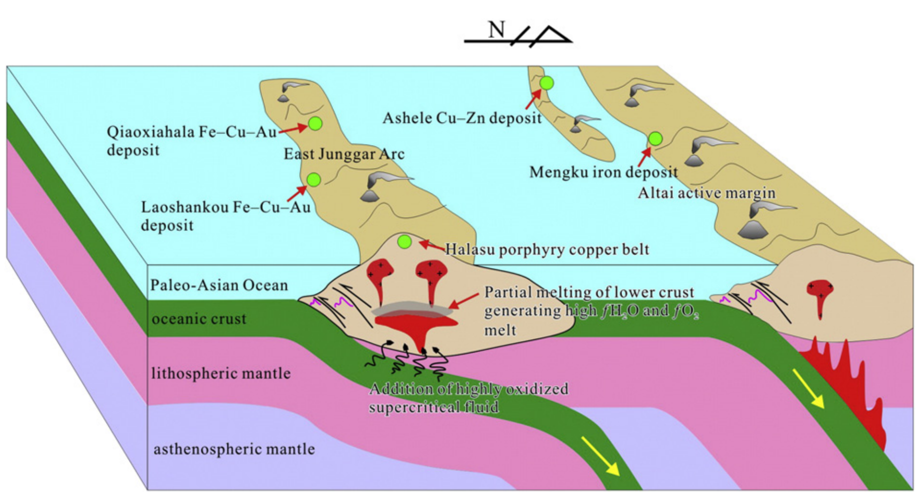

Fig. 16. Tectonic setting for the Late Paleozoic mineralization in Halasu belt and adjacent Chinese Altai region, modified from Long et al. (2010) and Xiao et al. (2014). The intra-ocean flat subduction induced melting in high fO_2 and fH_2O condition generates fertile parental magma, which may account for the porphyry mineralization in shallow depth in Halasu porphyry copper belt (see text for details).

normalized patterns and are characterized by positive Ce anomalies with variable negative Eu anomalies.

Zircon grains from the porphyritic syenite (HL-032) has Ce_N/Ce_N^* and Eu_N/Eu_N^* ratios between 2–100 and 0.3–0.8, respectively, whereas HL-004 has Eu_N/Eu_N^* ranging from 0.2 to 0.6 and Ce_N/Ce_N^* of 1–240. For the quartz diorite samples, zircon grains from sample HL-012 display Ce anomalies ranging from 10 to 335 and Eu anomalies of 0.3–0.6 and the grains in HL-013 show Eu_N/Eu_N^* range of 0.2–0.6 and Ce_N/Ce_N^* range of 30–225. The zircon grains of granodiorite from sample HL-017 are characterized by the Ce and Eu anomalies varying between 4–590 and 0.3–0.5, respectively. Zircon grains from the granodiorite porphyry (HL-037), have Ce anomalies of 5–650 and Eu anomalies of 0.4–0.7. The zircon grains in samples HL-027 and HL-028 from the diorite porphyry are characterized by the Eu_N/Eu_N^* ratios of 0.5–0.7 and 0.4–0.8, respectively, whereas Ce_N/Ce_N^* ranges from 5 to 200 and 5 to 220, respectively. Zircon grains from alkali granite porphyry (sample HL-011), display strong negative Eu anomalies and slightly positive Ce anomalies (0.1 to 0.3 and 1 to 50 respectively).

Zircon Ce^{IV}/Ce^{III} ratios are primarily used as a measure of the oxidation state of the magma (Ballard et al., 2002; Liang et al., 2006; Li et al., 2012). The calculated Ce^{IV}/Ce^{III} ratios demonstrate a wide range from 3 to 2500 in general. However, compared with the barren intrusions (samples HL-004, HL-011, HL-012, HL-013 and HL-032) and intrusions with insignificant mineralization (sample HL-017), of which the Ce^{IV}/Ce^{III} ratios vary from 3 to 800 with the average values of 160 for HL-004, 20 for HL-011, 170 for HL-012, 190 for HL-013, 130 for HL-032, 290 for HL-017, the ratios of mineralized granodiorite porphyry (sample HL-037) and diorite porphyry (samples HL-027 and HL-028) ranging from 140 to 2600 with an average of 970, are much wider and higher.

Because of the temperature dependant incorporation of Ti^{4+} into crystallizing zircon (Watson et al., 2006; Ferry and Watson, 2007), temperatures of magma in the Halasu porphyry copper belt are estimated using the Ti-in-zircon thermometer. The activity of both silica and titanium is set to 1, due to the presence of quartz as dominant mineral phase in rocks and rutile as inclusions in zircon grains. The nine samples, whose Ti concentrations range from 3 to 20 ppm, yield temperature range of 620–830 °C for sample HL-032, 650–740 °C for sample HL-004, 670–730 °C for sample HL-012, 640–810 °C for sample HL-013, 670–740 °C for sample HL-017, 630–720 °C for sample HL-037, 650–750 °C for sample HL-027, 650–710 °C for sample HL-028, and 640–830 °C for sample HL-011, respectively, which are within the general range of intermediate to felsic igneous rock crystallization temperature (653 ± 124 °C) (Fu et al., 2008). Moreover, the average temperatures of ore-bearing porphyries, including the samples HL-027 (average = 685 °C), HL-028 (average = 680 °C), and HL-037 (average = 675 °C), are obviously lower than barren samples, whose average temperatures are higher than 700 °C.

5.5. Zircon Lu–Hf isotopes

In situ zircon Hf isotope compositions from six samples with the εHf(t) and crustal model age values calculated using corresponding U–Pb age of grains are illustrated in Figs. 10 and 11. The Hf isotopic compositions are characterized by high initial $^{176}Hf/^{177}Hf$ ratios that range from 0.282718 to 0.282920 with corresponding εHf(t) values varying from 5.8 to 13.0. However, zircon grains from the porphyritic syenite (sample HL-032) demonstrate similar εHf(t) values (average = 9.1) to the alkali granite porphyry (sample HL-011), but relatively lower Hf isotope compositions with εHf(t) values ranging from 5.8 to 11.6 than other samples. The thirteen grains from the quartz diorite (sample HL-012) yield uniform εHf(t) values of 8.5–12.7 with crustal model ages varying from 555 to 844 Ma. Similarly, thirty-one zircon grains from syn-mineralization intrusive rocks (samples HL-017, HL-028, and HL-037) demonstrate remarkably homogeneous Hf isotope compositions with the εHf(t) values ranging from 9.1 to 12.8, 9.8 to 12.6, and 10.2 to 13.0, respectively, corresponding to crustal model ages of 540–740 Ma. Eleven zircon grains from the post-mineralization alkali granite porphyry (sample HL-011) yielded εHf(t) values of 7.6–11.3 and the crustal model age ranges from 615 to 822 Ma with average values of 9.74 and 714 Ma, respectively.

6. Discussion

6.1. Episodes of porphyry mineralization-related magmatism in Halasu and adjacent area

The nine new U–Pb ages generated in this study, when combined with published work (Xiang et al., 2009; Zhao et al., 2009b; Xue et al., 2010; Yang et al., 2012c), can be used to distinguish three periods of magmatism, of which the porphyritic syenite (samples HL-032 and HL-004) and the alkali granite porphyry (sample HL-011) are the first lithotypes to be identified of their ages in Halasu porphyry copper belt. Previous research in Halasu belt have determined the timing of copper and molybdenum mineralization by Re–Os isotopic dating of molybdenite samples separated from orebodies in Yulekenhalasu and Halasu I ore districts, with the former yielding ages of 373.9 ± 2.2 Ma and the latter 376.9 ± 2.2 Ma, slightly younger than the syn-mineralization porphyries (Xue et al., 2010; Yang et al., 2012c). Based on the spatial and temporal relationship with mineralization, the magmatism can be divided into three periods: pre-mineralization activity at ~390 Ma, syn-mineralization activity of 382–372 Ma, and post-mineralization activity of 350–320 Ma. The pre-mineralization group, including the porphyritic syenite discovered in the Yulekenhalsu and Halasu III ore districts, was emplaced at ~391 Ma, approximately 15 m.y. earlier than mineralization. The syn-mineralization intrusions range from 382 to 372 Ma and consist of a wide phase range of granitoids including quartz diorite, granodiorite, granodiorite porphyry and diorite porphyry with the latter two hosting major orebodies. The post-mineralization groups are composed of ~348 Ma quartz porphyry and 327 Ma alkali granite porphyry.

During the Late Paleozoic, the Laoshankou and Qiaoxiahala Fe–Cu–Au deposits also formed in the East Junggar. Although they are significantly different to the Halasu porphyry copper belt in mineral associations, they are synchronous with mineralization at Halasu during 370–380 Ma (Lü et al., 2012; Li et al., 2014) and consistent with a subduction-related tectonic framework.

Based on regional research in the adjacent Chinese Altai, near continuous magmatism occurred from the Ordovician to the Jurassic, peaking at ca. 500 Ma, 470–440 Ma, 425–360 Ma, 355–318 Ma, 290–270 Ma, and 245–190 Ma (Wang et al., 2010). The Late Silurian to Devonian interval in the Chinese Altai can be further subdivided into two periods of 425–390 Ma and 380–360 Ma (Han, 2008; Wang et al., 2010) and corresponding to the pre- and syn-mineralization magmatism in the Halasu porphyry copper belt. Furthermore, during the 425–360 Ma, mineralization in the Chinese Altai, including the Ashele VMS-type Cu–Zn deposit (Song et al., 2010; Wan et al., 2011) and the Mengku iron deposit (Xu et al., 2010; Yang et al., 2010a), are considered to have formed in arc-related settings. Similarly, the giant Oyu Tolgoi porphyry Cu–Au deposit in Mongolia, with a mineralization age of 373–370 Ma, consists of syn-mineralization quartz monzodiorite and granodiorite emplaced in the Late Devonian followed by post-mineralization syenite porphyry emplaced at the Late Carboniferous (Wainwright et al., 2011), suggesting a close temporal and tectonic relationship with the Halasu porphyry copper belt. Furthermore, zircon overgrowth rims and recrystallized domains from high-grade metamorphic rocks occurring in the Chinese Altai, with close genetic links to geodynamic events, give consistent ages of 390 Ma (Jiang et al., 2010), which is interpreted to record a high temperature metamorphic event associated with the Devonian magmatism. In summary, corresponding to magmatic framework in adjacent Chinese Altai, the Devonian to Early Carboniferous magmatic activity plays a critical role in the formation of Halasu porphyry copper belt.

6.2. Genesis of highly oxidized porphyry-Cu mineralization related magmatism

6.2.1. Highly oxidized intrusions in Halasu belt

The Eu_N/Eu_N^* vs. Ce^{IV}/Ce^{III} and Eu_N/Eu_N^* vs. Ce_N/Ce_N^* zircon data of syn-mineralization intrusions from the Halasu porphyry copper belt plot mainly within the range defined by zircon grains from ore-related intrusions in northern Chile (Fig. 12). However, among the syn-mineralization intrusive rocks, the ore-bearing intrusions (granodiorite porphyry and diorite porphyry) have higher Eu_N/Eu_N^* and Ce^{IV}/Ce^{III} ratios than the barren ones (quartz diorite and granodiorite), suggesting that the ore-bearing porphyries are more oxidized although syn-mineralization barren intrusions show indistinguishable elevated Ce_N/Ce_N^* ratios with ore-bearing ones (Fig. 12b). The Eu_N/Eu_N^* ratios demonstrate positive correlation with Ce_N/Ce_N^* and Ce^{IV}/Ce^{III} ratios, respectively, despite of the pre-mineralization porphyritic syenite that is characterized by high Eu_N/Eu_N^* but low Ce_N/Ce_N^* and Ce^{IV}/Ce^{III} ratios (Fig. 12). The wide range of negative Eu_N/Eu_N^* anomalies (Fig. 12) in the porphyritic syenite suggest that Eu_N/Eu_N^* is not only controlled by the oxygen fugacity, but also influenced by crystallization or assimilation of plagioclase in the magma (Hoskin and Ireland, 2000; Hoskin and Schaltegger, 2003), suggesting a slightly different magma origin or evolution path for the porphyritic syenite compared with the syn-mineralization intrusions. The oxygen fugacity (fO_2), calculated from the Ce_N/Ce_N^* and Ti-in-zircon temperatures (Trail et al., 2011, 2012; Qiu et al., 2013), herein provides practical measure for the oxidization state of magma. When plotted on the 10000/T vs. $\log(fO_2)$ and T vs. ΔFMQ diagrams (Fig. 13), the zircon grains from ore-bearing porphyries (granodiorite porphyry and diorite porphyry) mainly fall above FMQ buffer, whereas those from the pre- or post-mineralization intrusions plot generally below the ore-bearing ones, consistent with the analyses results of Ce^{IV}/Ce^{III} ratios. The conclusion that ore-bearing porphyries are more oxidized, is further supported by the statistics of ΔFMQ values because peak of ore-bearing porphyry ($\Delta FMQ = 2.5$) is obviously 7 to 8 log units higher than that in pre- or post-mineralization intrusions (Fig. 14).

It has been widely accepted that there exists a genetic link between oxidized magma and copper mineralization in plate convergent margin (Sillitoe, 1972, 2010; Gustafson and Hunt, 1975; Hedenquist and Lowenstern, 1994; Sun et al., 2004; Richards, 2009). The nature of the link is generally construed to be that high fO_2 results in the silicate magma remaining sulfide undersaturated during the evolution of magma, thus preventing the escape of chalcophile elements, which will otherwise prefer to participate in the sulfide melt rather than the silicate magma (Mungall, 2002; Mungall et al., 2006). In Halasu the granodiorite porphyry and diorite porphyry have high Ce^{IV}/Ce^{III} ratios, ΔFMQ values and corresponding high fO_2, which may have undergone less loss of chalcophile elements and accumulated more copper, resulting in higher mineralization potential than intrusions with low Ce^{IV}/Ce^{III} ratios.

6.2.2. Mechanism for high oxidizing state of magmas at Halasu

The Ti-in-zircon temperatures decrease systematically with time whereas Ce^{IV}/Ce^{III} ratios show a broad increase over time (Fig. 15). This trend provides new insights into the relationship between magmatic temperature, oxidization state, and water content in the Halasu porphyry copper belt.

Magma temperatures have been shown to be closely associated with the water content (Mysen and Boettcher, 1975; MuÈntener et al., 2001; Grove et al., 2006), for example, the temperatures of magma generated by low fH_2O melting is generally higher than those produced by high fH_2O melting which occurs in the magma reservoir before water saturation. Similar correlations between fH_2O and fO_2 measured by Fe^{3+}/Fe^{2+} have been observed in granitoids (Czamanske and Wones, 1973; Tepper et al., 1993), therefore, the fH_2O, is considered as the bridge to connect magma temperature and fO_2.

Specified mechanism between high fH_2O and fO_2, however, remains controversial, mainly including the H_2 separation and sulfur loss models proposed to explain the close association. According to the H_2 escape model, the release of H_2 from the magma causes the increase of relative O_2 amount in the residual magma (Henley and McNabb, 1978; Eastoe, 1982). However, this is only true in open system and that process of spontaneous separation of H_2 relative to O_2 into spatially separated reservoir (Brandon and Draper, 1996) from previously homogeneous system will violate the second law of thermodynamics (Mungall, 2002). Alternatively the sulfur loss model, could more reasonably explain the genetic link between high fH_2O and fO_2 as expressed by the following formulae:

$$SO_{3(aq)} + H_2O_{(aq)} = H_2S_{(aq)} + 2O_{2(g)}$$

$$6FeO + O_2 = 2Fe_3O_4$$

$$8FeO + SO_3 + H_2O = 4Fe_2O_3 + H_2S.$$

In this model, high fH_2O makes it easier for wet magma to gain water saturation (Shinohara, 1994; Candela, 1997; Robb, 2009) allowing the H_2S to separate from the magma by a flow of aqueous fluid which may react with chalcophile elements to precipitate sulfides under such conditions (Dilles, 1987). As a result, the decrease of H_2S, along with the high water content, will drive reaction to the right to increase the content of O_2, therefore, the magma will maintain a highly oxidized state during ascent. In addition, the oxidization of Fe^{2+} may have a reverse effect on the system because the consumption of O_2 or SO_3 will result in an increase of relative H_2S abundance and decrease of fO_2, causing the precipitation of sulfides in the mineralization stage. This mineralization hypothesis is illustrated in $\log(fO_2)$ vs. 10000/T diagram: during the progressive cooling of magma, the crystallization of magnetite will contribute to the original hydrous oxidizing fluid evolving across the SO_3–H_2S boundary (SSO) and entering the H_2S domain field (Fig. 13a), which means a redox transition. This model is consistent with the field observations of Halasu belt, for example, high biotite concentrations in the ore-related diorite porphyry are consistent with high fH_2O magmas. Moreover, the general occurrence of magnetite veins in the potassic zone which is closely related to orebodies supports the view that the crystallization of magnetite changes the oxidization state of aqueous fluid. In summary, the combined analyses of temperature, water content and oxygen fugacity of the magma, support the magma becomes more oxidized with time due to the progressive enrichment in water content, thus resulting in the higher mineralization potential of late stage diorite porphyry and granodiorite porphyry in the Halasu porphyry copper belt.

Some geochemical features of syn-mineralization intrusions at Halasu belt are similar to adakitic rocks, which are considered to be formed by partial melting of subducted oceanic slab by Yang et al. (2005). However, this conclusion remains controversial because many porphyries, including some syn-mineralization porphyries at Halasu belt have high HREE (Y and Yb) contents thus exhibit normal island arc signatures rather than typical adakitic affinities (Feng and Zhang, 2009; Yang et al., 2014). Since the syn-mineralization intrusive rocks are characterized by high water fugacities, we propose a model that incursion of highly oxidized supercritical fluids from the slab into the lower crust was ultimately responsible for the generation of hydrous parental magma, which is similar to the model by Bissig et al. (2003) documented in the Central Andes and generally described in details by Mungall (2002). According to this model, we propose that it is probably the highly oxidized supercritical fluid that triggered the partial melt of basic crust and consequently produced the high fH_2O and fO_2 parental magma.

The addition of supercritical fluid could have resulted from the flat subduction of PAO (Paleo-Asian Ocean) slab beneath the Junggar arc. This process permits the production of low temperature melts at around 900 °C (Prouteau et al., 1999), consistent with the low temperature affinity of syn-mineralization intrusions at Halasu belt. Moreover, in accordance with the model proposed by Bissig et al. (2003), the input of slab-derived highly oxidized supercritical fluid will trigger partial melting of basic lower crust in high oxidation state, destabilize sulfide phases in the lower crust or subducted slab, and carry important complex agents (Cl and S) for mineralization. Because of the flat subduction, the interaction between the mantle and the supercritical fluid may be restricted to limited extent and much of the fluid-extracted metals from slab are transported into the source of the parental magma, which is favorable for mineralization.

Likewise, Yin et al. (2015) reported the Early Carboniferous calc-alkaline volcanic rocks and I-type granitic intrusions are petrochemically distinct from the Late Carboniferous–Middle Permian granites in the West Junggar and are characterized by low Ti-in-zircon temperatures (689–857 °C), whereas the Late Carboniferous–Middle Permian granites show obviously high Ti-in-zircon temperatures (833–1032 °C) (Zhou et al., 2008). Yin et al. (2015) proposed that the flat subduction of the PAO slab is accounted for the generation of "cold" magma in the Early Carboniferous, whereas upwelling of hot asthenosphere caused by ridge subduction during the Late Carboniferous–Early Permian triggered the formation of granites, together with the coeval charnockites, sanukites, tholeiites, and adakite–magnesian diorite (Tang et al., 2010).

6.3. Implications for sources of regional and Halasu magmatism and tectonic evolution

6.3.1. Sources of magmas

As is revealed by experimental study, most granitoid magmas are derived from middle and lower crustal depth (Rapp et al., 1991; Grochau and Johannes, 1997; Holtz et al., 2001) and therefore the sources of magma in Junggar may originate from partial melting of basic lower to middle crust comprising the Early Paleozoic oceanic crusts and island arcs. Furthermore, the fH_2O may have an influence on the partial melting process because increased fH_2O during melting can increase the amount of amphibole but decreases the amount of plagioclase in the residuum (Beard and Lofgren, 1991; Waight et al., 1998). Allowing for the fH_2O effect, the low average Eu anomalies of syn-mineralization intrusions and marked concave upward REE patterns in ore-bearing granodiorite porphyry imply that their parental magmas were resulted from higher fH_2O partial melting relative to pre- or post-mineralization intrusions.

The broadly similar Sr–Nd isotope compositions of the Halasu intrusions suggest that the pre-, syn- and post- mineralization intrusions shared the similar magma source region (Fig. 15b), in spite of the fact that Sr composition locally vary much in Halasu belt and even in the East Junggar region resulted from the high mobility. Moreover, although it's hard to estimate the proportions of juvenile component in Junggar because the lack of distribution of lithology, those of individual intrusions can, however, be calculated reasonably well using a simple mixing equation (Faure, 1986), which has been carried out in adjacent Chinese Altai and other areas in CAOB by Jahn (2004) and Wang et al. (2009). In this study, the granitoids in Halasu are assumed to be derived by mixing of two end-member sources: namely the mantle-derived basaltic rocks and the preexisting Precambrian component. Based on this mixing model, most samples of intrusions from Halasu belt show nearly 95% of juvenile materials in reservoir (Fig. 6), thus precluding significant addition of Precambrian crust in partial melting process or assimilation of preexisting crustal materials during the ascent of produced parental magma.

The εHf(t) values from Halasu belt range between 5.8 and 13.0 and record a general enrichment which may either inherit from the source or resulted from contamination process during ascent of parental magma. However, as the result of mixing model is against significant crustal contamination, combined with the similar conclusions obtained via studies in adjacent Chinese Altai by Yuan et al. (2007) and Cai et al. (2011), the high εHf(t) values could represent the nature of source comprising juvenile materials. Furthermore, the pre- and post-mineralization intrusions are characterized by relative lower εHf(t) values than syn-mineralization intrusions although all samples display enriched εHf(t) values (Figs. 11 and 12). This may suggest that the syn-mineralization intrusions are derived from the most juvenile source compared with pre- and post-mineralization intrusions. On the contrary, when taking syn-mineralization intrusions alone into consideration, all samples demonstrate uniform εHf(t) compositions and indicate a continuous and homogeneous magma source for mineralization (Fig. 11), which remains active over a period over 10 m.y. and is identified as favorable condition for the generation of porphyry copper deposits (Muñoz et al., 2012).

Recent workers have highlighted that the significant transition of zircon εHf(t) values in Chinese Altai where zircon εHf(t) values show either positive or negative (−18 to +15) before 420 Ma but became positive only (0 to +15) after that time (Sun et al., 2009). This may indicate the significant addition of juvenile material into regional magma source, which would modify the composition of older source for Chinese Altai. Likewise, similar transition is also identified in the East Junggar region when combining earlier published εHf(t) values of igneous rocks in Taheir tectonic window by Xu et al. (2013) and Halasu by Yang et al. (2014) with our data (Fig. 11). During the Middle to Late Devonian, granitoids locally demonstrate the εHf(t) values ranging from −11 to +15 before 406 Ma (Xu et al., 2013), but change to positive only after approximately 390 Ma according to this study. The generally positive εHf(t) values of pre- and syn-mineralization intrusions in Halasu belt at the north margin of the East Junggar, termed as the peak of magmatic activity, occurred later than the similar transition in Chinese Altai, therefore, possibly represent a similar important magmatism subsequent the strong subduction–accretionary process in Chinese Altai. In other words, the main orogenic process in East Junggar region, marked by the magma source becoming juvenile material dominated, is spatially and temporally associated with, but slightly later than that in Chinese Altai region. This conclusion supports the southward accretionary crustal growth from Chinese Altai to East Junggar region and is consistent with the results of Nd–Sr isotopic mapping in Chinese Altai by Wang et al. (2009).

6.3.2. Regional tectonic evolution

The Halasu porphyry copper belt occurs within the Sawu'er Late Paleozoic oceanic island arc in the northern margin of East Junggar, and is considered to be intimately associated with the basement and evolution history in the Junggar region (He et al., 2004). However, the nature of basement rocks in the Junggar Block is open to debate with the following models: the Precambrian microcontinent (Watson et al., 1987; Wu, 1987), post-collisional mantle-derived mafic rocks (Han et al., 1997, 1999), and fragments of the Paleozoic oceanic crust and arcs (Carroll et al., 1990; Zheng et al., 2007; Xiao et al., 2009b).

The generally positive εNd(t) values and the absence of lower Paleozoic or earlier rocks in Junggar rule out the first model (Chen and Jahn, 2004). The second model, termed as vertical continental growth via underplating of mantle-derived magmas, may account for the generation of post-collision granitoids between 330 and 250 Ma (Han et al., 1999), but fails to explain the widely exposed Middle to Late Paleozoic (390–370 Ma) granites, which are considered to be the result of horizontal continental growth via progressive subduction and arc accretion (Wang et al., 2006). Moreover, the widespread basic to intermediate volcanic and intrusive rocks in Junggar region, which are characterized with geochemical arc affinities (Wang et al., 2006; Zhang et al., 2008), indicate a subduction tectonic setting. Besides, Zhang et al. (2009b) suggested that the Middle Devonian Beitashan Formation, which comprises dominantly tholeiite to calc-alkaline rocks and is characterized by remarkably negative Nb, Ta and Ti anomalies, MORB-like HFSE ratios (Zr/Nb and Sm/Nd) and high εNd(t) values (6.4–7.3), was formed in an island arc setting. This is consistent with the data for Halasu because the whole-rock geochemistry features demonstrate that the arc-related REE patterns and negative anomalies of Ta, Zr and Hf, especially the marked Nb anomalies (Fig. 5), have supra-subduction zone geochemical signatures, and therefore further support an island arc setting for Halasu belt during the Middle to Late Devonian.

Furthermore, according to previous researches in the southern margin of Chinese Altay Mountains (Niu et al., 1999, 2006), the occurrence of juxtaposed Devonian boninite, high-TiO_2 and low-TiO_2 basalts, adakites, which were produced by partial melting of subducted young oceanic crust, together with the cherts, turbidites, and minor gabbros also indicate an island arc setting (Liu et al., 1993; Xu et al., 2003; Niu et al., 2006; Xiao et al., 2009b). Moreover, the tectonic setting of the arcs and intervening seaways in the Paleozoic is further supported by the dismembered ophiolites distributed in the East Junggar region (Xiao et al., 2009b), for example, the Armantai and Kelameili ophiolites, which mark the residues of PAO branches. In addition, on regional scale, the younging shift of Nd model age ranging from Tarim, through Tianshan and Chinese Altai, to Junggar in Paleozoic (Hu et al., 2000), and the young model age (T_{DM}) in Halasu belt support the island arc setting for Junggar whereas the Tianshan and Altai is envisaged as composite terranes with the Tarim as continental segment (Hu et al., 2000).

Since the syn-mineralization intrusions are supposed to be formed by flat subduction in island arc setting, the pre-mineralization magmatism, which is about 10 m.y. predating the syn-mineralization magmatism, is probably corresponding to immature island arc setting produced by normal subduction (Zhang et al., 2009b). The post-mineralization magmatism, however, is consistent with regional magmatism which span over 30 m.y. and is characterized by the A-type granites. These intrusions emplaced in post-orogenic setting and are related to the melting of lower crust due to underplating of mantle-derived mafic magma (Tong et al., 2006). However, there exists a magmatic quiescence between ca. 370 Ma and 350 Ma, with almost no intrusions occurring at Halasu during this interval. This may be attributed to the easing of flat subduction of the PAO slab because prolonged flat subduction will sufficiently cool both lithospheres and the downgoing oceanic slab to an extremely low extend (<600 °C). This will restrain partial melting and therefore generate a volcanic gap (Gutscher et al., 2000).

Based on the discussion above, the sources of magmatism, the mechanism for generation of high oxidation state magma and the genetic link between high fO_2 and Cu mineralization, the tectonic setting for the Late Paleozoic mineralization in Halasu belt and adjacent Chinese Altai region is illustrated in Fig. 16 and described as follows. During the Middle to Late Paleozoic, an arc (East Junggar arc) was built in the PAO via subduction and accretion process. The subsequent addition of oceanic slab-derived supercritical fluid during flat subduction triggered the partial melting of the middle to lower juvenile crust in high fH_2O and fO_2 condition, which is thought to generate the precursor of low temperature and high oxidation state mineralization magma. Then in the Middle Devonian, the metallogenic porphyries were emplaced in the Beitashan Formation and only those porphyries characterized by high enough oxidation state to accumulate elevated chalcophile elements during the ascend of magma, are favorable for bearing economic mineralization at Halasu.

7. Conclusions

(1) The magmatism in Halasu porphyry copper belt covers a time interval of 390 to 320 Ma and is divided into three periods: the pre-mineralization activity of 390 Ma, syn-mineralization activity of 382–372 Ma, and post-mineralization activity of 350–320 Ma. This indicates the Middle Devonian to Early Carboniferous magma activity play a critical role in mineralization of the CAOB.

(2) The negative correlation between Ti-in-zircon temperatures and oxygen fugacity is possibly resulted from the different water fugacities (fH_2O) in early stage of magma evolution and is well corresponding to the fact that late stage syn-mineralization granitoids have higher water content, oxygen fugacity but low temperatures with higher mineralization potential. We propose that the generation of high fH_2O syn-mineralization magmatism is induced by flat subduction of PAO crust beneath East Junggar island arc.

(3) Syn-mineralization intrusions are characterized by remarkably homogeneous Hf isotopic composition over more than 10 m.y., which indicates a stable and long-lived reservoir beneath the ore-bearing porphyries during the Late Devonian. The Sr–Nd–Pb–Hf isotopic study suggests that the magma of all periods is derived from juvenile material dominated reservoir with limited addition of preexisting continental crust during flat subduction of PAO slab. The analyses of magmatism in Halasu belt, coupled with the significant transition of zircon εHf(t) values in Chinese Altai, support the existence of southward accretionary crustal growth from Chinese Altai to East Junggar region.

Acknowledgments

We sincerely appreciate the detailed and constructive reviews and suggestions of Franco Pirajno and two anonymous reviewers, which greatly improved this paper. We thank the No. 4 Geological Party of the Xinjiang Bureau of Geology and Mineral Exploration and Development, for assistance during field work in the Halasu porphyry copper belt. We also appreciate the laboratory assistance guidance offered by Jinlong Ma and Congying Li from Guangzhou Institute of Geochemistry, Chinese Academy of Sciences. This study was financially supported by the Chinese National Basic Research 973-Program (2014CB440802 and 2014CB448000) and Xinjiang Major Basic Research Project (201330121). This is contribution no. IS-2089 from GIGCAS.

Appendix A

Appendix Table A1
Major (wt.%) and trace (ppm) element compositions for the intrusive rocks at Halasu porphyry copper belt.

Sample	Rock name	SiO_2	TiO_2	Al_2O_3	Fe_2O_3	MnO	CaO	MgO	K_2O	Na_2O	P_2O_5	LOI	Total	K_2O/Na_2O	A/CNK	La	Ce	Pr	Nd	Sm	Eu	Gd	Tb	Dy	Ho	Er
HL-002	Granodiorite porphyry	62.94	0.44	16.20	5.19	0.04	1.54	2.25	3.10	3.98	0.19	3.19	99.16	0.78	1.27	9.00	18.75	2.50	10.20	2.41	0.58	1.69	0.23	1.27	0.25	0.74
HL-010	Granodiorite porphyry	60.72	0.56	18.13	1.41	0.07	3.86	0.81	0.66	9.79	0.31	3.30	99.68	0.07	0.76	7.30	22.20	3.21	16.00	3.70	0.81	2.07	0.27	1.38	0.26	0.82
HL-043	Granodiorite porphyry	64.32	0.37	15.64	4.34	0.06	1.62	1.56	3.34	4.51	0.17	2.40	98.45	0.74	1.12	8.60	18.40	2.10	9.10	2.19	0.57	2.02	0.33	2.03	0.43	1.30
HL-017	Granodiorite	64.55	0.51	17.28	3.38	0.01	0.60	1.41	3.08	5.44	0.26	2.34	98.97	0.57	1.29	6.90	13.35	1.81	8.50	2.23	0.54	2.10	0.34	1.92	0.40	1.13
HL-012	Quartz diorite	61.05	0.50	16.75	6.65	0.06	3.94	1.65	2.12	4.71	0.25	1.78	99.61	0.45	0.97	10.20	25.40	3.11	13.20	3.60	1.06	3.53	0.62	4.15	0.84	2.62
HL-015	Quartz diorite	57.12	0.57	16.46	6.63	0.08	6.98	1.57	1.56	5.17	0.28	3.30	99.84	0.30	0.72	13.40	22.50	3.24	14.80	3.79	1.15	4.48	0.77	4.91	1.04	3.17
HL-016	Quartz diorite	61.66	0.59	17.26	2.03	0.05	4.49	1.95	1.09	6.94	0.29	3.25	99.67	0.16	0.83	7.00	22.20	3.39	16.40	4.54	0.92	4.22	0.76	4.54	0.99	2.93
HL-027	Diorite porphyry	60.13	0.40	17.72	4.85	0.09	2.78	1.94	3.33	6.23	0.16	1.82	99.58	0.53	0.94	5.90	14.60	1.91	7.90	2.06	0.57	1.97	0.33	1.94	0.45	1.32
HL-028	Diorite porphyry	61.40	0.49	17.13	5.40	0.05	1.83	1.80	2.36	6.34	0.21	1.79	98.93	0.37	1.05	7.20	18.20	2.64	11.90	3.37	0.81	3.00	0.51	3.02	0.60	1.82
HL-032	Porphyritic syenite	60.54	0.45	17.69	4.17	0.15	2.26	0.59	5.70	5.84	0.11	1.78	99.39	0.98	0.89	18.80	36.70	3.63	12.70	2.70	0.69	2.68	0.48	3.06	0.71	2.33
HL-004	Porphyritic syenite	75.95	0.13	11.42	0.97	0.02	0.93	0.08	2.97	4.42	0.02	1.16	98.15	0.67	0.94	18.90	39.10	4.18	15.70	2.90	0.32	1.73	0.28	1.85	0.39	1.32
HL-011	Alkali granite porphyry	67.14	0.22	15.85	2.89	0.11	1.01	0.22	5.48	4.69	0.06	1.52	99.23	1.17	1.02	34.90	78.30	8.89	32.40	6.42	0.61	4.40	0.81	5.19	1.08	3.55
HL-014	Alkali granite porphyry	73.57	0.05	14.01	1.61	0.04	0.21	0.08	4.29	5.06	0.01	0.59	99.53	0.85	1.05	21.10	55.10	6.36	23.50	5.82	0.06	4.14	0.76	4.77	1.03	3.18

Appendix Table A1

Sample	Tm	Yb	Lu	∑REE	LR/HR	$(La/Sm)_N$	$(Gd/Yb)_N$	$(La/Yb)_N$	δEu	Y	Sr	Rb	Ba	Th	U	Ta	Nb	Zr	Hf	Ga	Cr	Co	Sc	Ni
HL-002	0.10	0.78	0.15	48.65	8.34	2.41	1.79	8.28	0.88	6.50	268.00	72.60	510.00	1.60	0.50	0.14	2.10	27.80	1.10	17.80	22.00	6.80	9.50	10.60
HL-010	0.12	0.93	0.18	59.25	8.83	1.27	1.84	5.63	0.89	6.20	357.00	11.50	80.00	1.70	1.60	0.24	3.90	94.10	2.60	12.85	5.00	1.70	5.40	5.00
HL-043	0.17	1.24	0.22	48.70	5.29	2.54	1.35	4.97	0.83	11.80	312.00	60.30	660.00	1.50	1.40	0.25	4.00	15.00	0.60	18.40	20.00	13.80	9.10	10.20
HL-017	0.15	1.14	0.20	40.71	4.52	2.00	1.52	4.34	0.76	10.90	365.00	76.50	530.00	2.00	1.70	0.18	2.80	27.10	1.00	14.50	7.00	10.30	9.80	11.50
HL-012	0.38	2.64	0.42	71.77	3.72	1.83	1.11	2.77	0.91	22.50	792.00	59.40	330.00	2.30	1.30	0.27	3.50	47.00	1.50	17.60	4.00	7.40	9.60	4.50
HL-015	0.38	2.60	0.41	76.64	3.32	2.28	1.43	3.70	0.85	33.90	798.00	45.90	160.00	1.70	0.90	0.24	3.60	34.00	1.20	21.70	7.00	14.30	11.10	16.30
HL-016	0.38	2.70	0.39	71.36	3.22	1.00	1.29	1.86	0.64	26.70	436.00	39.70	120.00	1.40	0.70	0.16	2.90	26.20	1.00	17.60	5.00	7.60	15.40	18.70
HL-027	0.18	1.21	0.18	40.52	4.35	1.85	1.35	3.50	0.87	12.20	408.00	49.60	620.00	1.40	0.60	0.31	3.50	14.10	0.60	18.85	24.00	9.10	8.60	9.80
HL-028	0.24	1.73	0.27	55.31	3.94	1.38	1.43	2.99	0.78	15.50	379.00	36.10	700.00	1.30	4.30	0.27	4.20	10.90	0.60	16.25	30.00	19.10	9.40	14.20
HL-032	0.34	2.44	0.40	87.66	6.05	4.50	0.91	5.53	0.78	18.20	470.00	85.10	420.00	13.20	3.80	2.17	39.70	177.00	5.30	24.30	1.00	4.80	1.90	0.70
HL-004	0.19	1.53	0.25	88.64	10.76	4.21	0.94	8.86	0.44	11.90	111.50	46.90	410.00	4.50	1.30	0.50	6.60	128.50	3.90	10.10	14.00	0.60	2.30	1.10
HL-011	0.50	3.76	0.63	181.44	8.11	3.51	0.97	6.66	0.35	27.60	59.40	75.50	220.00	8.80	2.80	2.48	32.20	296.00	7.60	19.95	3.00	0.70	7.70	0.70
HL-014	0.51	3.79	0.59	130.71	5.96	2.34	0.90	3.99	0.04	28.90	53.60	122.00	40.00	10.70	3.10	4.64	56.30	213.00	8.10	21.80	6.00	3.00	1.00	2.90

Appendix Table A2
Sr, Nd and Pb isotopic compositions of intrusive rocks at Halasu porphyry copper belt.

Sample	Lithology	T(Ma)	Rb (ppm)	Sr (ppm)	$^{87}Rb/^{86}Sr$	$^{87}Sr/^{86}Sr$	2σ	I_{Sr}	Sm (ppm)	Nd (ppm)	$^{147}Sm/^{144}Nd$	$^{143}Nd/^{144}Nd$	2σ
HL-011	Alkali granite porphyry	327	75.5	59.4	3.71683	0.724470	16	0.707172	6.4	32.4	0.12069	0.512754	10
HL-012	Quartz diorite	379	59.4	792.0	0.21932	0.705526	14	0.704342	3.6	13.2	0.16611	0.512832	8
HL-016	Quartz diorite	379	39.7	436.0	0.26627	0.705860	16	0.704438	4.5	16.4	0.16861	0.512853	8
HL-017	Granodiorite	378	76.5	365.0	0.61289	0.707225	16	0.703935	2.2	8.5	0.15979	0.512826	10
HL-028	Diorite porphyry	372	36.1	379.0	0.27854	0.705739	14	0.704264	3.4	11.9	0.17249	0.512818	10

Appendix Table A2 (*continued*)

Sample	εNd(t)	T_{DM2}(Ma)	$f_{Sm/Nd}$	$^{206}Pb/^{204}Pb$	$^{207}Pb/^{204}Pb$	$^{208}Pb/^{204}Pb$	Pb (ppm)	Th (ppm)	U (ppm)	$(^{206}Pb/^{204}Pb)_t$	$(^{207}Pb/^{204}Pb)_t$	$(^{208}Pb/^{204}Pb)_t$
HL-011	5.4	640	−0.39	19.527	15.548	38.741	7.5	8.8	2.8	18.085	15.471	37.309
HL-012	5.3	699	−0.16	18.484	15.497	37.961	8.4	2.3	1.3	17.805	15.461	37.583
HL-016	5.6	675	−0.14	19.562	15.553	38.482	2.4	1.4	0.7	18.269	15.483	37.667
HL-017	5.5	683	−0.19	19.590	15.555	38.176	4.1	2.0	1.7	17.747	15.455	37.494
HL-028	4.7	741	−0.12	18.501	15.493	37.798	6.4	1.3	4.3	15.617	15.337	37.524

Appendix Table A3
LA–ICP-MS U–Pb isotopic analyses for zircon grains from the intrusive rocks at Halasu porphyry copper belt.

Analysis	Content (ppm)			Th/U	Isotopic ratios						Isotopic ages (Ma)					
	Pb	Th	U		$^{207}Pb/^{206}Pb$	±1σ	$^{207}Pb/^{235}U$	±1σ	$^{206}Pb/^{238}U$	±1σ	$^{207}Pb/^{206}Pb$	±1σ	$^{207}Pb/^{235}U$	±1σ	$^{206}Pb/^{238}U$	±1σ
HL-032 porphyritic syenite																
1	108	2717	818	3.32	0.0550	0.0018	0.4722	0.0144	0.0624	0.0006	413	72	393	10	390	4
2	245	1345	3293	0.41	0.0547	0.0013	0.4724	0.0118	0.0624	0.0007	467	54	393	8	390	4
3	170	2705	1733	1.56	0.0543	0.0015	0.4729	0.0133	0.0629	0.0008	383	63	393	9	393	5
4	80	416	1049	0.40	0.0544	0.0016	0.4686	0.0137	0.0623	0.0006	387	65	390	9	390	4
5	230	1958	2803	0.70	0.0516	0.0017	0.4536	0.0146	0.0634	0.0010	333	74	380	10	396	6
6	146	2968	1348	2.20	0.0517	0.0015	0.4387	0.0128	0.0614	0.0006	272	64	369	9	384	4
7	80	440	1081	0.41	0.0512	0.0016	0.4332	0.0132	0.0613	0.0007	256	74	365	9	384	4
8	45	791	446	1.78	0.0518	0.0021	0.4370	0.0178	0.0611	0.0007	276	90	368	13	382	4
9	58	771	632	1.22	0.0543	0.0019	0.4667	0.0164	0.0623	0.0007	389	80	389	11	389	4
10	141	593	1914	0.31	0.0551	0.0018	0.4784	0.0153	0.0627	0.0007	417	70	397	11	392	4
11	194	6503	1231	5.28	0.0642	0.0024	0.5631	0.0196	0.0637	0.0007	750	81	454	13	398	5
12	210	1418	2671	0.53	0.0562	0.0020	0.4872	0.0169	0.0624	0.0007	461	78	403	12	390	4
13	50	680	532	1.28	0.0569	0.0023	0.4976	0.0202	0.0630	0.0008	487	89	410	14	394	5
14	82	1266	863	1.47	0.0569	0.0021	0.4872	0.0181	0.0615	0.0007	500	81	403	12	384	4
15	99	1329	1026	1.29	0.0550	0.0019	0.4878	0.0165	0.0639	0.0007	413	71	403	11	399	4
16	87	1107	956	1.16	0.0558	0.0020	0.4945	0.0182	0.0636	0.0008	456	78	408	12	398	5
17	115	2458	1037	2.37	0.0547	0.0018	0.4833	0.0171	0.0635	0.0008	398	74	400	12	397	5
18	85	907	1012	0.90	0.0546	0.0016	0.4694	0.0144	0.0620	0.0007	394	67	391	10	388	4
19	274	2965	3169	0.94	0.0568	0.0014	0.5064	0.0139	0.0640	0.0007	483	56	416	9	400	4
20	104	1376	1121	1.23	0.0570	0.0017	0.5009	0.0153	0.0634	0.0008	500	60	412	10	396	5
21	103	534	1355	0.39	0.0551	0.0016	0.4793	0.0137	0.0627	0.0006	417	63	398	9	392	4
22	49	616	557	1.11	0.0566	0.0020	0.4792	0.0157	0.0612	0.0007	476	78	398	11	383	4
23	114	1226	1323	0.93	0.0542	0.0016	0.4667	0.0140	0.0622	0.0007	376	67	389	10	389	4
HL-004 porphyritic syenite																
1	27	199	341	0.58	0.0566	0.0026	0.4948	0.0215	0.0621	0.0008	476	102	408	15	389	5
2	29	219	348	0.63	0.0528	0.0021	0.4576	0.0173	0.0626	0.0008	320	88	383	12	391	5
3	19	160	238	0.67	0.0568	0.0024	0.5009	0.0214	0.0621	0.0008	483	93	412	14	388	5
4	6	41	73	0.56	0.0561	0.0035	0.4657	0.0253	0.0619	0.0011	457	132	388	18	387	7
5	36	377	443	0.85	0.0595	0.0022	0.5097	0.0213	0.0612	0.0007	583	81	418	14	383	4
6	27	216	328	0.66	0.0530	0.0018	0.4609	0.0150	0.0627	0.0007	328	108	385	10	392	4
7	15	77	194	0.40	0.0586	0.0025	0.5192	0.0221	0.0637	0.0008	550	93	425	15	398	5
8	17	114	222	0.51	0.0555	0.0023	0.4796	0.0182	0.0618	0.0007	432	88	398	12	387	4
9	41	552	446	1.24	0.0543	0.0019	0.4700	0.0166	0.0620	0.0007	383	80	391	11	388	4
10	25	193	305	0.63	0.0563	0.0021	0.4837	0.0175	0.0624	0.0007	465	81	401	12	390	4
11	23	164	275	0.60	0.0558	0.0024	0.4860	0.0198	0.0632	0.0007	443	127	402	14	395	4
12	35	294	441	0.67	0.0564	0.0023	0.4824	0.0181	0.0609	0.0008	478	95	400	12	381	5
13	24	179	300	0.60	0.0589	0.0024	0.5138	0.0211	0.0629	0.0008	561	86	421	14	393	5
14	18	103	212	0.49	0.0742	0.0030	0.6370	0.0243	0.0630	0.0008	1056	80	500	15	394	5
15	25	162	327	0.50	0.0537	0.0020	0.4620	0.0163	0.0622	0.0007	367	85	386	11	389	4
16	22	157	262	0.60	0.0610	0.0026	0.5212	0.0222	0.0619	0.0008	639	93	426	15	387	5
17	27	223	331	0.67	0.0681	0.0029	0.5938	0.0251	0.0634	0.0009	872	83	473	16	396	5
18	11	60	143	0.42	0.0530	0.0028	0.4555	0.0235	0.0620	0.0010	328	122	381	16	388	6
19	33	282	406	0.69	0.0545	0.0024	0.4794	0.0188	0.0620	0.0007	394	94	398	13	388	4
20	23	149	290	0.51	0.0553	0.0026	0.4836	0.0196	0.0630	0.0009	433	104	401	13	394	6
21	19	132	246	0.53	0.0586	0.0025	0.5110	0.0195	0.0625	0.0008	554	93	419	13	391	5
22	25	206	306	0.67	0.0535	0.0021	0.4618	0.0169	0.0621	0.0008	350	87	386	12	389	5
23	23	178	270	0.66	0.0644	0.0024	0.5618	0.0187	0.0629	0.0007	767	78	453	12	393	4
HL-012 quartz diorite																
1	6	41	85	0.48	0.0498	0.0037	0.3997	0.0267	0.0603	0.0011	187	−25	341	19	377	7
2	6	46	85	0.54	0.0515	0.0035	0.4214	0.0261	0.0606	0.0009	261	154	357	19	379	6
3	13	127	161	0.79	0.0489	0.0027	0.4128	0.0225	0.0601	0.0008	143	128	351	16	376	5
4	7	38	90	0.43	0.0487	0.0034	0.4073	0.0262	0.0612	0.0011	132	156	347	19	383	7
5	17	171	215	0.80	0.0499	0.0024	0.4227	0.0200	0.0607	0.0008	191	115	358	14	380	5
6	14	95	185	0.51	0.0501	0.0025	0.4127	0.0194	0.0593	0.0007	198	115	351	14	372	4
7	11	90	139	0.65	0.0521	0.0030	0.4260	0.0225	0.0592	0.0009	300	125	360	16	371	5
8	9	70	120	0.58	0.0527	0.0028	0.4359	0.0219	0.0598	0.0009	322	119	367	15	374	5

9	19	170	240	0.71	0.0522	0.0023	0.4315	0.0188	0.0596	0.0007	300	102	364	13	373	4
10	9	63	121	0.52	0.0556	0.0032	0.4582	0.0254	0.0597	0.0009	439	128	383	18	374	6
11	7	56	92	0.60	0.0557	0.0035	0.4551	0.0261	0.0597	0.0009	439	139	381	18	374	5
12	5	38	71	0.53	0.0604	0.0048	0.5011	0.0377	0.0598	0.0011	617	175	412	26	375	7
13	6	42	87	0.48	0.0536	0.0038	0.4405	0.0291	0.0606	0.0010	354	161	371	20	379	6
14	9	63	117	0.53	0.0496	0.0029	0.4137	0.0232	0.0608	0.0009	176	137	352	17	380	6
15	7	35	95	0.37	0.0573	0.0038	0.4721	0.0282	0.0617	0.0011	502	148	393	19	386	6
16	7	44	87	0.50	0.0607	0.0043	0.4993	0.0344	0.0603	0.0010	628	147	411	23	377	6
17	6	38	75	0.51	0.0530	0.0037	0.4491	0.0307	0.0618	0.0010	332	157	377	22	387	6
18	9	61	125	0.49	0.0545	0.0028	0.4598	0.0240	0.0613	0.0009	394	117	384	17	383	6
19	6	37	80	0.46	0.0527	0.0036	0.4474	0.0284	0.0628	0.0011	317	149	375	20	393	6
20	9	63	116	0.55	0.0549	0.0029	0.4623	0.0231	0.0623	0.0010	409	119	386	16	389	6
21	6	39	83	0.47	0.0531	0.0030	0.4549	0.0253	0.0627	0.0009	345	131	381	18	392	6
22	8	57	109	0.52	0.0537	0.0028	0.4463	0.0228	0.0607	0.0009	367	120	375	16	380	5
HL-013 quartz diorite																
1	3	16	46	0.35	0.0569	0.0058	0.4401	0.0372	0.0596	0.0015	487	221	370	26	373	9
2	8	46	115	0.40	0.0584	0.0030	0.4709	0.0225	0.0602	0.0009	546	111	392	16	377	6
3	4	21	55	0.38	0.0502	0.0041	0.3961	0.0281	0.0594	0.0010	206	189	339	20	372	6
4	12	107	161	0.66	0.0517	0.0025	0.4257	0.0205	0.0593	0.0007	272	111	360	15	372	4
5	5	37	68	0.55	0.0483	0.0033	0.4088	0.0269	0.0616	0.0010	122	143	348	19	385	6
6	8	49	110	0.45	0.0546	0.0033	0.4646	0.0283	0.0609	0.0009	394	135	387	20	381	5
7	5	23	73	0.31	0.0599	0.0044	0.5030	0.0350	0.0613	0.0011	598	159	414	24	383	7
8	11	71	151	0.47	0.0573	0.0035	0.4762	0.0272	0.0602	0.0009	506	133	395	19	377	6
9	5	28	74	0.38	0.0548	0.0043	0.4477	0.0326	0.0599	0.0011	467	178	376	23	375	6
10	5	21	64	0.33	0.0600	0.0044	0.5000	0.0351	0.0602	0.0011	611	159	412	24	377	6
11	11	92	158	0.58	0.0553	0.0027	0.4603	0.0223	0.0606	0.0008	433	105	384	15	379	5
12	5	21	68	0.31	0.0528	0.0042	0.4352	0.0330	0.0606	0.0011	320	186	367	23	379	7
13	5	41	72	0.58	0.0575	0.0043	0.4780	0.0320	0.0596	0.0010	522	197	397	22	373	6
14	9	58	123	0.47	0.0543	0.0031	0.4528	0.0256	0.0603	0.0008	387	130	379	18	378	5
15	7	37	98	0.37	0.0526	0.0030	0.4311	0.0234	0.0596	0.0010	322	125	364	17	373	6
16	10	74	133	0.55	0.0553	0.0028	0.4510	0.0224	0.0596	0.0009	433	145	378	16	373	5
17	26	400	294	1.36	0.0541	0.0023	0.4563	0.0192	0.0610	0.0007	376	93	382	13	382	4
18	7	52	109	0.47	0.0544	0.0038	0.4447	0.0304	0.0594	0.0009	387	153	374	21	372	6
19	4	23	60	0.38	0.0605	0.0053	0.4829	0.0392	0.0605	0.0013	633	383	400	27	379	8
20	6	32	80	0.41	0.0585	0.0040	0.4872	0.0323	0.0615	0.0011	550	152	403	22	385	7
21	8	64	114	0.57	0.0595	0.0043	0.4896	0.0333	0.0611	0.0011	583	156	405	23	382	7
22	6	34	84	0.40	0.0596	0.0041	0.4989	0.0305	0.0630	0.0009	591	148	411	21	394	6
23	6	46	88	0.52	0.0578	0.0034	0.4698	0.0265	0.0605	0.0010	524	134	391	18	379	6
HL-017 granodiorite																
1	15	164	188	0.87	0.0490	0.0027	0.4031	0.0217	0.0581	0.0009	146	130	344	16	364	5
2	6	37	77	0.48	0.0533	0.0040	0.4428	0.0302	0.0596	0.0011	339	170	372	21	373	6
3	19	231	217	1.06	0.0491	0.0024	0.4149	0.0200	0.0597	0.0008	154	117	352	14	373	5
4	5	22	68	0.32	0.0478	0.0042	0.3960	0.0322	0.0595	0.0011	87	196	339	23	373	7
5	5	34	61	0.56	0.0523	0.0044	0.4204	0.0321	0.0602	0.0013	298	192	356	23	377	8
6	14	132	176	0.75	0.0548	0.0029	0.4440	0.0224	0.0590	0.0008	406	119	373	16	369	5
7	9	65	119	0.54	0.0499	0.0030	0.4167	0.0223	0.0611	0.0009	191	134	354	16	382	6
8	5	35	62	0.56	0.0528	0.0040	0.4317	0.0286	0.0597	0.0012	317	142	364	20	374	7
9	3	17	47	0.36	0.0545	0.0048	0.4530	0.0345	0.0621	0.0013	391	193	379	24	388	8
10	5	26	72	0.36	0.0554	0.0045	0.4542	0.0327	0.0592	0.0011	428	181	380	23	371	7
11	10	87	127	0.69	0.0601	0.0036	0.4923	0.0269	0.0593	0.0009	606	127	406	18	372	5
12	18	175	229	0.77	0.0482	0.0026	0.4135	0.0200	0.0621	0.0008	109	122	351	14	388	5
13	7	43	91	0.48	0.0539	0.0041	0.4534	0.0299	0.0623	0.0011	369	170	380	21	389	6
14	4	18	53	0.34	0.0550	0.0052	0.4642	0.0394	0.0622	0.0015	409	210	387	27	389	9
15	5	27	72	0.37	0.0594	0.0043	0.4727	0.0284	0.0591	0.0012	583	164	393	20	370	7
16	7	59	96	0.61	0.0522	0.0043	0.4360	0.0317	0.0622	0.0011	295	187	367	22	389	6
17	6	37	78	0.47	0.0565	0.0046	0.4579	0.0338	0.0606	0.0012	472	180	383	24	379	7
18	4	22	58	0.37	0.0541	0.0048	0.4296	0.0315	0.0601	0.0013	372	200	363	22	376	8
19	6	41	85	0.48	0.0626	0.0048	0.5248	0.0372	0.0630	0.0012	694	167	428	25	394	7
20	7	42	100	0.43	0.0553	0.0040	0.4571	0.0306	0.0608	0.0012	433	168	382	21	380	7
21	5	29	71	0.41	0.0641	0.0049	0.5146	0.0355	0.0629	0.0015	744	163	422	24	394	9
22	4	22	55	0.39	0.0559	0.0051	0.4541	0.0368	0.0603	0.0012	456	204	380	26	378	7

(continued on next page)

Appendix Table A3 (*continued*)

Analysis	Content (ppm)			Th/U	Isotopic ratios						Isotopic ages (Ma)					
	Pb	Th	U		$^{207}Pb/^{206}Pb$	±1σ	$^{207}Pb/^{235}U$	±1σ	$^{206}Pb/^{238}U$	±1σ	$^{207}Pb/^{206}Pb$	±1σ	$^{207}Pb/^{235}U$	±1σ	$^{206}Pb/^{238}U$	±1σ
HL-037 granodiorite porphyry																
1	5	29	70	0.41	0.0550	0.0046	0.4434	0.0345	0.0584	0.0011	413	189	373	24	366	7
2	6	46	84	0.54	0.0572	0.0045	0.4829	0.0355	0.0617	0.0012	498	171	400	24	386	7
3	5	39	71	0.55	0.0550	0.0042	0.4550	0.0321	0.0603	0.0012	413	170	381	22	377	7
4	5	30	71	0.42	0.0526	0.0036	0.4441	0.0310	0.0603	0.0012	322	157	373	22	377	7
5	5	33	73	0.45	0.0531	0.0041	0.4393	0.0310	0.0604	0.0011	345	178	370	22	378	7
6	7	45	86	0.53	0.0481	0.0033	0.4114	0.0258	0.0612	0.0010	102	156	350	19	383	6
7	5	31	73	0.42	0.0555	0.0043	0.4372	0.0292	0.0588	0.0011	432	171	368	21	368	7
8	6	36	83	0.43	0.0551	0.0036	0.4576	0.0299	0.0600	0.0011	417	151	383	21	376	7
9	7	42	89	0.48	0.0547	0.0035	0.4506	0.0266	0.0601	0.0010	398	175	378	19	376	6
10	7	56	84	0.67	0.0569	0.0035	0.4786	0.0274	0.0623	0.0012	487	135	397	19	389	7
11	5	28	69	0.41	0.0559	0.0037	0.4613	0.0293	0.0601	0.0012	450	146	385	20	376	7
12	5	34	71	0.48	0.0498	0.0035	0.4178	0.0269	0.0618	0.0012	183	163	354	19	387	7
13	5	30	73	0.41	0.0589	0.0042	0.4759	0.0316	0.0601	0.0011	565	128	395	22	376	7
14	5	29	66	0.44	0.0559	0.0040	0.4567	0.0309	0.0604	0.0012	450	164	382	22	378	7
15	5	27	65	0.42	0.0533	0.0038	0.4334	0.0272	0.0609	0.0011	339	163	366	19	381	7
16	15	153	201	0.76	0.0481	0.0027	0.3986	0.0212	0.0601	0.0009	106	130	341	15	376	6
17	4	27	62	0.43	0.0548	0.0049	0.4477	0.0394	0.0598	0.0011	406	202	376	28	374	7
18	8	56	100	0.55	0.0541	0.0032	0.4428	0.0250	0.0596	0.0009	376	133	372	18	373	6
19	9	95	111	0.86	0.0571	0.0030	0.4721	0.0240	0.0597	0.0009	494	117	393	17	374	6
20	5	31	69	0.45	0.0515	0.0039	0.4354	0.0310	0.0623	0.0011	261	174	367	22	389	7
21	5	36	75	0.48	0.0553	0.0039	0.4386	0.0273	0.0587	0.0011	433	156	369	19	368	7
HL-027 quartz diorite																
1	8	63	106	0.59	0.06184	0.00432	0.4828	0.03134	0.06039	0.00102	733	145	400	21	378	6
2	8	57	100	0.58	0.05411	0.00392	0.46064	0.02844	0.0613	0.00108	376	160	385	20	384	7
3	6	46	82	0.56	0.05916	0.0044	0.46305	0.02832	0.05793	0.00112	572	131	386	20	363	7
4	7	56	92	0.61	0.05108	0.00391	0.41967	0.0291	0.06	0.00114	243	178	356	21	376	7
5	9	68	114	0.60	0.05212	0.00369	0.43095	0.02745	0.06099	0.00104	300	168	364	19	382	6
6	6	36	77	0.47	0.0552	0.00404	0.4399	0.02951	0.06044	0.00107	420	160	370	21	378	7
7	6	37	82	0.45	0.0557	0.00431	0.46634	0.03156	0.06153	0.00123	439	174	389	22	385	7
8	5	35	70	0.49	0.05245	0.00472	0.43033	0.03448	0.05983	0.00112	306	206	363	24	375	7
9	6	45	68	0.67	0.05452	0.00459	0.4585	0.03786	0.0605	0.00129	391	191	383	26	379	8
10	9	78	125	0.62	0.0608	0.00305	0.46803	0.02251	0.05762	0.00087	632	108	390	16	361	5
11	6	42	83	0.50	0.0552	0.00388	0.44611	0.03256	0.05887	0.00118	420	157	375	23	369	7
12	6	48	85	0.56	0.06287	0.0047	0.51342	0.03766	0.06165	0.00125	706	128	421	25	386	8
13	12	134	146	0.91	0.05219	0.00315	0.42036	0.02307	0.05984	0.00088	295	142	356	16	375	5
14	8	62	101	0.61	0.05241	0.00367	0.43404	0.02738	0.06062	0.00104	302	129	366	19	379	6
15	7	45	86	0.52	0.05946	0.00382	0.51051	0.0304	0.06076	0.00113	583	139	419	20	380	7
16	6	42	82	0.51	0.05424	0.00445	0.44857	0.03461	0.06101	0.00127	389	190	376	24	382	8
17	7	59	99	0.60	0.05904	0.00446	0.46311	0.03062	0.05849	0.00106	569	165	386	21	366	6
18	5	38	71	0.53	0.05986	0.00499	0.47448	0.03438	0.05843	0.00119	598	181	394	24	366	7
19	6	56	80	0.71	0.0617	0.0045	0.5001	0.03532	0.06023	0.00106	665	157	412	24	377	6
20	6	42	88	0.47	0.05794	0.00398	0.45062	0.02826	0.05731	0.00099	528	152	378	20	359	6
21	8	69	110	0.63	0.05638	0.00388	0.45426	0.02834	0.05928	0.00109	478	154	380	20	371	7
22	7	50	95	0.52	0.05547	0.00418	0.45898	0.03276	0.05947	0.00112	432	169	384	23	372	7
23	6	41	84	0.49	0.05406	0.0041	0.45078	0.03068	0.06017	0.00109	372	203	378	21	377	7

HL-028 quartz diorite																
1	11	93	138	0.68	0.04896	0.00326	0.40895	0.02599	0.05811	0.00086	146	148	348	19	364	5
2	5	29	64	0.46	0.05737	0.00489	0.46711	0.03527	0.05955	0.00122	506	189	389	24	373	7
3	6	42	74	0.57	0.04966	0.00436	0.40533	0.03623	0.05991	0.00124	189	183	346	26	375	8
4	9	75	111	0.68	0.05629	0.00367	0.47996	0.03036	0.06118	0.00112	465	144	398	21	383	7
5	6	37	83	0.44	0.05743	0.00501	0.45748	0.0353	0.05878	0.00106	509	197	383	25	368	6
6	4	21	53	0.39	0.05934	0.0052	0.50332	0.04295	0.06112	0.00167	589	193	414	29	382	10
7	6	38	80	0.48	0.05908	0.00439	0.47496	0.0322	0.05951	0.00112	569	163	395	22	373	7
8	7	57	99	0.58	0.05342	0.00414	0.42017	0.02769	0.0585	0.00116	346	181	356	20	366	7
9	6	35	79	0.44	0.05458	0.00415	0.43747	0.03127	0.05922	0.00124	394	177	368	22	371	8
10	7	45	95	0.48	0.05495	0.00382	0.45507	0.03004	0.06102	0.0011	409	156	381	21	382	7
11	26	460	272	1.69	0.05586	0.00283	0.43478	0.02033	0.05791	0.0008	456	111	367	14	363	5
12	18	173	225	0.77	0.06071	0.00298	0.4848	0.02273	0.05941	0.00082	628	106	401	16	372	5
13	5	37	70	0.53	0.05777	0.00496	0.46223	0.034	0.05832	0.00126	520	189	386	24	365	8
14	4	23	65	0.35	0.05437	0.00469	0.42742	0.03216	0.05863	0.00117	387	190	361	23	367	7
15	6	35	79	0.45	0.05435	0.00448	0.44877	0.03355	0.06061	0.00119	387	187	376	24	379	7
16	8	60	98	0.61	0.05846	0.00438	0.48577	0.03255	0.06194	0.00113	546	163	402	22	387	7
17	7	48	89	0.54	0.0511	0.00413	0.40733	0.02846	0.05912	0.0011	256	182	347	21	370	7
18	5	30	73	0.42	0.05414	0.00438	0.43728	0.03098	0.06209	0.00126	376	183	368	22	388	8
19	6	48	83	0.58	0.05135	0.00421	0.43201	0.03238	0.05962	0.00117	257	189	365	23	373	7
20	5	29	72	0.40	0.05289	0.00445	0.43375	0.03098	0.06	0.00112	324	193	366	22	376	7
21	8	66	110	0.60	0.05106	0.00342	0.40769	0.02618	0.05769	0.00099	243	156	347	19	362	6
22	8	66	105	0.63	0.05602	0.00353	0.46177	0.02736	0.06019	0.00101	454	141	385	19	377	6
23	6	42	79	0.54	0.05061	0.00407	0.40888	0.02628	0.05934	0.0012	233	182	348	19	372	7
HL-011 alkali granite porphyry																
1	10	64	160	0.40	0.05458	0.00298	0.37917	0.01983	0.05093	0.00076	394	94	326	15	320	5
2	18	106	289	0.37	0.05484	0.00255	0.39117	0.01821	0.05129	0.00072	406	104	335	13	322	4
3	13	77	202	0.38	0.06561	0.00383	0.47187	0.02764	0.05132	0.00082	794	128	392	19	323	5
4	20	98	340	0.29	0.05277	0.00216	0.37826	0.01488	0.05133	0.00065	320	88	326	11	323	4
5	10	64	168	0.38	0.05416	0.00311	0.38471	0.02019	0.05156	0.00077	376	130	330	15	324	5
6	39	374	567	0.66	0.05319	0.00201	0.37635	0.01318	0.0518	0.00057	345	82	324	10	326	3
7	12	63	189	0.33	0.06035	0.00364	0.43028	0.02681	0.05183	0.0009	617	131	363	19	326	5
8	12	72	199	0.36	0.04759	0.00259	0.33791	0.01655	0.05189	0.0007	80	131	296	13	326	4
9	37	215	598	0.36	0.05244	0.0018	0.37628	0.01305	0.05191	0.00063	306	78	324	10	326	4
10	14	83	220	0.38	0.0551	0.00293	0.39621	0.02008	0.05192	0.00084	417	116	339	15	326	5
11	11	65	178	0.37	0.05706	0.00363	0.41992	0.02658	0.05211	0.00085	494	141	356	19	327	5
12	14	105	214	0.49	0.05164	0.00237	0.37389	0.01638	0.05232	0.00073	333	106	323	12	329	4
13	6	34	97	0.35	0.05249	0.00375	0.37377	0.02407	0.05234	0.00092	306	131	322	18	329	6
14	8	34	133	0.26	0.05101	0.00347	0.38077	0.02518	0.05235	0.00091	243	157	328	19	329	6
15	10	60	156	0.39	0.05248	0.00287	0.37834	0.01933	0.05237	0.00077	306	126	326	14	329	5
16	10	51	169	0.30	0.06155	0.00372	0.45965	0.0289	0.05261	0.00088	657	130	384	20	331	5
17	13	94	219	0.43	0.0541	0.00242	0.40247	0.01761	0.05308	0.00093	376	100	343	13	333	6
18	50	273	805	0.34	0.05598	0.00236	0.42312	0.01668	0.05422	0.00068	450	94	358	12	340	4

Appendix Table A4
Zircon Lu–Hf isotopic data for intrusive rocks at Halasu porphyry copper belt.

	T(Ma)	$^{176}Yb/^{177}Hf$	σ	$^{176}Lu/^{177}Hf$	σ	$^{176}Hf/^{177}Hf$	σ	εHf(t)	T_{DM2}(Ma)
HL-032 porphyritic syenite									
1	411	0.066876	0.000607	0.002027	0.000014	0.282781	0.000010	8.80	840
2	396.4	0.069499	0.000225	0.002959	0.000002	0.282808	0.000009	9.22	802
3	383.6	0.026552	0.000044	0.000927	0.000004	0.282783	0.000011	8.60	832
4	389.3	0.083389	0.000147	0.003367	0.000009	0.282718	0.000010	5.80	1015
5	391.9	0.030694	0.000125	0.001014	0.000003	0.282812	0.000011	9.78	763
6	394.1	0.063551	0.000465	0.002067	0.000007	0.282789	0.000011	8.75	830
7	399.5	0.034173	0.000369	0.001138	0.000011	0.282825	0.000011	10.36	731
8	387.6	0.042314	0.000188	0.001607	0.000004	0.282794	0.000011	8.89	816
9	400.1	0.038110	0.000173	0.001035	0.000003	0.282859	0.000010	11.62	651
10	396.4	0.104460	0.001106	0.003096	0.000027	0.282790	0.000011	8.55	844
11	392	0.062626	0.000229	0.001818	0.000002	0.282799	0.000011	9.13	804
HL-012 quartz diorite									
1	377.3	0.033303	0.000108	0.001385	0.000005	0.282864	0.000013	11.22	659
2	375	0.033684	0.000271	0.001474	0.000013	0.282829	0.000013	9.84	744
3	379	0.059253	0.000136	0.002403	0.000005	0.282865	0.000013	11.00	674
4	383	0.063424	0.000538	0.002687	0.000025	0.282856	0.000014	10.82	693
5	372	0.073579	0.000248	0.003075	0.000011	0.282920	0.000013	12.66	563
6	380.4	0.051844	0.000658	0.002081	0.000020	0.282861	0.000013	10.99	676
7	386	0.072748	0.000141	0.003055	0.000003	0.282835	0.000013	9.89	748
8	377.3	0.038084	0.000156	0.001671	0.000009	0.282888	0.000014	12.00	610
9	384.6	0.050497	0.000284	0.002043	0.000011	0.282858	0.000013	10.99	679
10	383	0.055487	0.000165	0.002276	0.000006	0.282875	0.000014	11.37	649
11	393.7	0.086526	0.003037	0.003402	0.000112	0.282859	0.000013	10.86	695
12	379.9	0.077080	0.000958	0.003029	0.000029	0.282797	0.000012	8.49	836
13	391.9	0.052731	0.000881	0.002243	0.000038	0.282887	0.000013	12.13	612
HL-037 granodiorite porphyry									
1	365.8	0.034697	0.000391	0.001480	0.000010	0.282865	0.000013	10.99	665
2	377.5	0.030369	0.000351	0.001397	0.000016	0.282861	0.000012	11.12	666
3	377.4	0.033270	0.000476	0.001491	0.000022	0.282835	0.000012	10.17	726
4	378	0.028515	0.000158	0.001273	0.000007	0.282873	0.000013	11.57	637
5	383	0.027300	0.000522	0.001149	0.000022	0.282883	0.000011	12.13	607
6	367.9	0.046581	0.001845	0.001881	0.000070	0.282863	0.000013	10.86	675
7	376.2	0.024789	0.000098	0.001165	0.000007	0.282915	0.000012	13.04	542

8	376	0.028723	0.000165	0.001291	0.000010	0.282887	0.000012	12.25	601
9	376	0.020394	0.000261	0.000948	0.000011	0.282864	0.000012	11.47	649
10	374.6	0.030981	0.000170	0.001452	0.000007	0.282878	0.000014	11.63	631
HL-028 diorite porphyry									
1	383	0.030282	0.000704	0.001291	0.000030	0.282888	0.000013	12.27	599
2	372.9	0.028779	0.000069	0.001341	0.000005	0.282868	0.000011	11.28	652
3	368	0.037007	0.000273	0.001669	0.000012	0.282835	0.000014	9.83	737
4	372.3	0.022941	0.000118	0.001066	0.000005	0.282838	0.000012	10.15	719
5	371	0.029498	0.000249	0.001403	0.000010	0.282882	0.000012	11.67	624
6	382	0.031836	0.000300	0.001453	0.000014	0.282854	0.000013	11.00	679
7	372	0.034499	0.000790	0.001448	0.000033	0.282891	0.000010	11.96	605
8	379	0.036219	0.000191	0.001648	0.000011	0.282873	0.000010	11.46	644
9	380	0.032610	0.000226	0.001487	0.000009	0.282873	0.000009	11.62	638
10	373.3	0.025793	0.000344	0.001180	0.000013	0.282905	0.000010	12.62	566
HL-017 granodiorite									
1	372.5	0.083859	0.000463	0.003420	0.000004	0.282848	0.000012	10.05	730
2	382.7	0.074361	0.000543	0.002934	0.000014	0.282898	0.000011	12.13	605
3	385.3	0.039989	0.000352	0.001713	0.000017	0.282868	0.000011	11.43	652
4	379.4	0.040532	0.000392	0.001734	0.000019	0.282858	0.000009	10.98	676
5	390.6	0.028201	0.000399	0.001182	0.000015	0.282898	0.000010	12.76	571
6	374.6	0.062250	0.000669	0.002590	0.000029	0.282814	0.000011	9.10	793
7	381.3	0.034413	0.000188	0.001472	0.000004	0.282880	0.000011	11.84	623
8	381.7	0.081795	0.000639	0.003179	0.000016	0.282844	0.000011	10.15	731
9	379.6	0.046167	0.000159	0.001986	0.000004	0.282873	0.000010	11.43	648
10	384.9	0.041254	0.000354	0.001680	0.000012	0.282851	0.000011	10.84	689
11	371	0.047518	0.000208	0.001940	0.000006	0.282871	0.000009	11.18	657
HL-011 alkali granite porphyry									
1	326.2	0.044256	0.000354	0.001670	0.000008	0.282863	0.000010	10.10	694
2	328.9	0.021381	0.000101	0.000840	0.000001	0.282894	0.000011	11.30	615
3	322.7	0.069735	0.000699	0.002669	0.000030	0.282802	0.000010	7.58	850
4	324.1	0.028229	0.000283	0.001117	0.000012	0.282857	0.000011	9.91	702
5	328.8	0.051969	0.000176	0.002013	0.000008	0.282809	0.000014	8.09	822
6	326.1	0.036631	0.000136	0.001431	0.000004	0.282891	0.000009	11.08	629
7	325	0.029922	0.000448	0.001221	0.000019	0.282835	0.000011	9.13	752
8	325	0.055369	0.000132	0.002065	0.000001	0.282874	0.000009	10.33	676
9	326	0.047277	0.000462	0.001803	0.000019	0.282853	0.000013	9.65	720
10	326.3	0.058623	0.000125	0.002421	0.000005	0.282845	0.000012	9.25	746
11	326.	0.025920	0.000071	0.001068	0.000003	0.282879	0.000011	10.72	652

Appendix Table A5
Zircon trace elements at Halasu porphyry copper belt.

	La	Ce	Pr	Nd	Sm	Eu	Gd	Tb	Dy	Ho	Er	Tm	Yb	Lu	Ce^{4+}/Ce^{3+}	Ce/Ce*	Eu/Eu*	log(fO_2)	ΔFMQ	T °C
HL-032 porphyritic syenite																				
1	1.063	54.484	1.003	6.452	6.105	1.786	20.114	7.730	103.736	48.787	277.432	71.924	690.989	110.983	71.72	12.94	0.49	−19.25	−2.90	730
2	1.138	82.212	1.219	7.411	5.710	1.791	18.214	6.703	93.345	43.543	246.053	66.822	701.596	119.579	136.29	17.12	0.54	−16.41	−0.91	766
3	3.355	96.342	3.351	22.121	15.920	6.013	49.350	16.663	218.850	90.413	451.595	102.540	872.166	120.752	19.11	7.05	0.66	−24.03	−6.49	684
4	1.537	54.853	1.370	9.321	5.976	1.902	14.787	5.249	71.594	34.301	202.086	54.481	531.633	79.555	55.66	9.27	0.62	−19.50	−3.63	750
5	1.173	22.916	1.165	7.154	4.743	1.579	10.287	2.929	34.091	15.396	90.565	24.667	242.389	37.704	17.63	4.81	0.69	−26.71	−8.57	663
6	4.272	70.134	3.544	20.981	13.078	3.997	26.755	7.142	81.181	35.243	209.889	63.497	774.106	155.012	31.41	4.42	0.65	−22.73	−6.65	741
7	1.258	68.263	1.013	7.130	5.537	1.838	19.213	6.830	97.395	44.269	250.925	65.304	632.767	97.324	95.41	14.83	0.54	−17.44	−1.71	756
8	0.226	30.853	0.273	3.202	3.168	1.383	15.422	5.852	82.994	40.056	231.652	59.107	582.650	101.529	134.75	30.42	0.61	−16.01	0.33	731
9	4.301	42.978	1.431	7.270	3.783	1.213	12.738	5.156	75.145	37.529	228.664	64.164	662.526	119.532	161.89	4.25	0.53	−18.10	−4.30	846
10	3.455	31.306	2.561	14.146	8.573	2.717	13.412	3.728	40.743	18.258	111.505	31.762	340.066	58.603	11.79	2.58	0.77	−27.36	−10.03	692
11	22.069	142.028	13.809	72.337	45.613	14.451	71.927	16.584	135.272	45.996	229.645	58.555	590.712	102.190	2.58	1.99	0.77	−21.57	−7.47	831
12	1.595	61.294	1.282	9.480	8.021	3.479	30.704	11.462	152.336	65.569	338.957	81.796	740.137	108.463	43.67	10.51	0.68	−25.46	−6.51	636
13	7.724	112.827	7.780	48.974	33.263	8.927	62.755	15.599	156.366	60.135	312.655	77.928	744.232	120.964	5.08	3.57	0.60	−18.68	−4.92	847
14	1.723	38.519	1.153	7.297	5.866	1.772	14.391	4.376	52.790	23.758	135.894	35.790	365.800	62.099	32.19	6.70	0.59	−20.98	−4.98	745
15	0.196	38.323	0.208	1.739	2.195	0.457	9.803	3.733	54.314	25.552	145.736	38.354	395.316	74.378	259.66	46.55	0.30	−13.85	2.21	742
16	1.219	31.134	0.897	6.042	4.713	1.263	11.617	3.638	49.374	22.689	134.413	35.731	346.129	58.352	37.52	7.30	0.52	−22.78	−5.77	705
17	0.191	24.166	0.139	1.272	1.004	0.389	5.192	2.115	32.298	16.374	97.109	26.303	258.224	41.693	427.18	36.30	0.52	−16.93	0.16	701
18	3.476	53.505	2.936	17.539	11.484	3.114	23.800	6.425	76.017	32.739	184.732	49.648	501.481	88.020	16.51	4.11	0.58	−23.70	−7.29	728
19	0.034	13.819	0.075	0.873	1.147	0.750	7.797	3.055	48.682	26.246	170.269	50.390	559.520	98.481	443.88	67.42	0.77	−13.61	3.01	720
20	4.606	69.388	3.588	21.487	13.088	4.010	24.085	7.099	83.223	34.344	190.733	48.264	448.612	63.398	11.29	4.18	0.69	−23.51	−7.15	730
21	1.188	34.151	1.121	7.268	5.050	1.755	13.553	4.457	56.482	24.828	142.224	37.585	351.817	52.703	31.53	7.26	0.65	−20.94	−4.82	740
22	0.040	14.997	0.033	0.490	0.611	0.313	3.901	1.827	31.912	16.781	109.608	30.640	300.366	46.552	772.36	101.07	0.62	−15.65	2.68	657
23	0.076	36.249	0.276	2.989	3.943	2.286	22.339	8.308	116.657	55.278	309.151	79.145	754.835	126.601	125.00	61.30	0.74	−16.39	1.39	676
24	1.692	40.017	1.484	9.880	6.397	1.690	16.122	4.701	59.101	26.249	152.019	39.598	382.903	57.465	25.43	6.19	0.51	−21.61	−5.46	739
HL-004 porphyritic syenite																				
1	2.434	55.655	0.848	5.528	6.095	1.048	33.214	13.320	177.696	73.991	362.864	84.471	871.229	168.744	174.94	9.50	0.23	−23.25	−5.54	679
2	0.753	47.058	0.330	3.316	4.513	0.962	31.707	11.869	161.604	68.843	343.514	80.123	826.248	162.725	256.82	23.13	0.25	−18.48	−1.46	704
3	3.737	39.389	1.174	6.445	4.825	0.856	27.063	10.206	137.629	59.079	301.573	70.989	738.900	147.779	174.73	4.61	0.23	−27.75	−9.19	649
4	0.012	26.295	0.062	1.494	2.782	0.577	19.845	7.345	96.149	40.083	198.786	44.370	458.363	90.630	209.72	239.97	0.24	−13.05	5.58	646
5	–	30.660	0.063	1.336	3.732	0.697	23.906	8.681	113.805	46.468	226.137	52.056	521.824	102.252	154.35	–	0.23	–	–	665
6	0.159	25.376	0.117	1.372	3.116	0.715	22.841	8.820	115.419	48.967	242.892	57.422	575.771	119.286	212.36	45.53	0.26	−14.06	2.07	740
7	0.063	23.397	0.273	4.080	8.771	2.409	47.824	16.945	211.863	84.280	393.187	88.842	875.397	170.621	35.29	43.78	0.36	−15.07	1.47	723
8	0.103	7.182	0.059	1.031	1.914	0.910	11.250	4.117	56.128	24.534	127.810	31.837	350.131	80.670	111.94	22.64	0.60	−20.52	−2.56	669
9	0.074	45.450	0.112	2.041	4.523	0.792	30.152	11.771	156.127	65.215	316.947	71.741	704.140	144.272	218.20	122.07	0.21	−13.30	4.24	685
10	0.177	18.726	0.103	0.995	2.429	0.439	16.610	6.489	89.513	39.294	199.300	48.671	508.164	105.283	229.77	33.99	0.21	−19.31	−1.20	664
11	0.025	23.494	0.109	2.364	4.899	1.057	28.006	10.443	136.203	56.264	280.486	64.493	642.313	133.408	90.38	110.39	0.28	−17.47	1.89	622
12	55.106	160.296	16.607	82.812	37.621	8.660	125.724	36.302	396.736	140.052	615.416	129.525	1207.961	239.901	19.14	1.30	0.38	−26.17	−10.64	765
13	3.198	41.713	1.025	6.876	5.779	1.073	32.002	11.887	157.986	65.252	320.140	73.948	737.590	149.320	129.47	5.65	0.24	−25.34	−7.57	676
14	0.614	36.880	0.298	2.909	5.001	1.050	29.803	11.148	148.929	64.018	321.582	75.960	758.663	154.583	158.20	21.15	0.26	−18.79	−1.78	705
15	0.026	40.316	0.100	1.350	4.142	0.886	29.183	11.145	150.419	66.473	336.351	79.168	814.557	166.920	269.31	194.32	0.25	−10.12	6.73	711
HL-012 quartz diorite																				
1	–	6.341	0.065	1.233	2.645	1.004	19.552	7.719	103.766	45.090	226.837	52.744	534.509	114.065	106.15	–	0.43	–	–	693
2	0.011	7.114	0.027	0.519	1.593	0.756	12.118	5.191	74.788	35.742	193.064	48.086	516.189	115.921	338.36	103.02	0.53	−11.93	4.65	721
3	–	5.344	0.088	2.102	4.174	1.405	26.319	9.778	125.771	52.207	257.006	58.408	584.402	123.783	39.01	–	0.41	–	–	674
4	0.057	12.906	0.086	1.490	3.686	1.192	27.430	10.820	145.840	63.007	318.202	73.989	745.363	159.029	155.40	45.28	0.36	−15.77	1.17	707
5	0.002	14.704	0.049	1.098	2.822	1.215	22.737	9.312	133.097	59.997	306.119	71.241	721.961	154.808	291.57	335.38	0.46	−6.68	9.51	737
6	0.004	8.446	0.022	0.545	1.811	0.743	14.087	5.795	85.897	41.000	217.645	52.832	562.974	122.968	327.36	230.15	0.45	−8.83	7.71	723
7	0.010	15.055	0.060	1.750	4.093	1.324	28.468	11.202	156.545	68.714	348.335	81.119	806.502	169.688	157.34	146.75	0.37	−10.31	6.13	727
8	0.013	15.286	0.041	1.043	3.030	1.159	26.518	10.814	157.819	73.632	385.510	90.354	903.072	197.239	333.89	160.53	0.40	−10.18	6.36	723
9	0.015	9.871	0.134	2.872	6.711	2.346	45.953	16.804	210.276	86.215	413.591	92.094	885.968	180.888	40.26	53.83	0.41	−16.19	1.26	688
10	–	8.984	0.034	0.516	2.089	0.772	15.330	6.234	91.612	41.690	217.764	52.211	534.448	116.188	246.80	–	0.42	–	–	711
11	0.070	30.053	0.093	1.688	4.700	1.925	42.496	17.256	244.743	107.949	530.074	121.719	1206.497	250.164	341.52	91.05	0.42	−12.09	4.34	727
12	0.007	8.353	0.087	1.675	4.051	1.425	27.692	10.205	141.204	61.472	312.373	73.068	742.780	159.883	84.45	83.65	0.41	−14.21	3.08	694

13	0.013	6.582	0.084	2.411	4.994	1.596	30.534	11.337	146.444	61.383	294.796	65.883	656.762	134.642	36.37	49.52	0.40	−16.40	1.00	690
14	0.013	4.395	0.018	0.398	0.538	0.327	6.263	2.596	35.674	15.790	84.321	20.384	220.626	47.982	729.15	70.94	0.55	−14.81	2.47	694
15	0.169	5.416	0.070	1.596	3.805	1.063	22.163	8.060	104.670	44.458	214.129	49.274	499.065	104.669	40.65	12.26	0.35	−21.83	−4.34	687
16	0.005	6.212	0.040	0.638	1.327	0.494	11.903	4.337	59.377	26.912	136.308	32.415	336.978	72.424	262.52	104.85	0.38	−12.90	4.17	702
17	0.008	8.388	0.036	0.803	2.337	0.890	17.374	7.195	105.605	48.746	253.142	60.325	618.941	134.200	211.93	120.88	0.43	−10.05	5.91	746
18	0.009	7.023	0.017	0.671	2.130	0.718	15.388	6.333	90.944	41.497	222.147	53.250	560.570	124.068	199.51	142.14	0.38	−12.39	4.98	691
19	0.098	8.257	0.036	1.284	3.123	1.306	21.652	8.647	117.888	51.711	264.613	62.039	632.421	137.511	120.58	34.14	0.49	−15.58	0.76	731
20	0.001	6.769	0.042	1.062	2.837	1.019	18.867	7.293	96.577	42.300	214.111	50.343	510.195	110.030	96.40	291.00	0.43	−9.58	7.74	693
21	0.009	11.355	0.070	1.176	3.463	1.127	21.936	8.807	127.533	59.944	314.957	75.451	777.110	169.500	168.45	109.88	0.40	−10.98	5.26	735
22	–	6.534	0.021	0.356	1.550	0.408	10.185	4.118	57.019	25.025	131.321	31.536	331.752	70.980	201.83	–	0.31	–	–	698
23	–	8.848	0.084	1.894	5.072	1.577	30.843	11.496	149.236	63.083	309.600	70.347	697.320	146.385	52.16	–	0.39	–	–	691
24	0.032	7.369	0.045	0.771	2.226	0.718	16.228	6.496	91.515	41.213	209.479	49.722	511.626	111.307	171.06	47.75	0.37	−15.74	1.28	704
25	0.200	7.261	0.149	2.156	4.313	1.230	26.705	10.071	134.689	57.751	287.875	65.162	653.955	136.679	55.16	10.33	0.35	−21.97	−4.73	695
HL-013 quartz diorite																				
1	–	3.928	0.016	0.266	1.107	0.390	7.240	3.166	43.644	19.795	103.593	25.934	273.705	62.461	210.30	–	0.42	–	–	716
2	0.034	10.756	0.127	2.483	5.862	1.576	38.271	14.009	181.630	75.586	366.764	82.389	811.936	169.124	54.45	39.97	0.32	−16.69	0.46	699
3	–	8.579	0.057	1.064	2.602	1.133	21.393	8.534	115.579	53.244	275.997	65.592	666.381	144.024	187.60	–	0.46	–	–	694
4	0.010	4.231	0.026	0.354	1.278	0.374	9.023	3.445	47.270	21.597	113.557	27.526	289.590	63.666	173.17	62.87	0.34	−16.03	1.62	681
5	–	5.074	0.025	0.551	1.820	0.542	13.617	5.296	76.549	34.823	177.335	42.674	445.319	97.823	154.90	–	0.33	–	–	689
6	–	7.493	0.045	0.863	2.090	0.667	15.211	6.245	89.797	41.381	217.198	51.736	536.227	120.280	213.86	–	0.36	–	–	722
7	0.003	6.269	0.023	0.723	1.537	0.580	12.287	4.812	66.077	30.460	160.259	40.266	428.752	96.939	268.49	181.41	0.41	−9.67	6.84	724
8	0.057	7.068	0.039	0.647	1.788	0.716	14.276	5.737	82.472	38.448	201.682	48.795	511.530	113.585	259.52	36.74	0.43	−15.65	0.85	724
9	0.007	3.599	0.080	1.623	3.462	1.118	23.278	8.412	113.361	48.252	235.958	53.410	538.247	114.762	35.11	38.17	0.38	−17.28	0.07	692
10	0.003	7.198	0.021	0.471	1.550	0.572	14.261	5.744	82.866	38.409	201.409	48.288	508.872	112.178	342.57	225.04	0.37	−13.49	5.24	643
11	–	4.282	0.030	0.875	1.930	0.580	11.682	4.340	58.097	25.015	128.322	30.642	314.593	69.798	84.69	–	0.37	–	–	700
12	0.023	9.623	0.205	3.004	7.075	2.329	47.816	17.846	228.304	94.803	452.231	101.262	988.385	206.751	40.41	34.51	0.39	−16.56	0.26	712
13	0.002	5.417	0.074	1.746	3.504	1.049	21.258	7.884	103.421	43.743	213.562	49.834	495.025	106.007	48.51	103.60	0.37	−13.99	3.58	683
14	0.006	10.486	0.037	0.526	2.126	0.770	16.673	6.916	101.465	47.660	254.385	62.213	656.114	144.786	347.11	173.99	0.40	−10.18	6.50	717
15	0.011	5.256	0.006	0.205	0.990	0.418	9.696	4.137	59.314	27.817	150.259	37.904	407.907	91.261	498.42	165.33	0.41	−13.91	4.47	655
16	0.013	9.353	0.063	0.801	2.402	0.726	16.609	6.886	100.278	47.277	249.672	61.506	651.095	143.068	242.26	80.09	0.35	−14.38	2.91	694
17	0.010	6.832	0.089	1.349	3.641	1.317	22.994	8.899	116.674	49.286	242.927	56.736	576.849	124.476	66.59	54.94	0.44	−15.14	1.84	706
18	–	2.903	0.017	0.592	1.532	0.299	11.716	4.567	60.595	26.336	136.869	33.262	346.687	77.243	98.94	–	0.22	–	–	690
19	0.007	4.297	0.026	0.285	1.192	0.437	10.070	4.090	60.844	28.093	148.608	36.342	388.447	86.480	268.32	80.31	0.39	−15.44	2.37	675
20	–	4.717	0.024	0.431	1.332	0.574	9.948	4.065	59.315	27.590	148.123	36.968	400.336	90.065	249.75	–	0.48	–	–	692
21	–	5.139	0.114	1.937	4.640	1.305	25.385	9.292	118.888	49.377	235.304	53.119	533.306	111.638	27.40	–	0.37	–	–	806
22	0.022	8.905	0.022	0.406	1.455	0.445	11.941	4.807	69.600	31.153	159.207	37.946	392.326	83.513	358.71	101.08	0.33	−15.67	2.66	656
23	0.009	7.609	0.055	0.656	2.410	0.814	15.765	6.350	94.034	43.780	234.286	58.055	618.104	136.945	188.55	83.57	0.40	−12.99	3.72	716
24	0.028	7.913	0.144	2.954	6.041	1.831	37.283	13.432	173.949	71.810	345.617	77.641	764.555	156.561	34.70	30.79	0.37	−18.70	−1.05	681
25	–	21.484	0.065	1.623	3.366	1.768	28.579	11.062	153.726	66.010	322.729	72.434	706.590	144.869	277.11	–	0.55	–	–	748
HL-017 granodiorite																				
1	1.460	16.074	0.704	4.742	4.336	1.343	20.066	8.423	119.998	56.963	301.472	72.391	754.371	160.460	220.66	3.89	0.44	−23.14	−7.09	743
2	0.028	16.375	0.052	1.287	3.474	1.162	21.816	9.092	128.198	57.551	294.924	69.536	694.750	144.756	304.77	105.06	0.41	−10.68	5.33	744
3	0.004	6.161	0.054	1.080	2.814	0.914	16.773	6.459	87.572	37.663	196.577	48.016	497.012	107.199	131.56	105.90	0.41	−14.63	3.29	671
4	0.016	16.330	0.107	1.971	5.817	2.093	36.402	13.497	183.678	78.490	383.563	88.381	874.726	177.562	132.92	96.04	0.44	−11.72	4.63	731
5	–	6.742	0.018	0.808	1.617	0.759	11.690	4.513	64.067	28.359	151.650	38.406	409.281	89.829	362.37	–	0.53	–	–	702
6	0.001	5.533	–	0.550	1.399	0.442	11.044	4.216	61.086	28.962	160.327	40.782	443.980	101.078	448.60	–	0.34	–	–	708
7	0.016	5.608	0.051	0.941	2.540	0.902	14.772	5.560	72.986	30.612	158.115	38.194	398.390	87.893	121.19	48.38	0.45	−15.72	1.31	704
8	0.007	11.887	0.064	0.965	3.334	1.264	23.315	9.219	135.074	58.477	302.786	70.770	704.641	146.810	240.76	135.21	0.44	−10.87	5.69	722
9	–	6.964	0.027	0.379	1.671	0.595	11.244	4.813	64.976	28.947	147.529	35.289	368.858	79.601	308.19	–	0.42	–	–	727
10	0.003	5.439	0.009	0.320	1.144	0.407	7.474	3.042	43.571	19.631	101.247	24.358	257.212	54.852	355.63	262.51	0.43	−10.00	7.33	692
11	–	4.483	0.017	0.043	0.700	0.361	6.157	2.586	38.688	16.759	90.891	22.345	235.900	51.602	715.19	–	0.53	–	–	687
12	0.021	8.504	0.027	0.698	1.839	0.578	13.599	5.582	75.898	34.922	187.759	47.582	506.933	111.869	440.51	87.83	0.35	−12.77	3.92	717
13	0.016	10.528	0.043	0.923	2.374	1.008	17.732	7.024	99.520	43.717	225.220	54.185	552.175	120.105	345.87	98.29	0.48	−12.09	4.48	722
14	–	21.153	0.191	4.119	11.036	4.706	72.135	25.536	325.034	129.674	611.042	135.925	1318.595	262.947	69.99	–	0.51	–	–	685
15	–	6.978	0.056	1.196	2.325	0.951	17.627	6.838	98.840	44.402	232.803	56.476	579.178	124.600	248.13	–	0.45	–	–	703
16	0.015	4.536	0.000	0.147	1.122	0.389	8.738	3.564	49.674	22.677	121.824	30.404	330.300	75.113	421.38	589.87	0.38	−7.51	10.09	682
17	0.013	5.668	0.038	0.914	2.189	0.624	13.596	5.534	79.119	34.712	182.802	44.172	478.858	102.466	189.70	63.63	0.35	−14.94	2.21	699
18	–	8.381	0.094	1.824	4.674	1.702	31.407	11.486	148.572	61.319	293.684	67.889	673.234	138.372	81.69	–	0.43	–	–	704

(continued on next page)

Appendix Table A5 (*continued*)

	La	Ce	Pr	Nd	Sm	Eu	Gd	Tb	Dy	Ho	Er	Tm	Yb	Lu	Ce^{4+}/Ce^{3+}	Ce/Ce*	Eu/Eu*	$\log(fO_2)$	ΔFMQ	T °C
19	–	5.420	0.066	1.326	2.358	0.990	14.125	5.470	75.923	32.131	167.693	41.035	431.335	96.060	147.73	–	0.52	–	–	711
20	–	4.702	0.018	0.596	1.450	0.607	11.798	4.878	68.065	30.118	154.656	38.761	404.860	89.377	306.42	–	0.45	–	–	698
21	0.033	6.632	0.058	0.534	1.964	0.660	11.832	4.460	62.551	28.194	146.117	35.198	370.751	80.126	218.14	37.17	0.42	−15.79	0.80	721
22	–	11.092	0.074	0.830	2.031	0.935	16.447	6.571	93.372	43.633	231.965	58.024	615.896	128.935	535.37	–	0.49	–	–	724
23	0.007	5.493	0.038	0.717	1.953	0.683	12.910	4.804	67.906	31.067	160.571	40.526	431.222	96.219	219.07	84.84	0.42	−13.46	3.50	706
24	0.001	4.554	0.045	0.339	1.079	0.282	8.581	3.101	42.591	19.667	101.217	24.241	257.344	56.667	346.02	219.97	0.28	−12.07	5.94	668
25	–	5.316	0.043	0.706	1.766	0.742	13.312	5.226	74.976	32.967	173.699	42.293	448.045	98.425	259.61	–	0.47	–	–	709
HL-037 granodiorite porphyry																				
1	0.012	5.786	0.035	0.543	1.259	0.585	10.562	4.035	57.510	25.388	134.469	32.949	348.515	77.996	362.76	68.61	0.49	−14.50	2.57	702
2	0.034	7.594	0.042	0.818	1.939	1.126	11.372	4.175	56.560	24.720	131.822	33.568	377.692	90.810	245.79	49.43	0.73	−18.62	−0.16	652
3	0.014	6.765	0.012	0.248	0.499	0.319	4.640	1.963	25.019	11.798	65.821	17.139	195.020	48.433	1703.76	124.50	0.64	−16.38	2.67	632
4	0.015	7.747	0.018	0.297	0.726	0.495	6.828	2.780	40.256	19.163	108.799	28.407	332.960	80.899	1533.58	114.36	0.68	−14.46	3.52	669
5	0.670	4.901	0.092	0.369	0.602	0.326	5.421	2.261	31.682	14.530	79.145	19.771	217.867	51.027	879.77	4.84	0.55	−25.27	−7.81	687
6	–	6.740	0.007	0.180	0.712	0.385	5.313	2.075	31.472	14.739	83.985	21.410	239.134	56.659	983.95	–	0.61	–	–	668
7	0.147	9.300	0.064	0.350	1.036	0.491	8.048	3.081	44.654	21.057	115.936	30.180	346.157	82.357	933.97	23.58	0.52	−20.56	−2.51	666
8	0.001	6.653	0.008	0.411	0.877	0.362	5.904	2.304	34.071	17.303	95.628	25.308	292.500	73.701	851.05	651.03	0.49	−7.16	10.45	682
9	0.023	11.129	0.147	2.471	6.334	2.147	45.594	16.752	219.815	88.707	424.711	94.389	943.169	195.136	67.97	46.64	0.39	−16.04	1.08	700
10	0.030	7.715	0.015	0.393	1.115	0.378	5.843	2.426	36.403	18.040	104.390	27.886	324.915	81.041	683.77	87.45	0.45	−15.68	2.40	665
11	0.011	8.183	0.003	0.220	0.877	0.536	6.816	2.854	40.443	19.693	109.369	28.727	329.148	80.656	1123.17	346.36	0.67	−9.83	7.92	677
12	–	8.298	0.026	0.325	1.051	0.535	7.533	2.818	38.720	17.465	94.793	24.218	268.345	62.622	619.70	–	0.58	–	–	675
13	0.004	7.544	0.011	0.269	0.681	0.434	6.002	2.548	40.130	19.129	106.804	28.297	320.967	77.200	1606.44	300.39	0.66	−12.43	6.31	642
14	0.001	7.325	0.022	0.302	0.752	0.421	6.744	2.532	36.588	17.058	94.368	24.706	273.843	64.670	1082.71	451.58	0.57	−7.85	9.43	694
15	–	6.569	0.020	0.378	0.807	0.452	5.286	2.048	30.017	14.259	80.528	21.325	246.436	60.694	816.60	–	0.67	–	–	653
16	0.002	7.406	0.008	0.260	0.620	0.444	6.020	2.551	35.529	17.031	97.272	25.927	298.134	73.167	1813.57	490.81	0.70	−8.21	9.39	682
17	0.006	6.389	0.028	0.234	0.736	0.390	5.255	2.229	32.310	15.143	84.123	22.112	256.006	62.713	970.78	120.48	0.61	−14.36	3.66	667
18	0.034	20.134	0.056	1.134	2.906	1.350	21.244	8.259	119.018	53.077	275.966	66.567	707.379	160.301	492.32	112.85	0.53	−11.91	4.82	715
19	–	5.008	0.012	0.686	2.023	0.793	14.998	5.747	77.006	32.917	164.732	39.406	401.750	86.843	135.44	–	0.44	–	–	682
20	0.010	7.272	0.024	0.330	1.387	0.681	9.217	3.181	46.788	20.783	113.503	29.153	323.092	78.448	393.94	114.15	0.58	−14.48	3.50	669
21	–	8.211	0.043	0.244	0.914	0.523	7.452	3.151	44.355	20.772	113.559	29.245	329.955	78.698	999.50	–	0.61	–	–	683
22	0.016	10.216	0.005	0.390	0.913	0.467	6.611	2.543	33.850	15.266	80.159	19.986	222.318	53.395	859.45	289.37	0.58	−10.88	7.05	670
23	0.008	5.956	0.008	0.261	0.690	0.298	5.076	1.951	28.485	12.963	74.081	19.318	221.983	54.869	905.40	183.01	0.49	−12.34	5.46	675
24	–	6.931	0.013	0.162	0.807	0.475	5.725	2.476	37.968	18.172	102.409	27.048	311.121	76.641	1066.49	–	0.68	–	–	673
25	0.009	5.464	0.049	0.757	1.751	0.956	11.966	4.881	62.631	28.205	147.590	36.749	404.052	94.807	221.25	64.50	0.64	−15.85	1.76	682
HL-027 diorite porphyry																				
1	0.004	11.337	0.046	0.661	2.138	0.900	11.670	4.867	64.585	29.473	159.839	40.926	464.461	104.735	407.24	201.40	0.55	−11.96	5.84	675
2	0.443	10.772	0.134	0.834	1.694	0.697	10.463	3.954	57.582	26.735	143.782	36.255	412.853	96.218	560.65	10.83	0.51	−22.67	−5.00	680
3	0.007	8.863	0.023	0.593	0.977	0.577	7.994	3.190	43.812	20.967	115.211	30.522	343.000	82.248	1154.27	172.23	0.63	−11.81	5.63	688
4	1.136	11.248	0.242	1.425	1.546	0.706	8.350	3.396	48.468	21.670	119.559	30.967	362.296	82.660	612.68	5.25	0.60	−24.78	−7.40	691
5	0.043	11.736	0.040	0.753	1.472	0.909	11.407	4.427	64.120	28.406	157.792	39.732	453.275	103.846	855.02	68.76	0.68	−14.63	2.51	699
6	–	9.051	0.008	0.238	1.101	0.570	6.698	2.854	43.208	20.084	110.416	29.332	339.453	79.365	913.83	–	0.64	–	–	677
7	0.223	7.149	0.025	0.908	1.363	0.823	8.758	3.244	45.870	20.102	110.533	28.612	322.343	74.726	437.07	23.54	0.73	−21.07	−2.77	658
8	0.042	9.455	0.058	0.727	1.926	0.795	12.454	4.580	64.205	27.609	141.168	35.137	375.857	80.960	313.21	46.77	0.50	−16.73	0.72	688
9	0.035	12.578	0.069	1.060	1.723	0.999	11.476	4.801	65.630	30.063	160.734	41.491	450.749	105.492	686.49	63.08	0.69	−14.26	2.55	712
10	0.124	9.449	0.014	0.230	1.246	0.677	9.504	3.763	54.946	25.058	137.885	35.506	407.369	90.947	838.52	55.77	0.60	−15.97	1.44	690
11	0.274	9.062	0.077	0.634	1.653	0.839	12.559	4.339	59.973	26.403	137.023	35.195	400.666	87.643	440.16	15.27	0.56	−23.39	−4.76	646
12	0.027	12.164	0.042	0.313	0.976	0.596	8.759	3.574	52.493	24.245	130.466	32.878	370.501	86.384	1617.82	87.83	0.62	−14.52	3.01	685
13	–	10.097	0.066	1.243	2.676	0.988	15.478	5.909	79.355	34.147	176.306	43.214	464.463	101.530	218.29	–	0.47	–	–	672
14	0.049	8.470	0.066	0.413	1.333	0.683	8.537	3.464	49.797	23.296	124.646	32.262	371.081	84.123	610.91	36.40	0.62	−17.56	−0.16	690
15	0.078	7.282	0.057	0.627	1.275	0.620	8.660	3.365	45.418	20.916	115.461	30.061	335.600	82.430	562.03	26.70	0.57	−18.67	−1.30	691
16	0.014	7.699	0.025	0.895	1.552	0.853	9.605	3.725	52.396	23.721	126.776	32.921	374.894	83.915	404.01	101.25	0.68	−10.38	5.42	753

17	0.107	9.020	0.054	0.417	1.307	0.779	8.937	3.559	51.669	23.552	129.968	34.666	392.230	90.268	728.18	29.03	0.70	−18.15	−0.87	694
18	0.049	11.875	0.045	0.972	1.717	0.873	12.770	4.772	64.701	28.778	153.449	39.733	439.848	103.929	644.48	62.53	0.57	−17.43	0.88	657
19	–	8.382	0.058	0.957	1.772	0.919	10.731	4.140	56.511	25.129	135.519	35.126	392.029	90.557	369.53	–	0.64	–	–	681
20	1.110	10.002	0.200	1.500	1.671	0.782	10.247	4.184	56.149	25.717	138.074	35.759	402.153	93.160	520.81	5.20	0.58	−23.21	−6.60	720
HL-028 diorite porphyry																				
1	–	8.055	0.033	0.300	1.569	0.768	9.714	3.697	53.754	24.385	131.703	33.217	376.886	85.710	564.33	–	0.60	–	–	660
2	0.011	3.535	0.005	0.267	0.550	0.326	5.610	2.218	31.335	13.918	72.519	18.133	196.860	43.017	959.43	111.53	0.57	−13.58	3.93	686
3	0.019	14.522	0.019	0.802	2.179	0.760	16.112	6.576	89.856	39.834	208.221	50.659	517.026	111.642	664.89	190.88	0.39	−11.33	6.07	690
4	–	6.197	–	0.276	0.481	0.352	4.354	1.794	24.894	11.350	65.029	16.979	201.136	46.948	2466.26	–	0.74	–	–	652
5	0.941	9.875	0.264	1.566	2.036	0.911	12.127	4.445	58.177	25.939	135.746	34.144	368.693	82.220	397.33	4.86	0.56	−25.95	−8.15	675
6	0.005	10.836	0.030	0.485	1.605	0.725	10.529	4.065	56.971	25.636	136.072	35.190	383.586	86.416	727.29	223.74	0.54	−11.72	6.15	673
7	0.007	8.089	0.025	0.166	0.679	0.433	6.351	2.614	39.225	19.302	108.906	28.786	324.408	77.740	2657.94	149.41	0.64	−13.29	4.61	672
8	0.016	6.058	0.033	0.271	0.702	0.295	4.345	1.839	27.992	13.159	76.504	20.244	238.884	56.288	1395.00	64.67	0.52	−14.69	2.37	703
9	–	7.516	0.021	0.565	1.147	0.707	9.161	3.512	51.446	23.291	128.282	32.973	373.348	87.405	985.84	–	0.67	–	–	665
10	–	9.520	0.010	0.316	1.341	0.573	7.880	3.158	44.149	21.000	113.638	29.553	332.619	80.402	868.37	–	0.54	–	–	680
11	–	8.765	0.011	0.550	0.586	0.420	6.528	2.532	39.278	18.698	104.564	27.930	330.013	76.142	3734.32	–	0.66	–	–	678
12	0.006	9.680	0.030	0.537	1.044	0.649	8.881	3.603	51.122	24.099	134.511	35.143	403.145	92.534	1618.66	177.23	0.65	−12.34	5.41	677
13	0.277	24.293	0.099	1.141	2.404	1.349	16.778	5.427	68.473	28.450	142.976	35.409	381.124	84.978	719.17	35.95	0.65	−18.79	−0.82	669
14	0.028	20.180	0.247	3.955	10.576	3.726	69.432	24.809	325.060	130.493	622.447	141.402	1338.991	265.313	92.25	59.26	0.42	−15.80	1.63	688
15	0.043	7.703	0.030	0.660	1.107	0.593	7.399	3.051	40.738	18.424	103.272	26.358	305.451	71.108	899.53	52.54	0.63	−15.32	1.67	705
16	0.031	6.399	–	0.188	0.727	0.537	5.994	2.364	36.502	17.632	99.923	26.979	315.140	74.511	1783.59	–	0.79	–	–	671
17	–	7.702	0.017	0.284	0.599	0.430	5.093	2.165	32.056	15.444	84.231	22.170	253.888	60.234	2533.13	–	0.75	–	–	668
18	0.020	10.454	0.009	0.299	0.865	0.563	6.732	2.645	39.017	18.284	97.893	26.146	297.553	68.745	1899.48	193.49	0.71	−13.09	5.18	659
19	–	9.415	0.010	0.361	0.745	0.550	6.964	2.779	40.746	19.407	107.754	28.596	327.002	77.109	2555.85	–	0.74	–	–	668
20	0.010	7.374	0.017	0.351	0.726	0.524	6.499	2.721	39.565	19.023	107.532	28.155	331.701	78.968	2167.91	138.18	0.74	−13.16	4.53	679
21	0.010	8.942	0.042	0.943	2.671	1.047	13.768	5.147	67.031	28.803	148.881	37.244	412.910	93.329	239.33	108.06	0.53	−14.61	3.33	670
22	0.023	7.654	0.016	0.261	1.045	0.588	6.914	2.829	40.658	19.829	109.730	29.371	343.464	80.678	1143.11	97.92	0.67	−15.12	2.89	668
23	0.006	11.002	0.023	0.441	1.607	0.676	10.907	4.174	62.708	28.817	154.341	39.723	437.945	101.069	857.53	223.78	0.49	−11.10	6.48	683
24	0.035	9.740	0.042	0.850	1.929	0.964	12.927	5.196	69.739	30.679	159.945	38.952	416.074	91.539	473.65	62.70	0.59	−14.91	2.20	701
HL-011 alkali granite porphyry																				
1	0.306	14.012	0.285	4.264	8.649	1.646	44.745	15.518	187.628	71.738	319.273	69.510	646.730	127.398	15.64	11.65	0.26	−22.04	−4.55	686
2	1.235	9.516	0.447	2.610	2.228	0.151	11.125	3.805	44.637	17.037	79.527	17.927	176.045	35.712	47.61	3.14	0.09	−25.85	−8.89	706
3	43.212	133.185	14.486	68.613	18.652	0.488	41.648	12.911	153.085	59.343	279.959	63.452	609.450	114.289	32.65	1.31	0.05	−27.82	−11.50	731
4	1.216	15.175	0.497	4.141	4.562	0.943	25.421	10.158	138.149	57.430	282.465	64.762	634.180	124.454	61.58	4.79	0.27	−25.22	−7.80	689
5	0.124	13.207	0.313	4.213	6.393	0.258	27.234	8.448	95.156	36.120	155.983	34.060	319.321	64.596	14.06	16.41	0.06	−19.69	−2.70	705
6	11.563	48.622	5.560	31.475	12.829	1.415	26.796	8.108	86.872	32.379	141.792	30.622	291.702	55.960	11.78	1.49	0.23	−26.38	−10.51	750
7	0.156	16.512	0.772	12.952	17.653	0.463	68.217	19.849	213.565	73.680	309.006	64.600	598.884	115.101	3.41	11.65	0.04	−20.81	−3.90	708
8	1.504	16.225	1.200	7.733	8.807	1.085	42.770	14.199	167.555	62.751	279.501	60.075	560.244	110.226	15.24	2.96	0.17	−25.03	−8.57	726
9	0.063	8.127	0.271	5.114	8.778	0.647	40.813	12.840	147.672	53.823	234.515	49.657	459.682	89.532	5.69	15.30	0.10	−22.21	−4.14	666
10	0.068	9.695	0.128	1.461	3.553	0.237	17.672	6.193	75.307	30.677	139.239	30.796	296.360	60.132	31.62	25.44	0.09	−19.09	−1.60	687
11	0.953	7.115	0.450	2.543	3.579	0.322	15.078	5.265	66.826	27.081	131.489	28.882	285.760	60.343	23.14	2.66	0.13	−24.30	−8.38	748
12	0.156	8.745	0.178	2.246	3.308	0.360	15.850	5.597	68.334	25.900	120.486	26.554	261.776	50.523	27.44	12.87	0.15	−21.19	−3.92	695
13	4.834	36.696	2.389	15.967	16.044	1.531	68.206	21.833	240.568	85.995	364.018	74.693	678.707	134.302	12.63	2.65	0.14	−24.09	−8.27	753
14	0.204	9.116	0.374	4.139	6.217	0.570	27.395	8.635	101.083	38.101	171.225	37.634	365.500	73.011	11.37	8.10	0.13	−21.36	−4.84	724
15	0.163	9.424	0.294	3.756	6.785	0.519	33.566	11.034	132.038	48.355	217.107	47.048	454.690	86.792	11.48	10.54	0.11	−23.46	−5.46	668
16	0.229	12.769	0.181	3.197	4.999	0.489	24.431	8.361	101.418	38.732	176.861	37.979	356.240	70.588	24.35	15.35	0.14	−20.06	−3.01	703
17	0.015	8.967	0.147	2.415	4.089	0.499	23.539	8.479	108.290	44.019	205.412	45.227	428.474	88.544	31.93	47.40	0.16	−15.09	1.60	717
18	0.037	7.375	0.354	6.040	10.693	0.837	49.540	16.069	178.025	64.091	277.129	57.380	524.279	102.993	3.69	15.77	0.11	−20.31	−3.10	697
19	1.345	18.075	0.824	8.846	13.293	0.754	52.962	17.198	193.152	70.832	309.819	66.301	624.022	117.762	7.65	4.21	0.09	−24.89	−7.86	704
20	6.341	23.924	2.169	12.835	7.584	0.519	25.738	8.401	99.381	38.572	178.640	40.988	392.240	79.642	23.46	1.58	0.11	−24.33	−9.33	788
21	0.030	6.116	0.119	2.107	4.248	0.314	21.887	6.956	85.758	32.799	154.668	35.680	349.152	69.876	15.82	25.22	0.10	−18.23	−1.17	703
22	0.081	7.662	0.329	4.831	10.104	0.864	46.761	15.264	171.928	63.758	286.257	61.020	569.460	110.987	4.92	11.47	0.12	−19.69	−3.35	731
23	0.298	9.201	0.203	1.655	2.924	0.226	14.464	5.220	65.941	25.771	118.607	26.543	259.330	50.368	36.96	9.18	0.11	−23.32	−5.64	679
24	1.951	13.710	0.574	5.165	6.037	0.200	25.500	7.660	85.772	31.498	140.076	29.872	281.621	54.962	13.92	3.18	0.05	−20.03	−5.83	826

References

Badarch, G., Cunningham, W.D., Windley, B.F., 2002. A new terrane subdivision for Mongolia: implications for the Phanerozoic crustal growth of Central Asia. J. Asian Earth Sci. 21, 87–110.

Ballard, J.R., Palin, M.J., Campbell, I.H., 2002. Relative oxidation states of magmas inferred from Ce(IV)/Ce(III) in zircon: application to porphyry copper deposits of northern Chile. Contrib. Mineral. Petrol. 144, 347–364.

Beard, J.S., Lofgren, G.E., 1991. Dehydration melting and water-saturated melting of basaltic and andesitic greenstones and amphibolites at 1, 3, and 6.9 kb. J. Petrol. 32, 365–401.

Bissig, T., Clark, A.H., Lee, J.K.W., Quadt, A.V., 2003. Petrogenetic and metallogenetic responses to Miocene slab flattening: new constraints from the El Indio-Pascua Au–Ag–Cu belt, Chile/Argentina. Mineral. Deposita 38, 844–862.

Black, L.P., Kamo, S.L., Allen, C.M., Aleinikoff, J.N., Davis, D.W., Korsch, R.J., Foudoulis, C., 2003. TEMORA 1: a new zircon standard for Phanerozoic U–Pb geochronology. Chem. Geol. 200, 155–170.

Bouvier, A., Vervoort, J.D., Patchett, P.J., 2008. The Lu–Hf and Sm–Nd isotopic composition of CHUR: constraints from unequilibrated chondrites and implications for the bulk composition of terrestrial planets. Earth Planet. Sci. Lett. 273, 48–57.

Brandon, A.D., Draper, D.S., 1996. Constraints on the origin of the oxidation state of mantle overlying subduction zones: an example from Simcoe, Washington, USA. Geochim. Cosmochim. Acta 60, 1739–1749.

Cai, K.D., Sun, M., Yuan, C., Zhao, G.C., Xiao, W.J., Long, X.P., Wu, F.Y., 2011. Prolonged magmatism, juvenile nature and tectonic evolution of the Chinese Altai, NW China: evidence from zircon U–Pb and Hf isotopic study of Paleozoic granitoids. J. Asian Earth Sci. 42, 949–968.

Candela, P.A., 1997. A review of shallow, ore-related granites: textures, volatiles, and ore metals. J. Petrol. 38, 1619–1633.

Carroll, A.R., Liang, Y.H., Graham, S.A., Xiao, X.C., Hendrix, M.S., Chu, J.C., McKnight, C.L., 1990. Junggar basin, northwest China: trapped late Paleozoic ocean. Tectonophysics 181, 1–14.

Chen, B., Jahn, B.M., 2004. Genesis of post-collisional granitoids and basement nature of the Junggar Terrane, NW China: Nd–Sr isotope and trace element evidence. J. Asian Earth Sci. 23, 691–703.

Chernyshev, I.V., Chugaev, A.V., Shatagin, K.N., 2007. High-precision Pb isotope analysis by multicollector–ICP–mass-spectrometry using $^{205}Tl/^{203}Tl$ normalization: optimization and calibration of the method for the studies of Pb isotope variations. Geochem. Int. 45, 1065–1076.

Coleman, R.G., 1989. Continental growth of northwest China. Tectonics 8, 621–635.

Czamanske, G.K., Wones, D.R., 1973. Oxidation during magmatic differentiation, Finnmarka complex, Oslo area, Norway: part 2, the mafic silicates. J. Petrol. 14, 349–380.

Dilles, J.H., 1987. Petrology of the Yerington Batholith, Nevada; evidence for evolution of porphyry copper ore fluids. Econ. Geol. 82, 1750–1789.

Dobosi, G., Kempton, P.D., Downes, H., Embey-Isztin, A., Thirlwall, M., Greenwood, P., 2003. Lower crustal granulite xenoliths from the Pannonian Basin, Hungary, part 2: Sr–Nd–Pb–Hf and O isotope evidence for formation of continental lower crust by tectonic emplacement of oceanic crust. Contrib. Mineral. Petrol. 144, 671–683.

Dong, L.H., Li, F.M., 2006. Metallogenic regularity and prospecting targets of porphyry copper deposits in northern Xinjiang. Miner. Depos. 25, 293–296 (in Chinese).

Dong, L.H., Xu, X.W., Qu, X., Li, G.M., 2009. Tectonic setting and formation mechanism of the circum-Junggar porphyritic copper deposit belts. Acta Petrol. Sin. 25, 713–737 (in Chinese with English abstract).

Eastoe, C.J., 1982. Physics and chemistry of the hydrothermal system at the Panguna porphyry copper deposit, Bougainville, Papua New Guinea. Econ. Geol. 77, 127–153.

Faure, G., 1986. Principles of Isotope Geology. John Wiley & Sons Inc., New York.

Feng, J., Zhang, Z.C., 2009. Geochemistry of the intermediate-acid porphyries on southern margin of the Altay Mountains and its implications for petrogenesis. Geol. Rev. 55, 58–72 (in Chinese with English abstract).

Ferry, J.M., Watson, E.B., 2007. New thermodynamic models and revised calibrations for the Ti-in-zircon and Zr-in-rutile thermometers. Contrib. Mineral. Petrol. 154, 429–437.

Fu, B., Page, F.Z., Cavosie, A.J., Fournelle, J., Kita, N.T., Lackey, J.S., Wilde, S.A., Valley, J.W., 2008. Ti-in-zircon thermometry: applications and limitations. Contrib. Mineral. Petrol. 156, 197–215.

Gao, S., Liu, X.M., Yuan, H.L., Hattendorf, B., Günther, D., Chen, L., Hu, S.H., 2002. Determination of forty two major and trace elements in USGS and NIST SRM glasses by laser ablation–inductively coupled plasma-mass spectrometry. Geostand. Newslett. 26, 181–196.

Ge, S.M., Bo, M.X., Xu, D.Z., Xiang, Z.Y., 1986. Recurrence intervals of major earthquakes for the Koktokay–Ertai fault. Seismol. Geol. 3, 1–9 (in Chinese with English abstract).

Geng, X.X., Yang, F.Q., Zhang, Z.X., Liu, F., Chai, F.M., Gao, G.J., 2013. Ore-forming fluid of Yulekenhalasu Cu–Mo deposit on the northern margin of Junggar basin, Xinjiang. Geol. Rev. 59, 235–247 (in Chinese with English abstract).

Griffin, W.L., Wang, X., Jackson, S.E., Pearson, N.J., O'Reilly, S.Y., Xu, X.S., Zhou, X.M., 2002. Zircon chemistry and magma mixing, SE China: in-situ analysis of Hf isotopes, Tonglu and Pingtan igneous complexes. Lithos 61, 237–269.

Grochau, B., Johannes, W., 1997. Stability of phlogopite in granitic melts, an experimental investigation. Contrib. Mineral. Petrol. 126, 315–330.

Grove, T.L., Chatterjee, N., Parman, S.W., Médard, E., 2006. The influence of H_2O on mantle wedge melting. Earth Planet. Sci. Lett. 249, 74–89.

Gustafson, L.B., Hunt, J.P., 1975. The porphyry copper deposit at El Salvador, Chile. Econ. Geol. 70, 857–912.

Gutscher, M.A., Maury, R., Eissen, J.P., Bourdon, E., 2000. Can slab melting be caused by flat subduction? Geology 28, 535–538.

Han, B.F., 2008. A preliminary comparison of Mesozoic granitoids and rare metal deposits in Chinese and Russian Altai Mountains. Acta Petrol. Sin. 24, 655–660 (in Chinese with English abstract).

Han, B.F., Wang, S.G., Jahn, B.M., Hong, D.W., Kagami, H., Sun, Y.L., 1997. Depleted-mantle source for the Ulungur River A-type granites from North Xinjiang, China: geochemistry and Nd–Sr isotopic evidence, and implications for Phanerozoic crustal growth. Chem. Geol. 138, 135–159.

Han, B.F., He, G.Q., Wang, S., 1999. Postcollisional mantle-derived magmatism, underplating and implications for basement of the Junggar Basin. Sci. China Ser. D 42, 113–119.

Han, B.F., Ji, J.Q., Song, B., Chen, L.H., Li, Z.H., 2004. SHRIMP zircon U–Pb ages of Kalatongke and Huangshandong Cu–Ni-bearing mafic–ultramafic complexes, North Xinjiang, and geological implications. Chin. Sci. Bull. 49, 2424–2429.

He, G.Q., Cheng, S.D., Xu, X., Li, J.Y., Hao, J., 2004. An Introduction to the Explanatory Text of the Map of Tectonics of Xinjiang and Its Neighbouring Areas. Geological Publishing House, Beijing, pp. 1–65 (in Chinese).

Hedenquist, J.W., Lowenstern, J.B., 1994. The role of magmas in the formation of hydrothermal ore deposits. Nature 370, 519–527.

Heinhorst, J., Lehmann, B., Ermolov, P., Serykh, V., Zhurutin, S., 2000. Paleozoic crustal growth and metallogeny of Central Asia: evidence from magmatic–hydrothermal ore systems of Central Kazakhstan. Tectonophysics 328, 69–87.

Henley, R.W., McNabb, A., 1978. Magmatic vapor plumes and ground-water interaction in porphyry copper emplacement. Econ. Geol. 73, 1–20.

Holtz, F., Johannes, W., Tamic, N., Behrens, H., 2001. Maximum and minimum water contents of granitic melts generated in the crust: a reevaluation and implications. Lithos 56, 1–14.

Hoskin, P.W., Ireland, T.R., 2000. Rare earth element chemistry of zircon and its use as a provenance indicator. Geology 28, 627–630.

Hoskin, P.W., Schaltegger, U., 2003. The composition of zircon and igneous and metamorphic petrogenesis. Rev. Mineral. Geochem. 53, 27–62.

Hu, A.Q., Jahn, B.M., Zhang, G.X., Chen, Y.B., Zhang, Q.F., 2000. Crustal evolution and Phanerozoic crustal growth in northern Xinjiang: Nd isotopic evidence. Part I. Isotopic characterization of basement rocks. Tectonophysics 328, 15–51.

Jahn, B.M., 2004. The Central Asian Orogenic Belt and growth of the continental crust in the Phanerozoic. Geol. Soc. Spec. Publ. 226, 73–100.

Jahn, B.M., Wu, F.Y., Chen, B., 2000. Granitoids of the Central Asian Orogenic Belt and continental growth in the Phanerozoic. Geol. Soc. Am. Spec. Pap. 350, 181–193.

Jiang, Y.D., Sun, M., Zhao, G.C., Yuan, C., Xiao, W.J., Xia, X.P., Long, X.P., Wu, F.Y., 2010. The ~390 Ma high-T metamorphic event in the Chinese Altai: a consequence of ridge-subduction? Am. J. Sci. 310, 1421–1452.

Khain, E.V., Bibikova, E.V., Salnikova, E.B., Kröner, A., Gibsher, A.S., Didenko, A.N., Degtyarev, K.E., Fedotova, A.A., 2003. The Palaeo-Asian ocean in the Neoproterozoic and early Palaeozoic: new geochronologic data and palaeotectonic reconstructions. Precambrian Res. 122, 329–358.

Kovalenko, V.I., Yarmolyuk, V.V., Kovach, V.P., Kotov, A.B., Kozakov, I.K., Salnikova, E.B., Larin, A.M., 2004. Isotope provinces, mechanisms of generation and sources of the continental crust in the Central Asian mobile belt: geological and isotopic evidence. J. Asian Earth Sci. 23, 605–627.

Laurent-Charvet, S., Charvet, J., Shu, L.S., Ma, R.S., Lu, H.f., 2002. Palaeozoic late collisional strike–slip deformations in Tianshan and Altay, Eastern Xinjiang, NW China. Terra Nova 14, 249–256.

Li, C.Y., Zhang, H., Wang, F.Y., Liu, J.Q., Sun, Y.L., Hao, X.L., Li, Y.L., Sun, W.D., 2012. The formation of the Dabaoshan porphyry molybdenum deposit induced by slab rollback. Lithos 150, 101–110.

Li, Q., Zhang, Z.X., Geng, X.X., Li, C., Liu, F., Chai, F.M., Yang, F.Q., 2014. Geology and geochemistry of the Qiaoxiahala Fe–Cu–Au deposit, Junggar region, northwest China. Ore Geol. Rev. 57, 462–481.

Liang, H.Y., Campbell, I.H., Allen, C., Sun, W.D., Liu, C.Q., Yu, H.X., Xie, Y.W., Zhang, Y.Q., 2006. Zircon Ce^{4+}/Ce^{3+} ratios and ages for Yulong ore-bearing porphyries in eastern Tibet. Mineral. Deposita 41, 152–159.

Liu, T.G., Yu, X.Y., Mei, H.J., 1991. The Duolanasayi–Kalaxiange'er porphyry copper–gold metallogenic belt. Geol. Geochem. 2, 71–74 (in Chinese with English abstract).

Liu, D., Tang, Y., Zhou, R., 1993. The Devonian intra-oceanic arc and boninite in the North Junggar, Xinjiang. Xinjiang Geol. 11, 1–12 (in Chinese with English abstract).

Liu, Y.S., Hu, Z.C., Gao, S., Günther, D., Xu, J., Gao, C.G., Chen, H.H., 2008. In situ analysis of major and trace elements of anhydrous minerals by LA–ICP-MS without applying an internal standard. Chem. Geol. 257, 34–43.

Liu, G.R., Dong, L.H., Xue, C.J., Li, X.R., Zhang, L.W., Wei, G.Z., He, L.X., Zhao, Z.H., Qin, J.H., Zhang, Z.X., 2010. Geological characteristics and exploration direction of the Yulekenhalasu copper deposit, Xinjiang. Xinjiang Geol. 28, 377–384 (in Chinese with English abstract).

Long, X.P., Yuan, C., Sun, M., Xiao, W.J., Zhao, G.C., Wang, Y.J., Cai, K.D., Xia, X.P., Xie, L.W., 2010. Detrital zircon ages and Hf isotopes of the early Paleozoic flysch sequence in the Chinese Altai, NW China: new constrains on depositional age, provenance and tectonic evolution. Tectonophysics 480, 213–231.

Lü, S.J., Yang, F.Q., Chai, F.M., Zhang, X.B., Jiang, L.P., Liu, F., Zhang, Z.X., Geng, X.X., Ouyang, L.J., 2012. Zircon U–Pb dating for intrusions in Laoshankou ore district in northern margin of East Junggar and their significances. Geol. Rev. 58, 149–164 (in Chinese with English abstract).

Ludwig, K.R., 2003. User's Manual for Isoplot 3.00: A Geochronological Toolkit for Microsoft Excel. Special Publication 4. Berkeley Geochronology Center, Berkeley (70 pp.).

Mao, J.W., Pirajno, F., Lehmann, B., Luo, M.C., Berzina, A., 2014. Distribution of porphyry deposits in the Eurasian continent and their corresponding tectonic settings. J. Asian Earth Sci. 79, 576–584.

Mossakovsky, A.A., Ruzhentsev, S.V., Samygin, S.G., Kheraskova, T.N., 1994. Central Asian fold belt: geodynamic evolution and formation history. Geotectonics 27, 445–474.

MuÈntener, O., Kelemen, P.B., Grove, T.L., 2001. The role of H_2O during crystallization of primitive arc magmas under uppermost mantle conditions and genesis of igneous pyroxenites: an experimental study. Contrib. Mineral. Petrol. 141, 643–658.

Mungall, J.E., 2002. Roasting the mantle: slab melting and the genesis of major Au and Au-rich Cu deposits. Geology 30, 915–918.

Mungall, J.E., Hanley, J.J., Arndt, N.T., Debecdelievre, A., 2006. Evidence from meimechites and other low-degree mantle melts for redox controls on mantle–crust fractionation of platinum-group elements. Proc. Natl. Acad. Sci. U. S. A. 103, 12695–12700.

Muñoz, M., Charrier, R., Fanning, C.M., Maksaev, V., Deckart, K., 2012. Zircon trace element and O–Hf isotope analyses of mineralized intrusions from El Teniente ore deposit, Chilean Andes: constraints on the source and magmatic evolution of porphyry Cu–Mo related magmas. J. Petrol. 1091–1122.

Mysen, B.O., Boettcher, A.L., 1975. Melting of a hydrous mantle: I. Phase relations of natural peridotite at high pressures and temperatures with controlled activities of water, carbon dioxide, and hydrogen. J. Petrol. 16, 520–548.

Niu, H.C., Xu, J., Yu, X.Y., Chen, F.R., Zheng, Z.P., 1999. Discovery of Mg rich volcanic rock series in western Altay area, Xinjiang and its geologic significance. Chin. Sci. Bull. 44, 1685–1687 (in Chinese with English abstract).

Niu, H.C., Sato, H., Zhang, H.X., Ito, J.I., Yu, X.Y., Nagao, T., Terada, K., Zhang, Q., 2006. Juxtaposition of adakite, boninite, high-TiO_2 and low-TiO_2 basalts in the Devonian southern Altay, Xinjiang, NW China. J. Asian Earth Sci. 28, 439–456.

Pearce, N.J., Perkins, W.T., Westgate, J.A., Gorton, M.P., Jackson, S.E., Neal, C.R., Chenery, S.P., 1997. A compilation of new and published major and trace element data for NIST SRM 610 and NIST SRM 612 glass reference materials. Geostand. Newslett. 21, 115–144.

Peccerillo, A., Taylor, S.R., 1976. Geochemistry of Eocene calc-alkaline volcanic rocks from the Kastamonu area, northern Turkey. Contrib. Mineral. Petrol. 58, 63–81.

Perelló, J., Cox, D., Garamjav, D., Sanjdorj, S., Diakov, S., Schissel, D., Munkhbat, T., Oyun, G., 2001. Oyu Tolgoi, Mongolia: Siluro–Devonian porphyry Cu–Au–(Mo) and high-sulfidation Cu mineralization with a cretaceous chalcocite blanket. Econ. Geol. 96, 1407–1428.

Prouteau, G., Scaillet, B., Pichavant, M., Maury, R.C., 1999. Fluid-present melting of ocean crust in subduction zones. Geology 27, 1111–1114.

Qiu, J.T., Yu, X.Q., Santosh, M., Zhang, D.H., Chen, S.Q., Li, P.J., 2013. Geochronology and magmatic oxygen fugacity of the Tongcun molybdenum deposit, northwest Zhejiang, SE China. Mineral. Deposita 48, 545–556.

Rapp, R.P., Watson, E.B., Miller, C.F., 1991. Partial melting of amphibolite/eclogite and the origin of Archean trondhjemites and tonalites. Precambrian Res. 51, 1–25.

Richards, J.P., 2009. Postsubduction porphyry Cu–Au and epithermal Au deposits: products of remelting of subduction-modified lithosphere. Geology 37, 247–250.

Robb, L., 2009. Introduction to Ore-forming Processes. John Wiley & Sons Inc., New York.

Seltmann, R., Porter, T.M., Pirajno, F., 2014. Geodynamics and metallogeny of the central Eurasian porphyry and related epithermal mineral systems: a review. J. Asian Earth Sci. 79, 810–841.

Sengör, A.M.C., Natal'In, B.A., Burtman, V.S., 1993. Evolution of the Altaid tectonic collage and Palaeozoic crustal growth in Eurasia. Nature 364, 299–307.

Shinohara, H., 1994. Exsolution of immiscible vapor and liquid phases from a crystallizing silicate melt: implications for chlorine and metal transport. Geochim. Cosmochim. Acta 58, 5215–5221.

Sillitoe, R.H., 1972. A plate tectonic model for the origin of porphyry copper deposits. Econ. Geol. 67, 184–197.

Sillitoe, R.H., 2010. Porphyry copper systems. Econ. Geol. 105, 3–41.

Song, G.X., Qin, K.Z., Liu, T.b., Li, G.M., Shen, P., 2010. The U–Pb ages, Hf isotope and REE patterns of older zircon grains from Devonian volcanic rocks in Ashele basin on the southern margin of Altai orogen and its geological significance. Acta Petrol. Sin. 26, 2946–2958 (in Chinese with English abstract).

Sun, S.S., McDonough, W.F., 1989. Chemical and isotopic systematics of oceanic basalts: implications for mantle composition and processes. Geol. Soc. Spec. Publ. 42, 313–345.

Sun, W.D., Arculus, R.J., Kamenetsky, V.S., Binns, R.A., 2004. Release of gold-bearing fluids in convergent margin magmas prompted by magnetite crystallization. Nature 431, 975–978.

Sun, M., Long, X.P., Cai, K.D., Jiang, Y.D., Wang, B.Y., Yuan, C., Zhao, G.C., Xiao, W.J., Wu, F.Y., 2009. Early Paleozoic ridge subduction in the Chinese Altai: insight from the abrupt change in zircon Hf isotopic compositions. Sci. China Ser. D 52, 1345–1358.

Tang, H.F., Qu, W.J., Su, Y.P., Hou, G.S., Du, A.D., Cong, F., 2007. Genetic connection of Sareshike tin deposit with the alkaline A-type granites of Sabei body in Xinjiang: constraint from isotopic ages. Acta Petrol. Sin. 23, 1989–1997 (in Chinese with English abstract).

Tang, G.J., Wang, Q., Wyman, D.A., Li, Z.X., Zhao, Z.H., Jia, X.H., Jiang, Z.Q., 2010. Ridge subduction and crustal growth in the Central Asian Orogenic Belt: evidence from Late Carboniferous adakites and high-Mg diorites in the western Junggar region, northern Xinjiang (west China). Chem. Geol. 277, 281–300.

Tepper, J.H., Nelson, B.K., Bergantz, G.W., Irving, A.J., 1993. Petrology of the Chilliwack batholith, North Cascades, Washington: generation of calc-alkaline granitoids by melting of mafic lower crust with variable water fugacity. Contrib. Mineral. Petrol. 113, 333–351.

Tong, Y., Wang, T., Kovach, V.P., Hong, D.W., Han, B.F., 2006. Age and origin of Takeshiken postorogenic alkali rich intrusive rocks in southern Altai, near the Mongolian border in China and its implication for continental growth. Acta Petrol. Sin. 22, 1265–1278 (in Chinese with English abstract).

Trail, D., Watson, E.B., Tailby, N.D., 2011. The oxidation state of Hadean magmas and implications for early Earth's atmosphere. Nature 480, 79–82.

Trail, D., Bruce Watson, E., Tailby, N.D., 2012. Ce and Eu anomalies in zircon as proxies for the oxidation state of magmas. Geochim. Cosmochim. Acta 97, 70–87.

Tu, X.L., Zhang, H., Deng, W.F., Ling, M.X., Liang, H.Y., Liu, Y., Sun, W.D., 2011. Application of RESOlution in-situ laser ablation ICP-MS in trace element analyses. Geochimica 40, 83–98 (in Chinese with English abstract).

Waight, T.E., Weaver, S.D., Muir, R.J., Maas, R., Eby, G.N., 1998. The Hohonu Batholith of North Westland, New Zealand: granitoid compositions controlled by source H_2O contents and generated during tectonic transition. Contrib. Mineral. Petrol. 130, 225–239.

Wainwright, A.J., Tosdal, R.M., Wooden, J.L., Mazdab, F.K., Friedman, R.M., 2011. U–Pb (zircon) and geochemical constraints on the age, origin, and evolution of Paleozoic arc magmas in the Oyu Tolgoi porphyry Cu–Au district, southern Mongolia. Gondwana Res. 19, 764–787.

Wan, B., Zhang, L.C., 2006. Geochemistry of ore-bearing porphyries in the Kalaxianger copper belt on the southeastern margin of the Altay Mountains, Xinjiang. Chin. Geol. 33, 618–625 (in Chinese with English abstract).

Wan, B., Xiao, W.J., Zhang, L.C., Windley, B.F., Han, C.M., Quinn, C.D., 2011. Contrasting styles of mineralization in the Chinese Altai and East Junggar, NW China: implications for the accretionary history of the southern Altaids. J. Geol. Soc. 168, 1311–1321.

Wan, B., Xiao, W.J., Han, C.M., Windley, B.F., Zhang, L.C., Qu, W.J., Du, A.D., 2014. Re–Os molybdenite age of the Cu–Mo skarn ore deposit at Suoerkuduke in East Junggar, NW China and its geological significance. Ore Geol. Rev. 56, 541–548.

Wang, T., Hong, D.W., Jahn, B.M., Tong, Y., Wang, Y.B., Han, B.F., Wang, X.X., 2006. Timing, petrogenesis, and setting of Paleozoic synorogenic intrusions from the Altai Mountains, northwest China: implications for the Tectonic evolution of an accretionary orogen. J. Geol. 114, 735–751.

Wang, T., Jahn, B.M., Kovach, V.P., Tong, Y., Hong, D.W., Han, B.F., 2009. Nd–Sr isotopic mapping of the Chinese Altai and implications for continental growth in the Central Asian Orogenic Belt. Lithos 110, 359–372.

Wang, T., Tong, Y., Li, S., Zhang, J.J., Shi, X.J., Li, J.Y., Han, B.F., Hong, D.W., 2010. Spatial and temporal variations of granitoids in the Altay orogen and their implications for tectonic setting and crustal growth: perspectives from Chinese Altay. Acta Petrol. Mineral. 29, 595–618 (in Chinese with English abstract).

Watson, M.P., Hayward, A.B., Parkinson, D.N., Zhang, Z.M., 1987. Plate tectonic history, basin development and petroleum source rock deposition onshore China. Mar. Pet. Geol. 4, 205–225.

Watson, E.B., Wark, D.A., Thomas, J.B., 2006. Crystallization thermometers for zircon and rutile. Contrib. Mineral. Petrol. 151, 413–433.

Whitney, D.L., Evans, B.W., 2010. Abbreviations for names of rock-forming minerals. Am. Mineral. 95, 185–187.

Winchester, J.A., Floyd, P.A., 1977. Geochemical discrimination of different magma series and their differentiation products using immobile elements. Chem. Geol. 20, 325–343.

Windley, B.F., Kröner, A., Guo, J.H., Qu, G.S., Li, Y.Y., Zhang, C., 2002. Neoproterozoic to Paleozoic geology of the Altai orogen, NW China: new zircon age data and tectonic evolution. J. Geol. 110, 719–737.

Wu, Q.F., 1987. The Junggar Terrane and Its Significance in the Tectonic Evolution of the Kazakhstan Plate. Plate Tectonics of Northern China. Geological Publishing House, Beijing (in Chinese).

Wu, Y.B., Zheng, Y.F., 2004. Genesis of zircon and its constraints on interpretation of U–Pb age. Chin. Sci. Bull. 49, 1554–1569.

Wu, F.Y., Li, X.H., Zheng, Y.F., Gao, S., 2007. Lu–Hf isotopic systematics and their applications in petrology. Acta Petrol. Sin. 23, 185–220 (in Chinese with English abstract).

Xiang, P., Zhang, L.C., Wu, H.Y., Zhang, X.J., Chen, Z.G., Wan, B., 2009. Ages of the zircon grains from ore-bearing porphyries in II–III ore area of Kalaxianger porphyry copper ore belt in Qinghe, Xinjiang and its significance. Acta Petrol. Sin. 25, 1474–1483 (in Chinese with English abstract).

Xiang, P., Zhang, L.C., Xu, X.W., Liu, G.R., Liu, Z.J., Jin, X.D., Li, W.J., 2012. Geological characteristics and genesis of Yulekenhalasu superimposed and tectonically reworked porphyry copper–gold (molybdenum) deposit in Qinghe, Xinjiang. Acta Petrol. Sin. 28, 2369–2380 (in Chinese with English abstract).

Xiao, X.C., Tang, Y.Q., Feng, Y.M., Zhu, B.Q., Li, J.Y., Zhao, M., 1992. Tectonic Evolution of Northern Xinjiang and Its Adjacent Regions. Geological Publishing House, Beijing (in Chinese).

Xiao, W.J., Windley, B.F., Badarch, G., Sun, S., Li, J.l., Qin, K., Wang, Z., 2004. Palaeozoic accretionary and convergent tectonics of the southern Altaids: implications for the growth of Central Asia. J. Geol. Soc. 161, 339–342.

Xiao, W.J., Windley, B.F., Huang, B.C., Han, C.M., Yuan, C., Chen, H.L., Sun, M., Sun, S., Li, J.L., 2009a. End-Permian to mid-Triassic termination of the accretionary processes of the southern Altaids: implications for the geodynamic evolution, Phanerozoic continental growth, and metallogeny of Central Asia. Int. J. Earth Sci. 98, 1189–1217.

Xiao, W.J., Windley, B.F., Yuan, C., Sun, M., Han, C.M., Lin, S.F., Chen, H.L., Yan, Q.R., Liu, D.Y., Qin, K.Z., 2009b. Paleozoic multiple subduction–accretion processes of the southern Altaids. Am. J. Sci. 309, 221–270.

Xiao, W.J., Santosh, M., 2014. The western Central Asian Orogenic Belt: a window to accretionary orogenesis and continental growth. Gondwana Res. 25, 1429–1444.

Xu, J.F., Castillo, P.R., Chen, F.R., Niu, H.C., Yu, X.Y., Zhen, Z.P., 2003. Geochemistry of late Paleozoic mafic igneous rocks from the Kuerti area, Xinjiang, northwest China: implications for backarc mantle evolution. Chem. Geol. 193, 137–154.

Xu, L.G., Mao, J.W., Yang, F.Q., Daniel, H., Zheng, J.M., 2010. Geology, geochemistry and age constraints on the Mengku skarn iron deposit in Xinjiang Altai, NW China. J. Asian Earth Sci. 39, 423–440.

Xu, X.W., Jiang, N., Li, X.H., Qu, X., Yang, Y.H., Mao, Q., Wu, Q., Zhang, Y., Dong, L.H., 2013. Tectonic evolution of the East Junggar terrane: evidence from the Taheir tectonic window, Xinjiang, China. Gondwana Res. 24, 578–600.

Xue, C.J., Zhao, Z.F., Wu, G.G., Dong, L.H., Feng, J., Zhang, Z.C., Zhou, G., Chi, G.X., Gao, J.G., 2010. The multiperiodic superimposed porphyry copper mineralization in Central Asian tectonic region: a case study of geology, geochemistry and chronology of Halasu copper deposit, southeastern Altai, China. Earth Sci. Front. 17, 53–82 (in Chinese with English abstract).

Yakubchuk, A., 2002. The Baikalide–Altaid, Transbaikal–Mongolian and North Pacific orogenic collages: similarity and diversity of structural patterns and metallogenic zoning. J. Geol. Soc. Lond. 204, 273–297.
Yakubchuk, A., 2004. Architecture and mineral deposit settings of the Altaid orogenic collage: a revised model. J. Asian Earth Sci. 23, 761–779.
Yakubchuk, A.S., Shatov, V.V., Kirwin, D., Edwards, A., Tomurtogoo, O., Badarch, G., Buryak, V.A., 2005. Gold and base metal metallogeny of the central Asian orogenic supercollage. Econ. Geol. 100, 1035–1069.
Yan, S.H., Teng, R.L., Zhang, Z.C., Chen, B., Chen, W., Zhou, G., He, L.X., 2006. New understanding on origin of Kalaxiangeer copper deposit on southern margin of Altay mountain, Xinjiang: constraints from S–Pb–H–O isotope geochemistry and $^{40}Ar/^{39}Ar$ age of Halasu copper deposit. Miner. Depos. 25, 292–301 (in Chinese with English abstract).
Yang, W.P., Zhang, Z.C., Zhou, G., Yan, S.H., He, L.X., Chen, B.L., 2005. Discovery of the Xileketehalasu porphyry copper deposit on the southern margin of the Altay copper metallogenic belt. Chin. Geol. 32, 107–114 (in Chinese with English abstract).
Yang, Y.H., Wu, F.Y., Xie, L.W., Zhang, Y.B., 2009. High-precision measurements of the $^{143}Nd/^{144}Nd$ isotope ratio in certified reference materials without Nd and Sm separation by multiple collector inductively coupled plasma mass spectrometry. Anal. Lett. 43, 142–150.
Yang, F.Q., Mao, J.W., Liu, F., Chai, F.M., Guo, Z., Zhou, G., Geng, X.X., Gao, J., 2010a. Geochronology and geochemistry of the granites from the Mengku iron deposit, Altay Mountains, northwest China: implications for its tectonic setting and metallogenesis. Aust. J. Earth Sci. 57, 803–818.
Yang, F.Q., Yan, S.H., Qu, W.J., Zhou, G., Liu, F., Geng, X.X., Liu, G.R., Wang, X., 2010b. The fluid inclusions and C, H and O isotopic geochemistry of the mineralized zone at the Halasu copper deposit, Xinjiang. Earth Sci. Front. 17, 359–374 (in Chinese with English abstract).
Yang, F.Q., Liu, G.R., Qin, J.H., Zhang, Z.X., Liu, Z.J., Zhang, L.W., Wei, G.Z., Liu, F., Geng, X.X., 2012a. Fluid inclusion and stable isotope study of Yulekenhalasu copper–(molybdenum) deposit in northern margin of Junggar, Xinjiang. Miner. Depos. 31, 965–982 (in Chinese with English abstract).
Yang, F.Q., Mao, J.W., Pirajno, F., Yan, S.H., Liu, G.R., Zhou, G., Zhang, Z.X., Liu, F., Geng, X.X., Guo, C.L., 2012b. A review of the geological characteristics and geodynamic setting of Late Paleozoic porphyry copper deposits in the Junggar region, Xinjiang Uygur Autonomous Region, Northwest China. J. Asian Earth Sci. 49, 80–98.
Yang, F.Q., Zhang, Z.X., Liu, G.R., Qu, W.J., Zhang, L.W., Wei, G.Z., Liu, F., Chai, F.M., 2012c. Geochronology of Yulekenhalasu porphyry copper deposit in northern Junggar area, Xinjiang, China. Acta Petrol. Sin. 28, 2029–2042 (in Chinese with English abstract).
Yang, F.Q., Chai, F.M., Zhang, Z.X., Geng, X.X., Li, Q., 2014. Zircon U–Pb geochronology, geochemistry, and Sr–Nd–Hf isotopes of granitoids in the Yulekenhalasu copper ore district, northern Junggar, China: petrogenesis and tectonic implications. Lithos 190, 85–103.
Yin, J.Y., Chen, W., Yuan, C., Yu, S., Xiao, W.J., Long, X.P., Li, J., Sun, J.B., 2015. Petrogenesis of Early Carboniferous adakitic dikes, Sawur region, northern West Junggar, NW China: implications for geodynamic evolution. Gondwana Res. 27, 1630–1645.
Yuan, C., Sun, M., Xiao, W.J., Li, X.H., Chen, H.L., Lin, S.F., Xia, X.P., Long, X.P., 2007. Accretionary orogenesis of the Chinese Altai: insights from Paleozoic granitoids. Chem. Geol. 242, 22–39.
Zartman, R.E., Doe, B.R., 1981. Plumbotectonics—the model. Tectonophysics 75, 135–162.
Zhang, L.C., Xiao, W.J., Qin, K.Z., Zhang, Q., 2006. The adakite connection of the Tuwu–Yandong copper porphyry belt, eastern Tianshan, NW China: trace element and Sr–Nd–Pb isotope geochemistry. Mineral. Deposita 41, 188–200.
Zhang, Z.C., Mao, J.W., Cai, J.H., Kusky, T.M., Zhou, G., Yan, S.H., Zhao, L., 2008. Geochemistry of picrites and associated lavas of a Devonian island arc in the northern Junggar terrane, Xinjiang (NW China): implications for petrogenesis, arc mantle sources and tectonic setting. Lithos 105, 379–395.
Zhang, Z.C., Mao, J.W., Chai, F.M., Yan, S.H., Chen, B.L., Pirajno, F., 2009a. Geochemistry of the Permian Kalatongke mafic intrusions, northern Xinjiang, northwest China: implications for the genesis of magmatic Ni–Cu sulfide deposits. Econ. Geol. 104, 185–203.
Zhang, Z.C., Zhou, G., Kusky, T.M., Yan, S.H., Chen, B.L., Zhao, L., 2009b. Late Paleozoic volcanic record of the Eastern Junggar terrane, Xinjiang, Northwestern China: major and trace element characteristics, Sr–Nd isotopic systematics and implications for tectonic evolution. Gondwana Res. 16, 201–215.
Zhao, Z.F., Xue, C.J., Zhang, L.W., Wang, L., 2009a. Discovery and significance of Yulekenhalasu porphyry copper deposit on northeast margin of Junggar. Nonferrous Met. 61, 124–128 (in Chinese with English abstract).
Zhao, Z.F., Xue, C.J., Zhang, L.W., Wen, C.S., Zhou, G., Liu, G.R., 2009b. U–Pb dating of zircon grains from acid intrusions in Yulekenhalasu copper deposit of Qinghe, Xinjiang, and its geological significance. Miner. Depos. 28, 425–433 (in Chinese with English abstract).
Zheng, J.P., Sun, M., Zhao, G.C., Robinson, P.T., Wang, F.Z., 2007. Elemental and Sr–Nd–Pb isotopic geochemistry of Late Paleozoic volcanic rocks beneath the Junggar basin, NW China: implications for the formation and evolution of the basin basement. J. Asian Earth Sci. 29, 778–794.
Zhou, T.F., Yuan, F., Fan, Y., Zhang, D.Y., Cooke, D., Zhao, G.C., 2008. Granites in the Sawur region of the west Junggar, Xinjiang Province, China: geochronological and geochemical characteristics and their geodynamic significance. Lithos 106, 191–206.
Zimmer, M., Kroner, A., Jochum, K.P., Reischmann, T., Todt, W., 1995. The Gabal Gerf complex: a Precambrian N-MORB ophiolite in the Nubian Shield, NE Africa. Chem. Geol. 123, 29–51.